Synthese, Charakterisierung und Untersuchungen zum Reduktionsverhalten von nanostrukturierten Metalloxiden in mesoporösen Kohlenstoffen

Dissertation

zur Erlangung des Doktorgrades des Fachbereichs Chemie
der Justus-Liebig-Universität Gießen

vorgelegt von

Holger Huwe

aus Hamburg

Gießen, 2007

Die vorliegende Arbeit entstand in der Zeit von August 2001 bis Januar 2007 am Institut für Anorganische und Analytische Chemie der Justus-Liebig-Universität Gießen in der Arbeitsgruppe von Prof. Dr. Michael Fröba.

1. Gutachter: Prof. Dr. Michael Fröba

2. Gutachter: Prof. Dr. Siegfried Schindler

Der denkende Mensch ändert seine Meinung.

(Friedrich Nietzsche)

1 Einleitung

Das Ziel dieser Arbeit war die Synthese, Charakterisierung und Modifizierung neuartiger mesoporöser, nanostrukturierter Wirt/Gast-Verbindungen sowie eine umfassende Untersuchung zum Reduktionsverhalten der Gastspezies mit Schwerpunkt auf dem System Fe-O. Parallel dazu wurden erste katalytische Untersuchungen zur Methanolzersetzung an ausgewählten Eisenoxiden durchgeführt. Letztere erfolgten in Kooperation mit dem Institut für Katalyse und dem Institut für Organische Chemie der Bulgarischen Akademie der Wissenschaften in Sofia unter der Leitung von Prof. Dr. Christo Minchev.

Als Gastsystem wurde die Gruppe der geordneten mesoporösen Kohlenstoffe gewählt. Mit deren Einführung durch den Südkoreaner Ryoo im Jahr 1999 erhielten die Wissenschaftler Zugang zu einem Material, das den bis dahin benutzten geordneten mesoporösen Silicamaterialien in einigen Bereichen (z.B. thermische und mechanische Stabilität) überlegen ist.[1] Ryoo widmete diese mesoporösen Kohlenstoffe seinem Institut und nannte sie dementsprechend *Carbons Mesoporous by KAIST*, kurz CMK-n. Eine weitere Gruppe geordneter mesoporöser Kohlenstoffe bildet die der Seouler National Universität, kurz SNU-n. Das n dient als Index für die Klassifizierung der Materialien. Eine detaillierte Übersicht über den Stand der Forschung auf dem Gebiet der porösen Kohlenstoffmaterialien bietet ein 2006 erschienener Übersichtsartikel.[2]

Die mesoporösen Kohlenstoffe aus der Gruppe der CMK-n zeigen eine hohe thermische Stabilität bis zu 1900 K in Inertgasatmosphären, hohe Stabilität gegenüber starken Säuren und Basen, hohe mechanische Stabilität sowie eine außergewöhnliche elektrische Leitfähigkeit.[3-8] Daher sind diese mesoporösen Kohlenstoffe nicht nur für Adsorptionsuntersuchungen, zur Wasserstoffspeicherung, für elektronische Anwendungen und als katalytisches Trägermaterial, sondern auch als Wirtmaterial in der Wirt/Gast-Chemie von Interesse.[8-12]

Hergestellt werden die mesoporösen Kohlenstoffe, indem die Porenkanäle eines entsprechenden mesoporösen Ausgangsmaterials (i.d.R.: Silica) zuerst mit einer Kohlenstoffquelle, zum Beispiel einer Zuckerlösung, gefüllt werden. Im nächsten Schritt wird der Zucker polymerisiert und anschließend pyrolisiert. Der so erhaltende Kohlenstoff wird dann im letzten Schritt mit einer starken Säure oder Lauge vom Silicagerüst befreit, siehe Abbildung 1. Durch die entsprechende Auswahl des Ausgangsmaterials und der

Kohlenstoffquelle können mesoporöse Kohlenstoffe mit unterschiedlich geordneten Porensystemen erhalten werden (z.B. MCM-48 Silica → CMK-1, SBA-1 → CMK-2, AlMCM-48 → SNU-1, HMS → SNU-2).[2,6,7]

Abbildung 1: Schematischer Syntheseweg von mesoporösen Kohlenstoffen CMK-n am Beispiel des CMK-1.

Eingesetzt wurden hier die beiden prominentesten Vertreter CMK-1 und CMK-3. Beide besitzen eine hydrophobe, graphitähnliche Oberfläche mit polyaromatischem Charakter ähnlich wie die der *carbon blacks* oder der *carbon fibres.*[4]

Die Synthese der mesoporösen Kohlenstoffe der Gruppe CMK-n erfolgt nach dem sogenannten Exotemplatverfahren. Dazu wird ein porenhaltiges Gerüstmaterial als Templat, genauer Strukturdirektor, eingesetzt. Innerhalb dessen wird ein Feststoff zuerst synthetisiert und anschließend vom Strukturdirektor befreit (Abb. 1).[13]

Für die Synthese des CMK-1 dient der MCM-48 Silica als Strukturdirektor. In das ineinander verwundene, dreidimensionale Netzwerk des mesoporösen, enantiomorphen Porenpaars des MCM-48 Silica (Raumgruppe kubisch $Ia\bar{3}d$) wird die Zuckerlösung gefüllt. Während des Karbonisierens bilden sich röhrenähnliche Kohlenstoffstrukturen an den Porenwänden des MCM-48 Silica aus. Bedingt durch die zwei verschiedenen Kanalsysteme des Strukturdirektors bleiben diese Kohlenstoffstrukturen solange voneinander getrennt und die Raumgruppe erhalten, bis das Silicagerüst herausgelöst wird. Nach dem Herauslösen des Silicagerüsts sieht es so aus, als ob die beiden Kohlenstoffröhren sich verbinden, begleitet durch einen Wechsel der Raumgruppe hin zu $I4_132$ oder niedriger. Eine schematische Darstellung ist in Abbildung 2 zu sehen. Bis heute konnte nicht vollständig geklärt werden, ob die beiden Kohlenstoffröhren dauerhaft miteinander verknüpft sind oder sich wie beim MCM-48 Silica nur gegenseitig durchdringen.[2,7] Charakteristische Daten sind in Tabelle 1 aufgeführt.

Tabelle 1: Charakteristische Daten des CMK-1 und CMK-3.[2,7] *Die angegebenen Werte sind abhängig von den Synthesebedingungen und daher als Größenordnung zu verstehen.*

Parameter	**CMK-1**	**CMK-3**
Struktur	kubisch	hexagonal
Raumgruppe	$I4_l32$	p6mm
a_0 [nm]	8 – 9,5	8 - 11
innere Oberfläche [m^2/g]	1400 - 2200	450 - 1600
D_p (BJH) [nm]	2 - 4	3 - 9
V_p [cm^3/g]	0,9 – 1,2	1,3
Mikro/Mesoporen	1:4	1:7

a_0: Einheitszellparameter; D_p: Mesoporendurchmesser; V_p: Gesamtporenvolumen.

Zur Synthese des CMK-3 wird der SBA-15 Silica als Strukturdirektor eingesetzt. Anders als beim CMK-1 ist der CMK-3 das negative Abbild des SBA-15 Silica bei gleicher Symmetrie des Porensystems. Die Struktur des mesoporösen Kohlenstoffs bildet sich durch eine hexagonale Anordnung von eindimensionalen Kohlenstoffstäben. Diese Stäbe sind ihrerseits über weitere, wesentlich dünnere Kohlenstoffstäbe miteinander verbunden. Somit wird ein CMK erhalten, der eine geordnete, zweidimensionale, hexagonale Anordnung der Mesoporen aufweist (Abb. 2). Neben den Mesoporen besitzt der CMK-3 noch Mikro- und sekundäre, nicht geordnete Mesoporen. [2,7] Charakteristische Daten sind in Tabelle 1 aufgeführt.

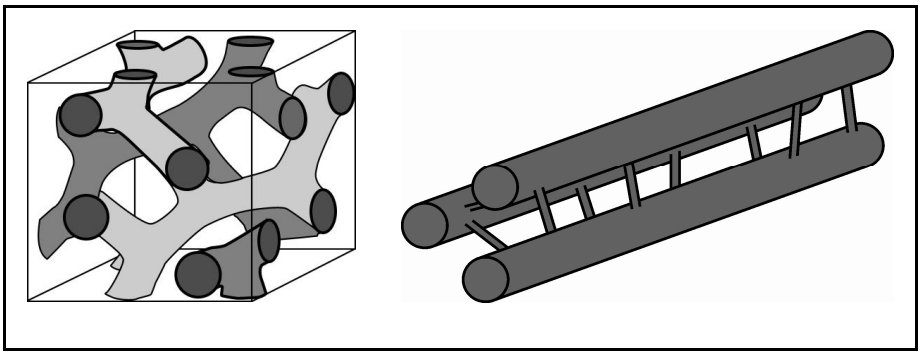

Abbildung 2: Schematische Darstellung vom CMK-1 (links) und CMK-3 (rechts).

Nanostrukturierte Metalloxide und Metalle ausgewählter 3d-Metalle (Mangan, Eisen, Kobalt, Nickel, Kupfer und Zink) wurden innerhalb der Mesoporen von mesoporösen Kohlenstoffen des Typs CMK-n synthetisiert. Das Reduktionsverhalten der 3d-Metalloxide wird schon mehr als ein Jahrhundert untersucht. Dabei dient das Eisenoxidsystem Hämatit → Magnetit → Wüstit → Eisen oft als Modellsystem für die Vielzahl der Übergangsmetalloxide; zahlreiche

Experimente und extensive theoretische Untersuchungen wurden an ihm schon durchgeführt. Dieses System findet unter anderem Anwendung im Hochofenprozess, in der Katalyse und neuerdings bei der Wasserstoffspeicherung.[14-34]

Erste Untersuchungen zur Struktur und zum Reduktionsverhalten gehen auf Pauling und Hendricks in den frühen Zwanzigern des letzten Jahrhunderts zurück.[35] Seit dem gibt es zahlreiche Arbeiten mit dem Ziel, die Eigenschaften des Eisenoxidsystems besser zu verstehen und somit einen Einblick in dessen Reduktionsverhalten zu bekommen.[18,32-38]
Während des Reduktionsprozesses erfahren die Oktaeder des Hämatits eine Strukturumwandlung von der Hämatitstruktur über eine inverse Spinellstruktur (Magnetit), eine defekte Natriumchloridstruktur (Wüstit) zu einer kubisch raumzentrierten Struktur (bcc) des Eisens. Der sehr komplexe Reduktionsverlauf ist abhängig von den Reduktionsparametern wie zum Beispiel der Heizrate, dem Reduktionsgas und der Partikelgröße. Es ist daher nicht verwunderlich, dass es verschiedene Ansichten über dessen Ablauf gibt.[39] Erste umfassende Studien zum Reduktionsverhalten von volumenkristallinem Hämatit wurden 1984 von St. John[40] sowie 1987 von Rau[41] vorgestellt. Experimente mit kleineren Eisenoxidpartikeln in der Größenordnung 50 – 800 µm wurden dann 1981 von Hayes[42] und 1988 von El-Tabirou[43] veröffentlicht.

Erst mit der Einführung der Wirt/Gast-Chemie konnten in den späten 90ern des letzten Jahrhunderts erste Untersuchungen nicht nur an nanostrukturierten Eisenoxiden durchgeführt werden. Unterschiedliche Nanopartikel (z.B. Pt, CdS, MnS, NiO), aufgebaut in den Poren der mesoporösen Silicamaterialien (z.B. MCM-41, MCM-48, SBA-15), zeigten deutlich andere Eigenschaften als die entsprechenden Volumenkristalle. Zurückzuführen ist dieser Effekt unter anderem auf die Größenlimitierung der Gaststrukturen bedingt durch die Porengröße des Wirtmaterials.[23-25,27-29,44-45]

Erste Untersuchungen zum Reduktionsverhalten der nanostrukturierten Eisenoxide im Wirt/Gast-System Fe_2O_3@MCM-48 Silica wurden in unserer Arbeitsgruppe von Köhn et al. 2001 durchgeführt. Neben einer Reduktion von Fe(III) zu Fe(II) wurde dabei auch durch die Reaktion mit dem Wirtmaterial die Bildung von Fe_2SiO_4 beobachtet.[24,46] Bedingt durch die sauerstoff- und silicatfreie Umgebung beim Einsatz von mesoporösen Kohlenstoffen als Wirtsysteme ist es nun möglich, das Reduktionsverhalten von nanostrukturiertem Eisenoxid genauer zu untersuchen.

Generell sind zwei Wege denkbar, um die Phasenentwicklung während des Reduktionsprozesses vom Hämatit bis hin zum Eisen zu untersuchen. Zum einen kann die Reduktion bei einer bestimmten Temperatur abgebrochen und dann die Probe charakterisiert werden. Die Charakterisierung der Proben erfolgt im Anschluss daran mittels der sehr leistungsstarken Röntgenabsorptionsspektroskopie (XAS). Sowohl die Gewinnung von Reduktionsreihen als auch die Charakterisierung mittels XAS sind sehr zeit- und materialaufwendig, liefern aber, wie später gezeigt wird, sehr gute Ergebnisse.
Eine andere Möglichkeit ist die Verfolgung der Reduktionen *in situ* mittels Synchrotronstrahlung (*in situ* XAS). Es ist eine schnelle, elegante Methode, die auch schon vielfach für katalytische Untersuchungen eingesetzt wird. Die Nachteile sind, dass es zu Beginn dieser Arbeit im Jahre 2001 keine geeignete Reaktionszelle gab und sowohl die Aufnahme als auch die Auswertung von Röntgenabsorptionsspektren sehr komplex ist.

Eines der Hauptprobleme liegt in einer vernünftigen Charakterisierung der Wirt/Gast-Verbindungen, besonders in der der nanostrukturierten Gäste. Zum Nachweis, dass sich die Gäste überwiegend in den Poren des Wirtmaterials und nicht auf deren äußeren Oberflächen befinden sowie die Erhaltung der Wirtstruktur bei den Umsetzungen gegeben ist, ist die Nutzung einer Vielzahl von sich ergänzenden leistungsstarken Charakterisierungstechniken erforderlich. Diese sind zum Beispiel die Röntgenpulverdiffraktometrie (P-XRD), die Transmissionselektronenmikroskopie (TEM), die Ramanspektroskopie und die Stickstoff-Physisorption. Zur Charakterisierung der Gastverbindungen und Reduktionsprodukte werden Techniken wie die P-XRD, die TEM, die Infrarotspektroskopie und die Röntgenabsorptions-spektroskopie mittels Synchrotronstrahlung (XAS) eingesetzt.

Die Wirt/Gast-Verbindungen können im Prinzip auf zwei unterschiedlichen Wegen hergestellt werden.[47] Einer ist die direkte Zugabe des Wirtes während der Synthese der Gastspezies, ein anderer ist die Imprägnierung nach dessen Synthese. Letzterer bietet den Vorteil, dass mit einem qualitativ hochwertigem Wirtmaterial gearbeitet werden kann. Diese Art der Einlagerung kann entweder aus der Gasphase oder über eines der nasschemischen Imprägnierungsverfahren erfolgen. Die nasschemischen Imprägnierungsverfahren erfordern aber eine sehr sorgfältige Handhabung, da sonst das Gastsystem beschädigt oder die Gäste auch auf der Oberfläche der Wirtstruktur und nicht ausschließlich in den Porenkanälen zu finden sind. Der Vorteil gegenüber Einlagerungen aus der Gasphase ist die Möglichkeit, eine höhere Belegung der Poren zu erreichen.

Hier wurden die Wirte mit einer entsprechenden Metallnitratlösung behandelt, von der Lösung getrennt, getrocknet und abschließend die Nitrate in die Oxide überführt. Die so erhaltenen Wirt/Gast-Verbindungen werden im Folgenden als Me_xO_y@CMK-n bezeichnet, also z.B. Co_3O_4@CMK-3 für Cobaltoxid als Gastverbindung im Porensystem vom CMK-3. Durch diese Synthese innerhalb der Mesoporen werden nanostrukturierte Gastverbindungen erhalten, die in ihrer Ausdehnung in zwei Dimensionen durch den Porendurchmesser begrenzt sind und in der Dritten durch die Länge der Poren.

Die vorliegende Arbeit kann im Prinzip in mehrere parallel bearbeitete Bereiche aufgeteilt werden. Ein Bereich ist der Synthese- und Charakterisierungsteil der nanostrukturierten Wirt/Gast-Verbindungen. In der ersten Veröffentlichung von 2003[V2.1] wurde die sogenannte „intra-pore“ Synthese und Charakterisierung von nanostrukturiertem Eisen(III)oxid im Porensystem vom CMK-1 vorgestellt. Darauf aufbauend wurde 2006[V2.7] gezeigt, dass dieses auch mit anderen 3d-Metallen möglich ist. Zusätzlich wurde darin gezeigt, dass eine innerhalb der Porensysteme durchgeführte Reduktion der Metalloxide zu den reinen Metallen ohne eine nachweisbare Schädigung der Wirtstruktur möglich ist. Parallel zu diesen Synthesen wurden die ersten eisenoxidhaltigen Wirt/Gast-Verbindungen katalytischen Tests unterzogen. Die Ergebnisse in Bezug auf die Methanolzersetzung wurden 2004[V2.3] und 2005[V2.4] veröffentlicht.

Das Reduktionsverhalten des Systems Hämatit – Magnetit – Wüstit – Eisen wurde näher untersucht. Ziel war es, eine Einsicht in das Reduktionsverhalten dieses nanostrukturierten Systems zu erhalten sowie die jeweiligen Eisenoxide möglichst phasenrein in den Poren der Wirte herzustellen. Die Ergebnisse dieser Untersuchungen werden demnächst veröffentlicht.[V2.8]

Bedingt durch die Nanostrukturierung der Gastsysteme lieferte deren Charakterisierung mittels Röntgenabsorptionsspektroskopie als Hauptuntersuchungsmethode mit dem bisher angewandten Auswertungsverfahren keine zufriedenstellenden Ergebnisse mehr. Das Auswertungsverfahren wurde daher verfeinert und auf die nanostrukturierten Eisenoxide angewendet.[V2.6]

Daneben hat sich die Reduktion der Gastsysteme im Labor mittels temperaturgesteuerter Reduktion mit anschließender Charakterisierung, obwohl sie sehr gute Ergebnisse liefert[V2.8], als sehr zeit- und materialaufwendig herausgestellt.

Eine elegante, schnelle Methode ist die Verfolgung der Reduktion *in situ* mittels der Röntgenabsorptionsspektroskopie. Bis zu diesem Zeitpunkt gab es noch keine geeignete Reaktionszelle, um Reduktionen mit geringen Mengen an Reduktionsmaterial in einer Wasserstoff/Stickstoff-Atmosphäre kontrolliert und temperaturabhängig bis 1300 K durchzuführen. Außerdem sollte mit Hilfe dieser Zelle ein Onlinemonitoring sowohl der Transmissions- als auch der Fluoreszenzstrahlung möglich sein. Daher wurde eine entsprechende Zelle entwickelt und erfolgreich getestet[V2.2]. Erste Anwendungen mit dieser Zelle zum Reduktionsverhalten von Fe_2O_3@CMK-1 wurden im Frühjahr 2006 publiziert[V2.5].

2 Veröffentlichungen

Die Veröffentlichungen sind in der Reihenfolge ihres Erscheinens aufgeführt.

Die Veröffentlichungen V2.3 und V2.4 sind aus Kooperationen mit anderen Instituten entstanden. Mein Anteil an diesen Arbeiten ist die Synthese und Charakterisierung der untersuchten Wirt/Gast-Verbindungen mittels P-XRD, N_2-Physisorption, TEM und XAS.

Available online at www.sciencedirect.com
SCIENCE DIRECT®
ELSEVIER
Microporous and Mesoporous Materials 60 (2003) 151–158
MICROPOROUS AND MESOPOROUS MATERIALS
www.elsevier.com/locate/micromeso

Iron (III) oxide nanoparticles within the pore system of mesoporous carbon CMK-1: intra-pore synthesis and characterization

Holger Huwe, Michael Fröba *

Institute of Inorganic and Analytical Chemistry, Justus-Liebig-University Giessen, Heinrich-Buff-Ring 58, D-35392 Giessen, Germany

Received 20 December 2002; received in revised form 17 March 2003; accepted 20 March 2003

Abstract

Iron (III) oxide nanoparticles were synthesized inside the pore system of mesoporous carbon CMK-1. This intra-pore synthesis was carried out using several cycles of wet impregnation, drying and calcination procedures. The existence of iron (III) oxide nanoparticles within the pore system was proved by powder X-ray diffraction, nitrogen physisorption, preservation of the host structure by Raman spectroscopy and transmission electron microscopy. Finally, the local structure of the iron oxide was determined by X-ray absorption spectroscopy.

Keywords: CMK-1; Mesoporous carbon; Iron (III) oxide; Nanoparticles; X-ray absorption spectroscopy

1. Introduction

Ordered mesoporous carbons are known since 1999 [1]. This new group of materials designated as CMK-*n* ($n = 1$–5) possess several advantages compared to mesoporous silica molecular sieves, i.e. high thermal stability up to 1600 °C in N_2 atmosphere, high stability in strong acids and bases, high mechanical stability and especially electric conductivity [2,3]. Therefore, the mesoporous carbons are of great interest for, e.g. adsorption [3,4], catalyst supports [5], electronic applications [6–9] and host–guest chemistry [10].

The carbon synthesis procedure starts with an infiltration of a carbon source (e.g. sucrose or furfuryl alcohol) into a mesoporous silica phase, followed by a carbonization step and, finally, the removal of the silica framework using HF or ethanolic NaOH solution. The usage of different mesoporous silica sources leads to different mesoporous carbon materials (e.g. MCM-48 → CMK-1; SBA-1 → CMK-2; SBA-15 → CMK-3). The obtained mesoporous carbons exhibit varieties of structures, specific surface areas, pore diameters and pore volumes, e.g. CMK-1 (space group cubic $I4_1$ 32 or lower) synthesized from MCM-48 silica can exhibit high specific surface areas up to 2200 m^2/g. During the removal of the silica phase the structure transforms from two interpenetrating networks to an interwoven structure. The outer surface of CMK-*n* has a graphite-like, polyaromatic

* Corresponding author. Tel.: +49-641-99-34100; fax: +49-641-99-34109.
E-mail address: michael.froeba@anorg.chemie.uni-giessen.de (M. Fröba).

1387-1811/03/$ - see front matter
doi:10.1016/S1387-1811(03)00336-6

character similar to carbon blacks or carbon fibres [4].

During the last three years we were able to synthesize different transition metal oxides within mesoporous silica phases [11–13]. Here we report on the first synthesis of iron (III) oxide nanoparticles within the mesoporous carbon material CMK-1. Adapted impregnation and calcination cycles allow the control over the degree of coating and loading of the host structure. The application of multiple characterization techniques, i.e. powder X-ray diffraction (PXRD), N_2 physisorption, Raman and IR spectroscopy, X-ray absorption spectroscopy and transmission electron microscopy, proves that nanostructured iron (III) oxide has been formed within the pore system of CMK-1.

2. Experimental

2.1. Syntheses

The syntheses of the mesoporous MCM-48 silica [11] and the host structure CMK-1 carbon were carried out in accordance with the procedures described in the literature [1,5,14,15]. Up to four impregnation, drying and calcination cycles were applied to form iron (III) oxide within the host structure.

In a typical procedure 1 g dried CMK-1 was stirred for 30 min in 50 cm^3 of an ethanolic or aqueous solution of iron nitrate (4.6 mol/l) at room temperature. The carbon–iron nitrate composite was separated from the solution by centrifugation (2970 rotations/min, 30 min) and dried under vacuum at room temperature. Afterwards, the sample was calcined at 623 K for 10 h, leading to the transformation of the iron nitrate into iron (III) oxide. The completion of the transformation was indicated by the disappearance of the IR band of the nitrate ion at 1380 cm^{-1}. Depending on the number of impregnation, drying and calcination cycles a desired iron content between 15 and 65 wt.% could be obtained.

2.2. Characterization

The samples were analyzed by PXRD with filtered CuK_α radiation using a Bruker AXS D8 Advance diffractometer in Θ/Θ geometry (continuous scan mode: speed: 0.02° (2Θ)/min and counting time of 6 s/data point).

Infrared spectra were recorded on a Perkin-Elmer Spectrum GX FTIR spectrometer in the range between 400 and 4000 cm^{-1} using the KBr pellet method.

Nitrogen physisorption measurements were recorded with an Autosorb 6 instrument (Quantachrome) at 77 K. Before the physisorption measurements the samples were outgassed at 423 K for 16–29 h. The surface areas were calculated from the adsorption branch in a region of $p/p_0 = 0.03$ to 0.20 applying the Brunauer, Emmet and Teller (BET) [16] method. The pore size distributions were calculated using the desorption branch and applying the Barrett–Joyner–Halenda (BJH) method [17]. The total pore volume was extracted from the adsorption branch using a respective data point at $p/p_0 = 0.97$–0.99.

Raman spectroscopy was carried out with a Raman microscope system (Jobin-Yvon). The argon-ion laser operated at 514.5 nm. The resolution of the spectra was 1 cm^{-1}.

Transmission electron microscopy was carried out using a Philips CM30 instrument operating at 300 kV in the bright field mode. For that the samples were crushed in acetone and dispersed on a holy carbon grid.

X-ray absorption spectroscopic measurements were carried out at the storage ring DORIS III (HASYLAB@DESY, Hamburg, Germany) at the EXAFS beam line A1 which was equipped with an Si(1 1 1) double-crystal monochromator. The Fe K-edge spectra were taken at liquid-nitrogen temperature (77 K). All the spectra were recorded in the fluorescence mode up to four times to improve after summation the signal to noise ratio. The samples were measured as fresh pressed polyethylene pellets. For further data analysis the programs WinXAS 2.0 [18] and FEFF 7.0 [19] were used.

3. Results

3.1. Powder X-ray diffraction

Fig. 1 shows the powder X-ray diffraction patterns of the mesoporous carbon host and the

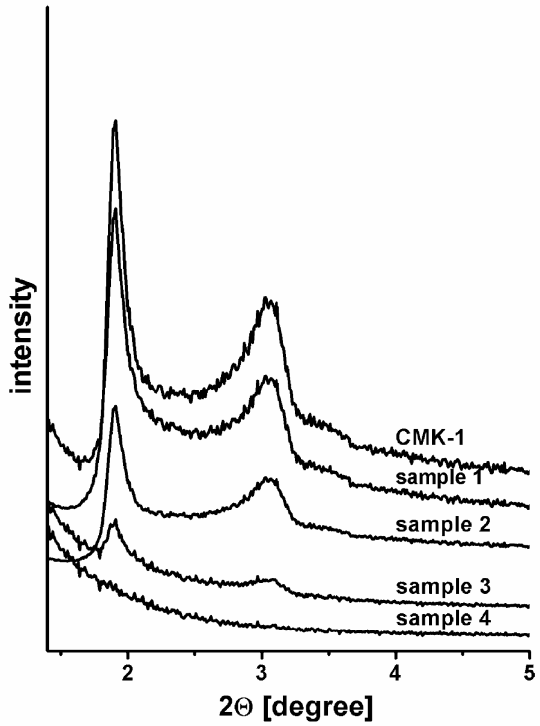

Fig. 1. PXRD of CMK-1 and the host/guest compound after the first (sample 1), the second (sample 2), the third (sample 3) and the fourth (sample 4) impregnation/calcination cycle.

corresponding host/guest compounds after the first, second, third and fourth (sample 4) impregnation/calcination cycle. With every impregnation/calcination cycle the X-ray peak intensities decrease and slowly shift to smaller d spacings (see Table 1). These effects have already been discussed in previous studies dealing with metal oxide phases within mesoporous silica [11–13]. The loss in intensity is due to the fact that the introduction of scattering material into the pores leads to an increased phase cancellation between scattering from the walls and the pore regions. In case of sample 4 the absence of the XRD reflections can be attributed to a very high filling of the pores.

Fig. 2 exhibits the diffraction pattern of sample 4. The inset shows the range in which the strongest reflections of bulk haematite appear. The absence of these prominent reflections in case of the nanostructured iron (III) oxide indicates that no

Table 1
d-Spacings of the CMK-1 and the host/guest compounds after the first, second and third impregnation/calcination cycle

	d_{110} [nm]	d_{211} [nm]
CMK-1	4.70	2.91
Sample 1	4.65	2.89
Sample 2	4.63	2.87
Sample 3	4.55	–

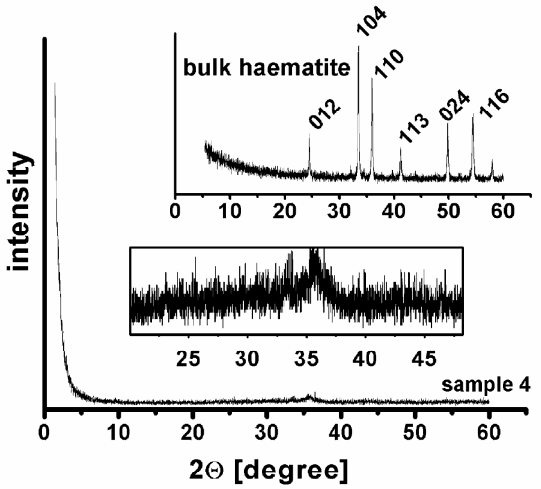

Fig. 2. Diffraction pattern of sample 4 in comparison with bulk haematite. The inset shows a magnification of sample 4 in the range where the strongest reflections of haematite appear.

crystalline bulk material has been formed outside the pore system. The weak and broad reflection at $2\Theta \approx 35°$ corresponds to almost X-ray amorphous very small iron (III) oxide crystallites.

3.2. Nitrogen sorption

Besides PXRD nitrogen physisorption is the method of choice to gain knowledge about mesoporous materials. This method gives information on the specific surface area and the pore diameter. Calculating pore diameters of mesoporous materials using the BJH method is common [20]. Although the applied theory is not perfect for small mesopores (<4 nm) and not usable for micropores, it can give information concerning differences between the host/guest compounds and the pristine mesoporous carbon. Former studies show that the application of

the BJH theory gives appropriate qualitative results which allow a direct comparison of relative changes between different mesoporous materials [21–24].

The isotherms of the nitrogen physisorption measurements of the CMK-1 and host/guest compounds received after the first to fourth impregnation step (samples 1–4) as well as the pore diameter distributions of CMK-1, sample 2 and sample 4 are shown in Figs. 3a and b. The data for the BET surface areas and the pore diameters are listed in Table 2. The isotherms of the samples 1, 2 and 3 still exhibit mesoporosity (t-plots do not reveal any microporosity), which indicates a coating of the inner surface of CMK-1. These materials show type IV isotherms (IUPAC classification) typical for mesoporous systems [25]. A well-defined step occurs at about $p/p_0 = 0.4$ for samples 1–3. This is associated with the filling of the mesopores due to capillary condensation. Depending on the number of impregnation/calcination cycles the amount of adsorbed nitrogen decreases. Sample 4 shows only a weak step, indicating a very high degree of pore loading. This material exhibits microporosity due to the pore filling as well as a small amount of larger mesopores which might be caused by interparticle porosity. With the intra-pore formation of the iron oxide the step of capillary condensation is slightly broadened, representing a less uniform remaining pore size probably caused by inhomogeneous pore filling.

The pore diameters of the pristine host compound, sample 2 and sample 4 are shown in Fig. 3b, the corresponding data are listed in Table 2. It can clearly be seen, that the pore diameter decreases with the number of impregnation steps accompanied with a broadening of the diameter distribution. This is probably due to a slight inhomogeneous filling of the mesopores. For sample 4 no pore diameter can be determined in the range of mesopores. In addition, it has to be kept in mind that the loading of CMK-1 itself leads also to a reduction of the specific surface areas.

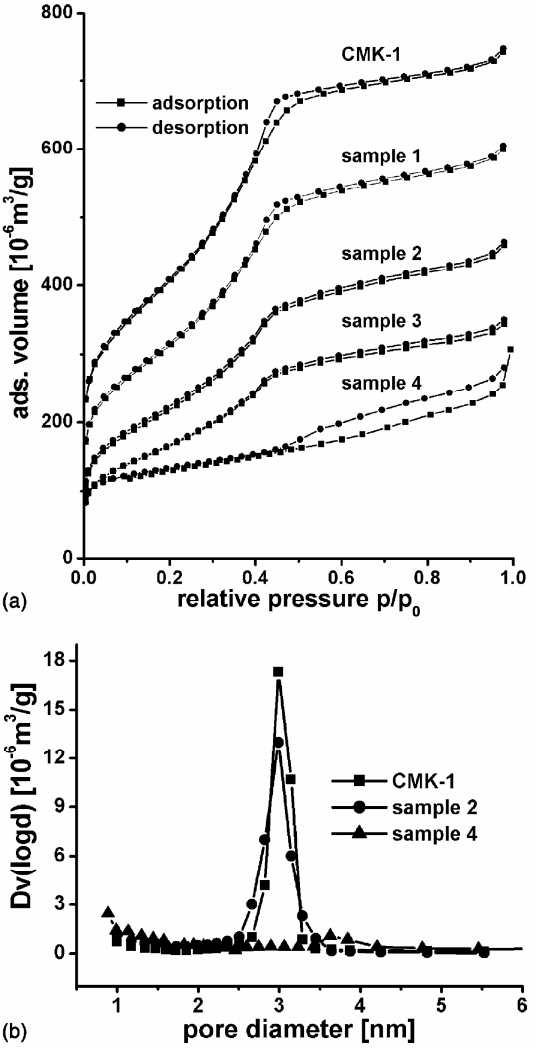

Fig. 3. (a) Nitrogen adsorption/desorption isotherms (77 K) of CMK-1 and the host/guest compounds after the respective impregnation/calcination cycles. (b) BJH pore size distributions ($Dv(\log d) \equiv \mathrm{d}V/\mathrm{d}(\log D)$) for CMK-1, sample 2 and sample 4 calculated from the desorption branch.

3.3. Raman spectroscopy and transmission electron microscopy

In order to verify that the host structure remains intact even after the fourth impregnation/calcination cycle, Raman spectroscopic measurements were carried out. The corresponding spectra are depicted in Fig. 4. For CMK-1 the two bands appear at 1333 cm^{-1} and 1592 cm^{-1} while they are slightly shifted to lower wavenumbers in sample 4 (1316 and 1575 cm^{-1}), an effect which can be at-

Table 2
N_2 physisorption data of CMK-1 and the four host/guest compounds[a]

Sample	S_{BET} [m^2/g]	D_p (BJH) [nm]	V_p [10^{-6} m^3/g]
CMK-1	1403	3.11	0.74 ($p/p_0 = 0.97$)
Sample 1	1210	3.10	0.60 ($p/p_0 = 0.98$)
Sample 2	1005	3.06	0.46 ($p/p_0 = 0.98$)
Sample 3	634	3.02	0.35 ($p/p_0 = 0.98$)
Sample 4	220	<1	0.30 ($p/p_0 = 0.99$)

[a] S_{BET}: total surface area by BET theory; D_p (BJH): BJH pore diameter; V_p: total pore volume at a relative pressure $p/p_0 = 0.97$–0.99.

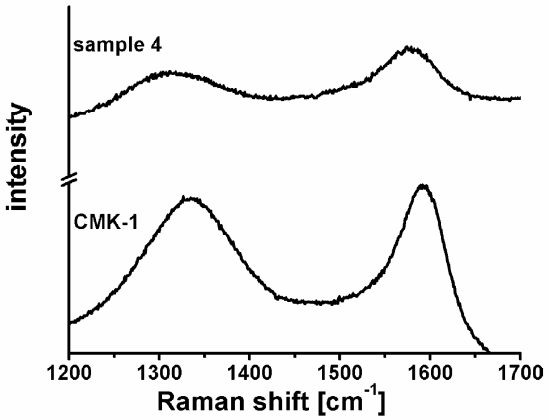

Fig. 4. Raman spectra of CMK-1 and the host/guest compound after the fourth impregnation/calcination cycle (sample 4).

tributed to an increased degree of disorder within the material due to multiple thermal impregnation/calcination cycles. The graphite-like, polyaromatic character of CMK-1 [3] seems to be preserved during the impregnation/calcination cycles. Nevertheless, in the literature these Raman bands (1350, 1582 and 1620 cm^{-1} not resolved) are described as "disordered sp^2 bonded graphite" [26]. The band at 1350 cm^{-1} is a so-called disorder-induced band (D-band) and appears only for disordered graphite. The symmetry-allowed G-band (E_{2g2} mode) appears at 1582 cm^{-1}.

The transmission electron micrograph (Fig. 5) shows the host/guest compound after the fourth impregnation/calcination cycle. Again, it can clearly be seen that the mesoporous carbon host

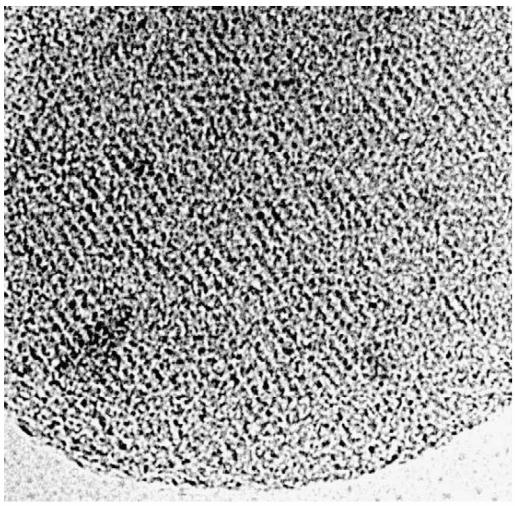

Fig. 5. Transmission electron micrograph of the host/guest compound after the fourth impregnation/calcination cycle (sample 4).

structure is preserved. In addition, no iron oxide particles could be detected on the surface which is a further confirmation that iron oxide is exclusively formed within the pore system.

3.4. X-ray absorption spectroscopy

In order to gain structural information on the local structure of the iron within the pores X-ray absorption spectroscopic measurements were carried out at the Fe K-edge. The Fourier transforms (FT) of the Fe K-edge oscillations $\chi(k)k^3$ of sample 4 as well as of bulk haematite synthesized under the same experimental conditions as for the host/guest compounds are shown in Fig. 6. The data analysis, using the program WinXAS, was focused on the Fe–Fe shells. The shells were extracted by a Fourier filter using a Bessel window in the range between 1.8 and 12.5 Å. The number of parameters in the fits were all significantly smaller than the possible number of independent parameters. A detailed description of the data analysis will be given in a future paper.

The modified radial distribution function of bulk haematite exhibits coordination shells up to 7.5 Å, while in case of the host/guest compounds

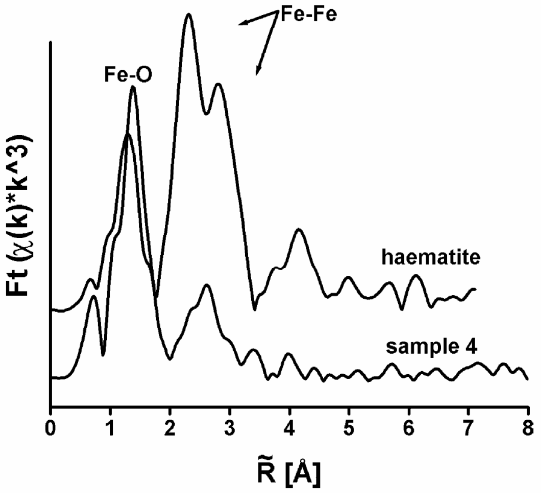

Fig. 6. Modified radial distribution function (mRDF) of the Fe K-edge oscillations $\chi(k)k^3$ of the host/guest compound after the fourth impregnation/calcination cycle (sample 4) as well as of bulk haematite.

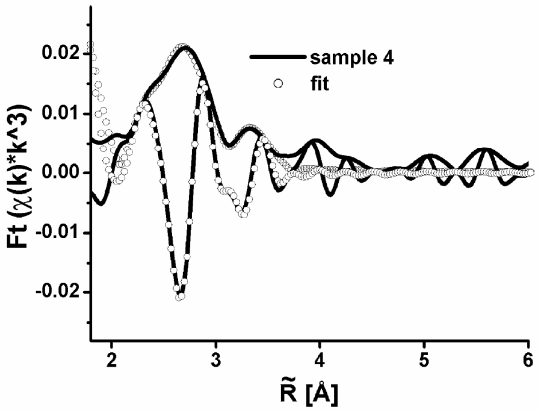

Fig. 7. mRDF of the host/guest compound after the fourth impregnation/calcination cycle (sample 4) and the result of the corresponding least-squares fit.

only significant shells up to 3.7 Å are present. This is due to the small particle sizes or static disorder effects. Compared to bulk haematite, the Fe–O shells are mostly unchanged in the samples, but the Fe–Fe shells are strongly reduced because of the nanostructural order of the iron (III) oxide.

Bulk haematite, which is isostructural with corundum, consists of FeO_6 octahedra. Regarding the modified radial distribution function of haematite in Fig. 6 in the range between 0.8 and 3.7 Å several coordination shells can be distinguished. The shell in the range of 0.8–1.9 Å comprises the first two coordination spheres of the iron with oxygen as nearest neighbor. In the range between 1.9 and 3.7 Å the iron–iron coordination shells appear. They can be divided into four shells due to the different linkage of the FeO_6 octahedra [27]. The coordination shells up to 3.28 Å are formed by face- and edge-shared octahedra, the coordination shells at higher distances are due to a corner-shared linkage.

As an example, Fig. 7 shows the modified radial distribution function of sample 4 and the least-squares fit; the refined structure parameters of the sample 4 and bulk haematite as well as single crystal data are listed in Table 3. The EXAFS results of bulk haematite are in good agreement with results extracted from single crystal data. In contrast to bulk haematite, a reduction of the coordination number in the host/guest compound is observed which is due to the small particle size and static disorder effects of the iron (III) oxide. In contrast to bulk haematite the first iron–iron shell

Table 3
Refined structure parameters of the Fe–Fe shells of the host/guest compound after the fourth impregnation/calcination cycle (sample 4) and bulk haematite as reference as well as corresponding results extracted from single-crystal data of haematite[a]

	Sample 4	Bulk haematite	Haematite s.c. [27]
N	0.44	0.50	1
R [Å]	2.94	2.88	2.89
$\Delta\sigma^2$ [Å^2]	0.0042	0.0039	–
N	0.91	3	3
R [Å]	2.99	2.96	2.96
$\Delta\sigma^2$ [Å^2]	0.0047	0.0039	–
N	0.29	3	3
R [Å]	3.18	3.38	3.35
$\Delta\sigma^2$ [Å^2]	0.0013	0.0040	–
N	0.55	4.03	6
R [Å]	3.46	3.69	3.69
$\Delta\sigma^2$ [Å^2]	0.0042	0.0040	–
ΔE_0	−2.04	−6.81	

[a] N: coordination number; R: bond length; $\Delta\sigma^2$: Debye–Waller factor; ΔE_0: energy shift; s.c.: single crystal data.

of the nanoparticles appears at 2.94 Å, a distance which is in between face-shared (<2.9 Å) and edge-shared (2.95–3.28 Å) iron oxide octahedra [28]. Taking all this into account we assume that the first three iron–iron shells are formed by edge-shared and the fourth by corner-shared octahedra.

4. Conclusions

It can be concluded that iron (III) oxide is formed within the pore system of mesoporous carbon CMK-1. To obtain different amounts of iron (III) oxide inside the mesopores of CMK-1 various numbers of wet impregnation/drying and calcination cycles were applied. By using powder X-ray diffractometry, nitrogen physisorption, Raman spectroscopy and transmission electron microscopy it could be shown that iron (III) oxide nanoparticles were almost exclusively formed inside the preserved pore system of the mesoporous carbon host structure. The local structure of iron oxide was determined by X-ray absorption spectroscopy. It revealed slightly disordered iron (III) oxide nanoparticles and the absence of other iron oxides.

Acknowledgements

Financial support by the Deutsche Forschungsgemeinschaft (Fr 1372/2-2) and the Fonds der Chemischen Industrie is gratefully acknowledged. We thank HASYLAB@DESY for allocating beamtime.

Finally we would like to thank Dr. Peter Klar and Martin Güngerich from the Department of Physics at the Philipps-University Marburg (Germany) for carrying out the Raman spectroscopic measurements.

References

[1] R. Ryoo, S.H. Joo, S. Jun, J. Phys. Chem. B 103 (1999) 7743.
[2] R. Ryoo, S.H. Joo, S. Jun, T. Tsubakiyama, O. Terasaki, in: A. Galarneau, F. di Renzo, F. Fajula, J. Vedrine (Eds.), Zeolites and Mesoporous Materials at the Dawn of the 21st Century, Studies in Surface Science and Catalysis, vol. 135, Elsevier, Amsterdam, 2001, p. 1121.
[3] H. Darmstadt, C. Roy, S. Kaliaguine, S.J. Choi, R. Ryoo, Carbon 40 (2002) 2673.
[4] H. Darmstadt, C. Roy, S. Kaliaguine, S.J. Choi, R. Ryoo, Carbon 2001, International Conference on Carbon, Lexington, USA, 2001, p. 673.
[5] R. Köhn, D. Paneva, M. Dimitrov, T. Tsoncheva, I. Mitov, C. Minchev, M. Fröba, Micropor. Mesopor. Mater., accepted.
[6] C.R. Bansal, J.B. Donnet, F. Stoeckli, Active Carbon, Marcel Dekker, New York, 1988, p. 126.
[7] H.C. Foley, Micropor. Mater. 4 (1995) 407.
[8] J. Lee, S. Yoon, T. Hyeon, S.M. Oh, K.B. Kim, Chem. Commun. (1999) 2177.
[9] R. Ryoo, S.H. Joo, M. Kruk, M. Jaroniec, Adv. Mater. 13 (9) (2001) 677.
[10] S.H. Joo, S.J. Choi, I. Oh, J. Kwak, Z. Liu, O. Terasaki, R. Ryoo, Nature 412 (2001) 169.
[11] M. Fröba, R. Köhn, G. Bouffaud, Chem. Mater. 11 (1999) 2858.
[12] R. Köhn, F. Brieler, M. Fröba, in: A. Sayari, M. Jaroniec, T.J. Pinnavaia (Eds.), Nanoporous Materials II, Studies in Surface Science and Catalysis, vol. 129, Elsevier, Amsterdam, 2000, p. 341.
[13] R. Köhn, M. Fröba, Catal. Today 68 (2001) 227.
[14] (a) C.T. Kresge, M.E. Leonowicz, W.J. Roth, J.C. Vartuli, J.S. Beck, Nature 359 (1992) 710;
(b) J.S. Beck, J.C. Vartuli, W.J. Roth, M.E. Leonowicz, C.T. Kresge, K.D. Schmitt, C.T.-W. Chu, D.H. Olson, E.W. Sheppard, S.B. McCullen, J.B. Higgins, J.L. Schenkler, J. Am. Chem. Soc. 114 (1992) 10835.
[15] S.H. Joo, S. Jun, R. Ryoo, Micropor. Mesopor. Mater. 44–45 (2001) 153.
[16] S. Brunauer, P.H. Emmet, E. Teller, J. Am. Chem. Soc. 60 (1938) 309.
[17] E.P. Barrett, L.G. Joyner, P.P. Halenda, J. Am. Chem. Soc. 73 (1951) 373.
[18] T. Ressler, J. Synchrotron Rad. 5 (1998) 118.
[19] J.J. Rehr, J. Mustre de Leon, S.I. Zabinsky, R.C. Albers, J. Am. Chem. Soc. 113 (1991) 5135.
[20] U. Ciesla, F. Schüth, Micropor. Mesopor. Mater. 27 (1999) 131.
[21] A. Saito, H.C. Foley, AIChE J. 37 (1991) 429.
[22] M. Thommes, R. Köhn, M. Fröba, in: K.K. Unger, G. Kreysa, J.P. Baselt (Eds.), Characterization of Porous Solids V, Studies in Surface Science and Catalysis, vol. 128, Elsevier, Amsterdam, 2000, p. 259.
[23] M. Thommes, R. Köhn, M. Fröba, J. Phys. Chem. B 104 (2000) 7932.
[24] M. Thommes, R. Köhn, M. Fröba, Appl. Surf. Sci. 196 (2002) 239.
[25] K.S.W. Sing, D.H. Everett, R.A.W. Haul, L. Mouscou, R.A. Pierotti, J. Rouquerol, T. Siemieniewska, Pure Appl. Chem. 57 (1985) 603.
[26] M.S. Dresselhaus, M.A. Pimenta, P.C. Eklund, G. Dresselhaus, Raman scattering in fullerenes and related

carbon-based materials, in: W.H. Weber, R. Merlin (Eds.), Raman Scattering in Materials Science, Springer-Verlag, Berlin-Heidelberg, 2000, p. 314 (Chapter 8).
[27] R.L. Blake, R.E. Hessevick, T. Zoltai, L.W. Finger, Am. Mineral. 51 (1966) 123.
[28] A. Manceau, V.A. Drits, Clay Miner. 28 (1993) 165.

A new *in situ* cell for XAFS investigations

Holger Huwe and Michael Fröba*

Institute of Inorganic and Analytical Chemistry, Justus Liebig University Giessen, Heinrich-Buff-Ring 58, D-35392 Giessen, Germany.
E-mail: michael.froeba@anorg.chemie.uni-giessen.de

A new *in situ* cell for X-ray absorption spectroscopic investigations has been designed and tested. In contrast to existing cells, it is able to reach temperatures as high as 1250 K and can record X-ray absorption spectra in transmission and fluorescence modes. Furthermore, the cell is equipped with a new sample-holder system which allows an easy sample changing. All components are commercial and are simple to build. The cell is light and easy to handle, and can be used under reducing or oxidizing conditions which makes it suitable for performing reduction and oxidation investigations as demanded, *e.g.* in heterogeneous catalysis experiments. The cell was tested on the reduction of haematite.

Keywords: X-ray absorption spectroscopy; *in situ* cells; instrumentation; *in situ* XAFS.

1. Introduction

Interest in *in situ* experiments using X-ray absorption spectroscopy has been on the increase in recent years. The possibility of performing time- and temperature-resolved experiments has lead to the design of different *in situ* cells for several approaches (Jentoft *et al.*, 2004; Ressler, 2003; Pettiti *et al.*, 1999; van Bokhoven *et al.*, 1999; Kampers *et al.*, 1989; Dent *et al.*, 1995; Zhang *et al.*, 1991). Most of them are used in the study of catalysts (Ressler *et al.*, 2003; Wienold *et al.*, 2003).

Here we report on the construction of a new *in situ* cell with a wide range of applications. The cell is of a simple design – the use of special and complex manufactured parts has been avoided. All of the parts used are not expensive and can be assembled in a common machine shop. In addition, the cell is light, easy to handle and robust.

The sample-holder system was constructed for the housing of sample pills. It allows a very simple sample changing combined with a reproducible setting with respect to the sample position. The chosen material and design benefit the temperature distribution as well as gas changes during the measurements.

The most important advantage of the cell is the combination of several features known from other cells (*e.g.* high temperature without fluorescence yield detection). The cell makes *in situ* XAFS studies possible for elements with an absorption of X-rays over a wide range. Simultaneous detection of transmission and fluorescence yield is possible. During experiments the temperature can be varied from room temperature up to 1250 K. A wide choice of gas mixtures for reduction and oxidation cycles is conceivable.

2. *In situ* cell

The cell consists of three main parts: (i) the reaction room, which accommodates (ii) the sample holder, and (iii) the gas and temperature control system.

The main part of the reaction room is a T-shaped quartz tube (25 mm in diameter), around which are wrapped a heating wire and copper cooling tubes. An S-shape winding of the heating wire allows a nearly uniform temperature distribution at the sample position. In order to attach the wire and to gain a better temperature assignment the heating wire was built of oven cement. The area of constant temperature was estimated to be an area 7.5 mm × 7.5 mm around the sample position.

The ends of the tube are closed using brass flanges, which consist of an end cap, a spacer, a gasket and a screw holder. The end caps are bored 25 mm in diameter and equipped with an epoxy-sealed Kapton polyimide foil (of thickness 50 µm) for the X-ray beam to pass through. Changing the window material (*e.g.* to beryllium) is possible if necessary. Each of the two spacers is equipped with a tube for gas inlet or outlet. In addition, one spacer carries and fixes the thermocouple (Pt10%Rh/Pt), which is embedded in a ceramic tube, positioned such that its end is close to the sample position and at 2 mm from the quartz wall. The set-up is shown schematically in Fig. 1, and Figs. 2, 3 and 4 show different views of the entire cell. Important cell parameters are listed in Table 1.

First investigations show that it is possible to reduce the size of the entire cell by more than a half without restricting any of the features described above. This might be useful for space-restricted beamlines or for increasing the transmission and fluorescence yields.

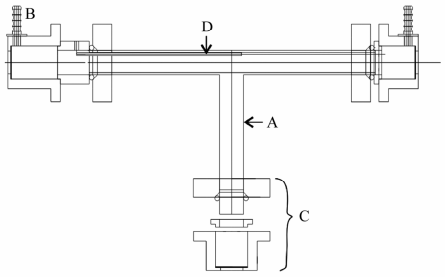

Figure 1
Construction drawing of the *in situ* cell. A: quartz tube; B: reaction gas intake or release flow socket; C: flange consisting of end cap, spacer, gasket and screw holder; D: thermocouple.

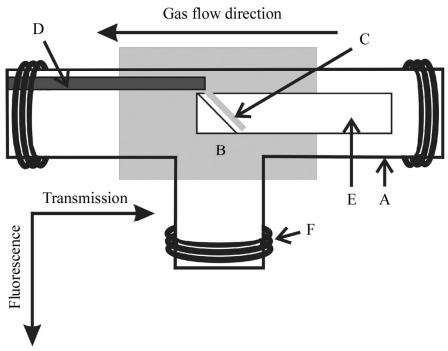

Figure 2
Schematic drawing of the *in situ* cell. A: T-shaped quartz tube; B: heating area (shaded); C: sample position; D: thermocouple; E: sample holder; F: water-cooling unit of the fluorescence arm.

 DOI: 10.1107/S0909049504013858

Table 1
Cell parameters.

Parameter	Value
Dimensions (length × width × height)	400 × 300 × 150 mm
Sample–transmission window distance	190 mm
Sample–fluorescence window distance	100 mm
Temperature range	Room temperature to 1250 K
Heating power	540 W (maximum 10 A, 50 V)
Heating resistor	5.4 Ω
Thermocouple	Pt10%Rh/Pt
Constant-temperature length	15 mm

The design and construction of this cell offers some technical and safety advantages, *e.g.* the structural separation between the electric (especially the heating area) and the water-cooling parts. In addition, the sample and the experimental gas are physically separated from the electric and heating wires.

The sample holder consists of a specially cut quartz tube as shown in Fig. 5. The sample, pressed as a boron nitride pellet (maximum diameter 16 mm), is mounted at an angle of 45° to the direction of the cut quartz tube. The quartz tube is specially cut to avoid any shielding of the fluorescence radiation. The reaction gas impinges on the sample after flowing through the tube. This makes it possible to switch gases while ignoring the gas mixture in the fluorescence arm of the cell.

In order to change the sample, one of the end caps has to be removed. The sample holder is then inserted into the furnace up to the desired position (marked on the outside) and the end cap is then replaced.

The *in situ* cell operates with a programmable temperature controller (Eurotherm 815S) with the possibility of performing heating ramps. The temperature allocations during these ramps are shown in Fig. 6. The temperature curves are recorded under real conditions (*i.e.* at the sample position with a nitrogen gas flow of 5 cm^3 min^{-1}, water cooling and aligned sample holder). It can be clearly seen that after a self-optimization procedure of the controller the differences between the desired and the real temperature are marginal over a large temperature range.

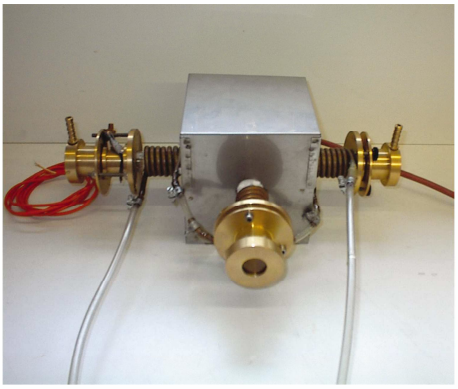

Figure 3
The entire cell viewed from the side.

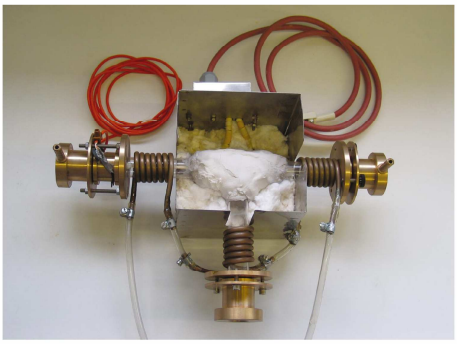

Figure 4
The entire cell viewed from the top, with the top of the box and the thermal insulation removed.

3. EXAFS measurements

First tests were carried out at the HASYLAB@DESY EXAFSII beamline E4. The cell was tested in an experiment on the reduction of bulk haematite.

For the *in situ* measurements, bulk haematite was pressed into a boron nitride pellet of diameter 10 mm and thickness 0.5 mm. The reaction gas was 5% hydrogen in nitrogen with a flow rate of 5 cm^3 min^{-1} and a heating rate of 2° min^{-1}. XAFS spectra were

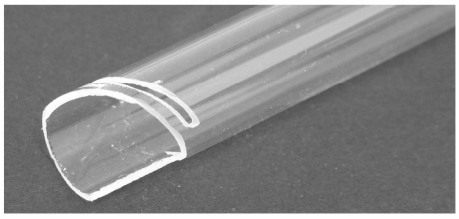

Figure 5
Quartz sample holder.

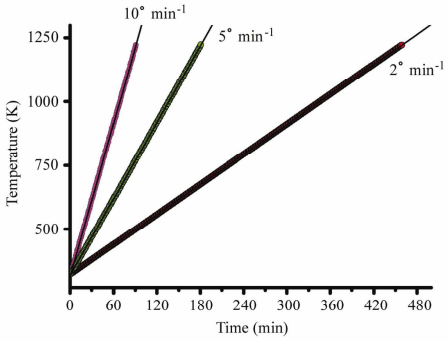

Figure 6
Temperature allocation for three heating ramps, collected after previous self-optimization of the controller/cell system. The temperature curves were recorded under real conditions (*i.e.* with nitrogen gas flow, water cooling and aligned sample holder) at the point of the sample position.

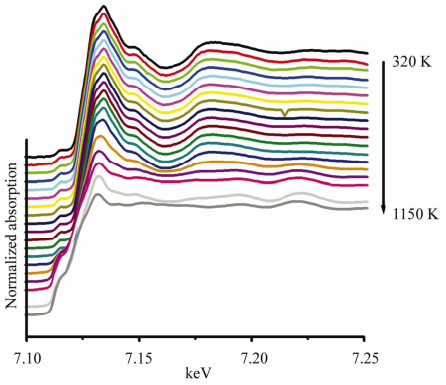

Figure 7
In situ XANES spectra of the reduction of bulk haematite (transmission).

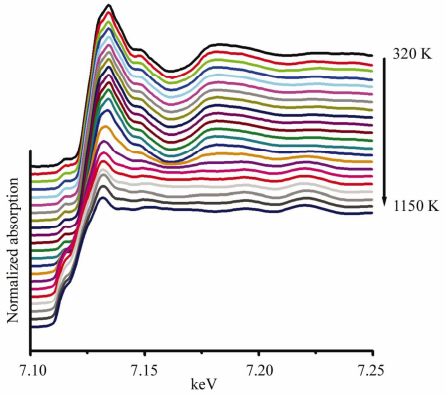

Figure 8
In situ XANES spectra of the reduction of bulk haematite (fluorescence).

recorded in a temperature range from 320 K up to 1150 K. It should be mentioned that the spectra were not collected in equidistant temperature steps. This is due to the different temperature ranges where a reduction to the respective iron oxides appears.

Figs. 7 and 8 show the corresponding energy-calibrated normalized background-corrected XANES spectra recorded at the Fe *K* edge in transmission and fluorescence mode, respectively. For both, a temperature-dependent change of the pre-edge peak is observed, combined with modifications in the white line and in the EXAFS oscillations. Evaluation of the spectra using principle component analysis shows the appearance of four different phases for both the transmission and fluorescence spectra series. These phases are α-Fe_2O_3 (<570 K), Fe_3O_4 (570 K), FeO (640 K) and Fe^0 (>1050 K), as expected (Webb & Orr, 1997). The proportions of the different iron phases in the transmission and fluorescence series are the same at respective temperatures. All these results demonstrate the usage of the *in situ* cell.

4. Conclusions

A new XAFS *in situ* cell has been designed, constructed and applied. It is able to reach temperatures up to 1250 K and can record X-ray absorption spectra in transmission and fluorescence modes. The sample holder allows for simple sample changing. The cell was successfully used in the reduction of haematite.

Financial support by the Fonds der Chemischen Industrie is gratefully acknowledged. We would like to thank HASYLAB@DESY for allocating beam time and the HASYLAB staff for supporting us. Thanks to Ralf Sack (head of our machine shop) for building the cell.

References

Bokhoven, J. A. van, van der Eerden, A. M. J., Smith, A. D. & Koningsberger, D. C. (1999). *J. Synchrotron Rad.* **6**, 201–203.
Dent, A. J., Greaves, G. N., Roberts, M. A., Sankar, G., Wright, P. A., Jones, R. H., Sheehy, M., Madill, D., Catlow, C. R. A., Thomas, J. M. & Rayment, T. (1995). *Nucl. Instrum. Methods Phys. Res. B*, **97**, 20–22.
Jentoft, R. E., Hahn, A. H. P., oft, F. C. & Ressler, T. (2004). *Phys. Scr.* Accepted.
Kampers, F. W. H., Maas, T. M. J., van Groundelle, J., Brinkgreve, P. & Koningsberger, D. C. (1989). *Rev. Sci. Instrum.* **60**, 2635–2638.
Pettiti, I., Gazzoli, D., Inversi, M., Valigi, M., De Rossi, S., Ferraris, G., Porta, P. & Colonna, S. (1999). *J. Synchrotron Rad.* **6**, 1120–1124.
Ressler, T. (2003). *Anal. Bioanal. Chem.* **376**, 584–593.
Ressler, T., Wienold, J., Jentoft, R. E. & Girgsdies, F. (2003). *Eur. J. Inorg. Chem.* **2**, 301–312.
Webb, P. A. & Orr, C. (1997). *Analytical Methods in Fine Particle Technology*, p. 265. Norcross, GA: Micromeritics Instruments. (ISBN 0–9656783-0-X.)
Wienold, J., Timpe, O. & Ressler, T. (2003). *Chem. Eur. J.* **9**, 6007–6017.
Zhang, Z., Chen, H. & Sachtler, W. M. H. (1991). *J. Chem. Soc. Faraday Trans.* **87**, 1413–1418.

Jointly published by
Akadémiai Kiadó, Budapest
and Kluwer Academic Publishers, Dordrecht

React.Kinet.Catal.Lett.
Vol. 83, No. 2, 299-305
(2004)

RKCL4530

IRON MODIFIED MESOPOROUS CARBON AND SILICA CATALYSTS FOR METHANOL DECOMPOSITION

Tanya Tsoncheva[a*], Daniela Paneva[b], Ivan Mitov[b], Holger Huwe[c], Michael Fröba[c], Momtchil Dimitrov[a] and Christo Minchev[a]

[a] Institute of Organic Chemistry, Bulgarian Academy of Sciences, Sofia 1113, Bulgaria,
[b] Institute of Catalysis, Bulgarian Academy of Sciences, Sofia 1113, Bulgaria,
[c] Institute of Inorganic and Analytical Chemistry, Justus-Liebig-University Giessen, Germany

Received March 10, 2004
Accepted June 22, 2004

Abstract

Iron modified silica and carbon mesoporous materials with similar textural characteristics are compared in methanol decomposition to H_2, CO and CH_4. The influence of the support on the phase composition and reductive properties of the catalysts is studied by Mössbauer spectroscopy and TPR with hydrogen.

Keywords: Fe_2O_3/mesoporous silica or carbon, methanol decomposition, Mössbauer spectroscopy

INTRODUCTION

In the last decades methanol has been regarded as a suitable alternative source for hydrogen production. For the purpose, various processes are proposed and among them, catalytic methanol decomposition gains considerable interest [1]. In our previous studies we demonstrated that in the case of nanosized iron oxide supported on mesoporous silicas catalysts the selectivity of this process could be successfully controlled by the state of the iron particles [2-4]. It was also shown that the dispersion and phase transformations of the supported iron species essentially vary with the preparation conditions used, support textural characteristics and with the influence

*Corresponding author. E-mail: ormm@orgchm.bas.bg

0133-1736/2004/US$ 20.00.

of the reaction medium as well. The aim of the present paper is to study the catalytic behavior in methanol decomposition of iron oxide supported on silica and carbon mesoporous materials. The compared supports (MCM-48 *vs* CMK-1 and SBA-15 *vs* CMK-3) possess similar textural characteristics, since the mesoporous carbons are prepared by silica-templated synthesis [5] from the corresponding ordered mesoporous silicas.

EXPERIMENTAL

The parent mesoporous silica (MCM-48 and SBA-15) and carbon (CMK-1 and CMK-3) molecular sieves were synthesized by standard procedures [3,6] and are characterized with BET surface areas of 1256, 543, 660 and 510 m^2/g, respectively. The Barret-Joyner-Halenda (BJH) pore diameters are about 3.7 (SBA-15 and CMK-3) and 2.5 nm (MCM-48 and CMK-1). The template-free materials were impregnated with 0.5 M aqueous solution of $Fe(NO_3)_3$, dried at room temperature and calcined in a flow of air at 650-670 K for 6 h. The samples were denoted as Fe/S48, Fe/S15, Fe/C1 and Fe/C3 for MCM-48, SBA-15, CMK-1 and CMK-3 supports, respectively. The materials obtained were characterized by X-ray diffraction and nitrogen physisorpton as described in Ref. [3,6]. The iron content in the samples is about 3.5 wt.%. The Mössbauer spectra (MS) were obtained at room temperature as it is described in [2-4]. The parameters of hyperfine interaction: isomer shift (IS), quadrupole splitting (QS) and effective internal magnetic field (H_{eff}) as well as the line widths (FWHM) and the relative weight (G) of the partial components of the spectra were determined. The temperature-programmed reduction–thermogravimetric measurements (TPR-TG) were performed in a SETARAM TGDTA 92 microbalance in flow of H_2 in Ar (50%) with 5 K/min. The methanol decomposition was carried out in a flow type apparatus with methanol partial pressure of 1.57 kPa, WHSV of 1.5 h^{-1} and heating rate of 2 K/min in the range 350 – 700 K. Experiments at 670 K were also done. The catalysts were pretreated at 770 K for 2 h in air or Ar for the silicate and carbon samples, respectively. On-line GC analysis was used.

RESULTS AND DISCUSSION

The X-ray diffraction patterns and physisorption measurements of the samples show that iron modification does not affect substantially the structure of the mesoporous materials [3,6]. In the high angle region only very low or no reflections typical of iron oxide have been found (not shown). More detailed

information concerning the state of the supported iron species was obtained by MS spectroscopy (Table 1). All spectra consist of two-line components (Dbl) with parameters typical of hematite (Table 1) that could be ascribed to ultrafine particles (below 10 nm) with superparamagnetic (SPM) behavior. Only in the case of Fe/C1, a six-line (Sxt) component with reduced value of H_{eff} and broadened line width is registered as well (Table 1). The presence of doublet and sextet components in this sample is evidence for the broad size distribution of hematite particles (up to 12-13 nm). In order to describe the iron species more precisely, an idealized core-shell model [3] is applied for the doublets in the MS spectra (Table 1). The doublet with higher QS values (Dbl2) is associated with surface iron atoms while the doublet with

Table 1

Mössbauer parameters of iron supported mesoporous silica and carbon samples

Sample	Components	IS (mm/s)	QS (mm/s)	H_{eff} (T)	FWHM (mm/s)	G (%)
Fe/S15	Dbl 1-Fe_2O_3-SPM, core	0.36	0.71	-	0.48	76
	Dbl 2-Fe_2O_3-SPM, shell	0.36	1.15	-	0.68	24
Fe/S48	Dbl 1-Fe_2O_3-SPM, core	0.34	0.63	-	0.43	51
	Dbl 2-Fe_2O_3-SPM, shell	0.33	1.13	-	0.65	49
Fe/C3	Dbl 1-Fe_2O_3-SPM, core	0.35	0.70	-	0.61	73
	Dbl 2-Fe_2O_3-SPM, shell	0.34	1.63	-	1.20	27
Fe/C1	Sx Fe_2O_3	0.36	-0.10	26.6	1.85	54
	Dbl Fe_2O_3-SPM	0.35	0.75	-	0.54	46

lower QS values (Dbl1) belongs to iron atoms from the core of the particles. The higher ratio of the core to surface ions, which is registered for Fe/S15 and Fe/C3 in comparison with Fe/S48, could be an indication for the presence of larger iron oxide particles in the former materials. Moreover, on the basis of these values, the existence of iron particles with very similar sizes for Fe/S15 and Fe/C3 could be assumed (Table 1). So, in the case of the mesoporous materials with larger pore diameter (SBA-15 and the corresponding CMK-3), practically no influence of the support nature on the initial state of the catalysts is established. On the contrary, for the samples with smaller mesopores (MCM-48 and the corresponding CMK-1), smaller iron oxide particles are registered for the silica based sample (Fe/S48). Thus, both textural and hydrophobic

characteristics of the support seems to control the dispersion of the iron oxide species and the textural factor has decisive effect only in the case of silica based materials.

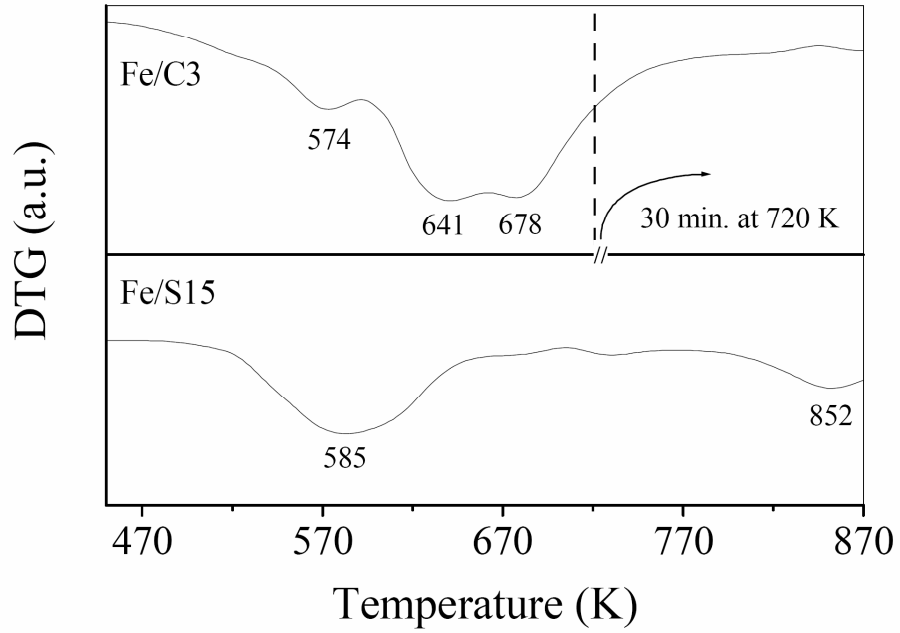

Fig. 1. DTG curves registered during TPR experiments for Fe/C3 and Fe/S15

The TPR behavior of Fe/S15 and Fe/C3 samples, obtained on different supports and characterized by very close initial state of the iron oxide (Table 1) is compared in Fig. 1. The observed reduction peaks in the temperature interval 450-720 K could be associated with Fe(III)→Fe(II) and Fe(II)→Fe(0) reduction transitions depending on the dispersion of the iron oxide particles and the support used. Two general effects could be assumed. A broad, not clearly defined peak with maximum at about 585 K is found for Fe/S15. In contrast, three peaks (at 574, 641 and 678 K) are registered in the TPR pattern of Fe/C3. At the same time, different reductive changes during the TPR experiments are established by MS and XRD data. Metallic iron (about 80 %) is found for Fe/C3, while predominantly Fe(III) → Fe(II) transition and about 50% unchanged iron(III) oxide species are registered for Fe/S15. Similar effects are established for Fe/C1 and Fe/S48 as well. Thus, “easier” reduction in the case of carbon based materials could be assumed and it could be due not only to the reductive properties of the carbon but also to the weaker iron oxide–support interaction in this case. The latter is in accordance with Ref. [7], where

graphite-like character and presence of few functional groups for the mesoporous carbon are reported. On the contrary, the existence of silanol nests, together with the preferable location of the iron species at these sites in the silicas [8], provoke strong iron oxide–support interaction.

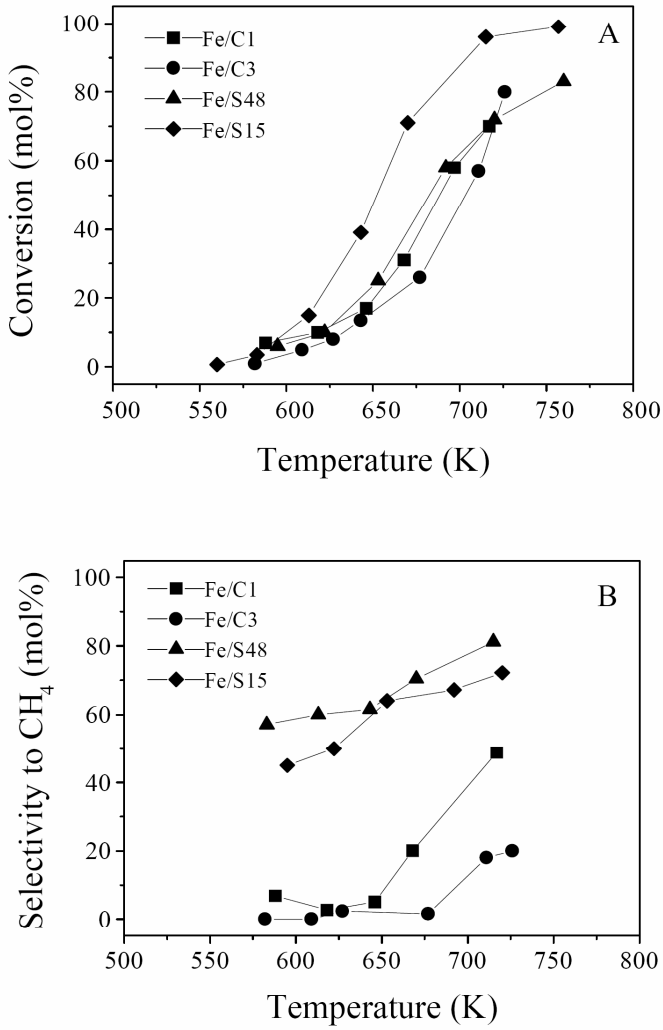

Fig. 2. Total conversion (A) and methane selectivity (B) *vs* temperature for various samples

The temperature dependencies of methanol conversion and methane selectivity are presented in Fig. 2A and Fig. 2B, respectively. The samples exhibit significant catalytic activity above 650 K and the main registered carbon-containing products are CO and CH_4 in all cases. However, higher capability for methane formation is observed for the silica based materials. These results are also confirmed by the catalytic experiments at 670 K. About

90% selectivity to methane is registered for both Fe/S15 and Fe/S48 after 60 min time on stream. On the contrary, under the same conditions, it is 15% and 20% for Fe/C1 and Fe/C3, respectively.

After the catalytic test, the MS spectra show clearly defined changes mainly in the case of Fe/S15 and Fe/C3. The appearance of a new sextet component with parameters characteristic of highly dispersed magnetite with G=9% and 75% for Fe/S15 and Fe/C3, respectively is found. Thus, as a whole, reductive transition under the reaction medium occurs, but despite the similar initial state of Fe/S15 and Fe/C3, it is more significant for the latter sample. The reductive properties of the carbon support could not be ignored as a possible reason for this result. However, the maintenance of higher relative part of unchanged SPM Fe_2O_3 in Fe/S15 (G=91%) in comparison with Fe/C3 (G=25%) could be an indication also for the stronger iron oxide–support interaction in the former sample.

In our previous investigations [2-4], a relation between the phase composition of the iron oxide supported on mesoporous silica materials and their behavior in methanol decomposition was established. There, the higher selectivity to CH_4 or CO was ascribed to the iron oxide transformations due to the reaction medium to magnetite or iron carbide, respectively. However, in the present study the observed phase transformations for the carbon based materials after the catalytic test could not explain their lower selectivity to methane. Taking into account the similar textural characteristics and the close initial state of iron oxide, especially for Fe/S15 and Fe/C3, a specific effect of the support nature could be proposed. As was mentioned above, stronger iron oxide–support interaction in the case of silica supported materials could be assumed on the basis of MS and TPR data. In this aspect, higher electron iron–support exchange for the obtained silica materials could be expected. As a result the C-O bond cleavage in the methanol molecule seems to be facilitated leading to methane formation [9,10]. At the same time, the predominant formation of methoxides and their following decomposition to CO and H_2 could be expected for the carbon-based materials [11,12].

In conclusion, variations in the catalytic and reductive properties as well as in the phase transformations of iron oxide supported materials could be achieved by changing the support nature. Higher selectivity to H_2 and CO is obtained when mesoporous carbon is used as a support instead of silica based mesoporous materials.

Acknowledgement. Financial support from the National Science Fund at the Ministry of Education and Science of Bulgaria (Project X-1208), Bulgarian Academy of Sciences and the Deutsche Forschungsgemeinschaft is gratefully acknowledged.

REFERENCES

1. J. Agrell, B. Lindstroem, L.J. Pettersson, S. Jaras: *Catalysis*, **16**, 67 (2002).
2. R. Köhn, D. Paneva, M. Dimitrov, T. Tsoncheva, I. Mitov, C. Minchev, M. Fröba: *Microporous Mesoporous Mater.,* 63, 125 (2003).
3. C. Minchev, H. Huwe, T. Tsoncheva, M. Dimitrov, D. Paneva, I. Mitov, M. Fröba: *Stud. Surf. Sci. Catal*., accepted, 2004.
4. T. Tsoncheva, M. Dimitrov, D. Paneva, I. Mitov, R. Köhn, M. Fröba, C. Minchev: *React. Kinet. Catal. Lett*., **74**, 385 (2001).
5. R. Ryoo, S.H. Joo, S. Jun: *J. Phys. Chem. B*, **103**, 7743 (1999).
6. H. Huwe, M. Fröba: *Microporous Mesoporous Mater*., **60**, 151 (2003).
7. H. Darmstadt, C. Roy, S. Kaliaguine, S.J. Choi, R. Ryoo*: Carbon 2001, International Conference on Carbon,* Lexington, Kentucky, USA, 2001.
8. M. Stockenhuber, M.J. Hudson, R.W. Joyner: *J. Phys. Chem. B*, **104**, 3370 (2000).
9. R.J. Levis, J. Zhicheng, N. Winograd: *J. Am. Chem. Soc*., **110**, 4431 (1988)
10. R.J. Levis, J. Zhicheng, N. Winograd: *J. Am. Chem. Soc*., **111,** 4605 (1989).
11. M. Mavrikakis, M.A. Barteau: *J. Mol. Catal. A: Chemical,* **131,** 135 (1998).
12. N. Takezawa, N. Iwasa: *Catal. Today*, **36**, 45 (1997).

Available online at www.sciencedirect.com
SCIENCE DIRECT®
Microporous and Mesoporous Materials 81 (2005) 333–341
MICROPOROUS AND MESOPOROUS MATERIALS
www.elsevier.com/locate/micromeso

Iron oxide modified mesoporous carbons: Physicochemical and catalytic study ☆

Christo Minchev [a,*], Holger Huwe [b], Tanya Tsoncheva [a], Daniela Paneva [c], Momtchil Dimitrov [a], Ivan Mitov [c], Michael Fröba [b,*]

[a] Institute of Organic Chemistry, Bulgarian Academy of Sciences, Sofia 1113, Bulgaria
[b] Institute of Inorganic and Analytical Chemistry, Justus Liebig University Giessen, D-35392 Giessen, Germany
[c] Institute of Catalysis, Bulgarian Academy of Sciences, Sofia 1113, Bulgaria

Received 9 September 2004; received in revised form 9 February 2005; accepted 10 February 2005
Available online 7 April 2005

Abstract

Series of iron oxide supported on CMK-1 and CMK-3 materials obtained by impregnation from aqueous or organic media are studied by TPR, XAFS, Moessbauer spectroscopy and methanol decomposition as a catalytic test. More highly dispersed iron oxide particles are obtained using ethanolic impregnation medium, but their dispersion is affected to a low extent by the support pore structure. On the basis of the combined results on the state and reductive phase transformations of the loaded iron oxide particles, more accessible CMK-3 in comparison with CMK-1 pore structure is assumed.

Keywords: Nanostructured iron oxide; Mesoporous carbons; TPR; Moessbauer spectroscopy; Methanol decomposition; XAFS

1. Introduction

In the last years highly ordered mesoporous carbons of CMK-n type obtained by the template-synthesis [1–4] have gained a considerable interest as new nanostructured materials due to their potential applications as adsorbents, catalyst supports, hydrogen storage systems and host structures of advanced electronic materials. It is known that the pore structure of such type of material could be controlled readily by the tailoring of the pore wall thickness by the used silica template. For CMK-1 [5–7] and CMK-3 [8,9] obtained from MCM-48 and SBA-15 used as silica matrices, respectively, uniform mesopores of about 3 and 4.5 nm in size, high BET specific surface area and large pore volume are observed. A certain amount of micropores (below 0.9 nm) in both carbon materials is also found but their volume cannot be estimated precisely especially in the case of CMK-1 [3] up to now. The CMK-3 structure is visualised as hexagonally packed and rigidly interconnected carbon rods [9] while the CMK-1 structure is composed of two weakly contacting carbon networks and belongs to the tetragonal $I4_1/a$ or the monoclinic $C2/c$ space group [10,11]. However, despite the great progress in the investigation of these novel materials, the detailed characterization of the pore structure and connectivity seems to be an extremely difficult problem and is not fully understood [6,12,13].

It is known that iron supported on activated carbon has been applied in number of catalytic processes such

☆ Work presented at the International Mesostructured Materials Symposium, 1–4 May 2004, Cape Town, South Africa.

* Corresponding authors. Fax: +35928700225 (C. Minchev), Tel.: +49 641 99 34100; fax: +49 641 99 34109 (M. Fröba).
E-mail addresses: ormm@orgchm.bas.bg (C. Minchev), michael.froeba@anorg.chemie.uni-giessen.de (M. Fröba).

1387-1811/$ - see front matter © 2005 Elsevier Inc. All rights reserved.
doi:10.1016/j.micromeso.2005.02.015

as Fischer–Tropsch synthesis [14], CO and CO_2 hydrogenation [15], desulfurisation [16] and dehalogenation [17], ozone [18] or hydrogen sulfide decomposition [19], and catalytic removal of SO_2, NO and HCl [20]. The advantages of activated carbon over conventional inorganic supports are in its weak chemical interaction with the active phase and also in the formation of highly dispersed supported metal particles due to its high surface area and well developed porosity [21]. The ordered CMK mesoporous carbons, characterized with uniform pores, controllable pore diameters, high specific surface areas and large pore volumes, offer a new possibility to better control the loaded metal particles dispersion. In this relation, platinum, ruthenium and palladium modified CMK carbons have already been described as materials with remarkably higher catalytic activity compared to their analogues obtained on other carbons or inorganic supports [2,22,23].

In our previous work [24–26] we have established a good relationship between the dispersion of supported haematite nanoparticles on different mesoporous silicas, their reductive phase transformation and catalytic behaviour in methanol decomposition to hydrogen, carbon monoxide and methane. However, practically no information of that kind for the analogues mesoporous carbon based materials exists. For that reason, the aim of the present paper is to study the effect of the textural characteristics of CMK-1 and CMK-3 on the state, reductive and catalytic properties in methanol decomposition of the supported iron oxide. Special attention is paid to the comparison of the latter effects with the corresponding ones for the iron modified mesoporous silicas.

2. Experimental

2.1. Materials

The modified CMK-1 and CMK-3 materials were prepared as described in [27] by a wet impregnation procedure with 0.5 M (0.5Fe) or 5 M (5Fe) solutions of $Fe(NO_3)_3$ from aqueous (Method A) or ethanolic (Method B) medium, respectively. Using 0.5 and 5 M solutions, samples with 3% and 17 wt% iron content are obtained. The samples were dried under the following conditions: (i) at room temperature for 6 h in oil pump vacuum. Finally the impregnated materials were calcined in a flow of air at 623 K for 10 h leading to the transformation of the iron nitrate into iron oxide. The reference samples (0.5FeR and 5FeR with 3% and 17% iron, respectively) were prepared by the same impregnation procedure in aqueous medium. In this case a carbon material with not well developed porosity and a specific surface area of 180 m^2/g was used as a support.

2.2. Methods and apparatus

Powder X-ray diffraction (XRD) data were recorded on a Bruker AXS D8 advanced diffractometer (Cu Kα) in θ/θ geometry with a secondary monochromator. Nitrogen isotherms were recorded at 77 K using a static volumetric technique (Quantachrome Autosorb 1). Before the physisorption measurements the calcined samples were outgassed at 393 K for 15 h under vacuum. The pore size distributions were calculated using the adsorption or desorption branch of the sorption isotherm and applying the Barret–Joyner–Halenda (BJH) formula [28].

X-ray absorption spectroscopic measurements were carried out at the storage ring DORIS III (HASYLAB, DESY, Germany) at the EXAFS II beam line which was equipped with a Si(1 1 1) double crystal monochromator. The Fe K-edge spectra were recorded in fluorescence mode up to 4 times to improve the signal to noise ratio after summation. All samples were measured as fresh pressed boron nitride pellets. Data preparation (e.g. energy calibration, background removal, μ_0-setting, Fourier transformation) as well as data analysis were carried out with the program WinXAS3.0 [29]. For theoretical calculations the software FEFF7 [30] was used.

The TPR-TGA (temperature programmed reduction–thermogravimetric analysis) investigations were performed in a Setaram TG92 instrument. Usually, 40 mg of the sample were placed in a microbalance crucible and heated in a flow of 50 vol.% H_2 in Ar (100 cm^3/min) up to 723 K at 5 K/min and a final hold-up of 30 min. Prior to the TPR experiments the samples were treated in-situ in a flow of argon up to 773 K at a rate of 3 K/min followed by a hold-up of 1 h.

The Moessbauer spectra were obtained at room temperature with a Wissel (Wissenschaftliche Elektronik GmbH, Germany) electromechanical spectrometer working in a constant acceleration mode. A ^{57}Co/Cr (activity $\cong$ 10 mCi) source and an α-Fe standard were used. The experimentally obtained spectra were fitted to mathematical processing according to the least squares method. The parameters of hyperfine interaction such as isomer shift (IS), quadrupole splitting (QS), the effective internal magnetic field (H_{eff}), the line widths (FWHM), and the relative weight (G) of the partial components in the spectra were determined. In some cases the value of QS was calculated by a simple idealized core-shell model according to the Refs. [25,31].

2.3. Catalytic test

The catalytic experiments were performed in a fixed-bed reactor (0.1 g catalyst) at a methanol partial pressure of 1.57 kPa and a WHSV of 1.5 h^{-1} [25]. The temperature was raised with a rate of 1 K/min in the range of 350–700 K. Selected experiments were carried

out under isothermal conditions at 670 K and a WHSV of 2.5 h^{-1}. The on-line gas chromatographic analysis was performed on Porapak Q and molecular sieve columns using an absolute calibration method. Before the catalytic experiments the samples were pretreated in-situ in argon at 773 K for 2 h.

3. Results and discussion

3.1. Physicochemical characterization of iron modified mesoporous materials

3.1.1. Powder X-ray diffraction

Powder X-ray diffraction patterns show the preservation of the host structure after the impregnation process (Fig. 1). However, for all modified samples the X-ray peak intensities are reduced most probably due to pore filling. In the high angle region practically no reflections typical of iron oxide have been found, which is an evidence for the formation of nanosized iron oxide particles.

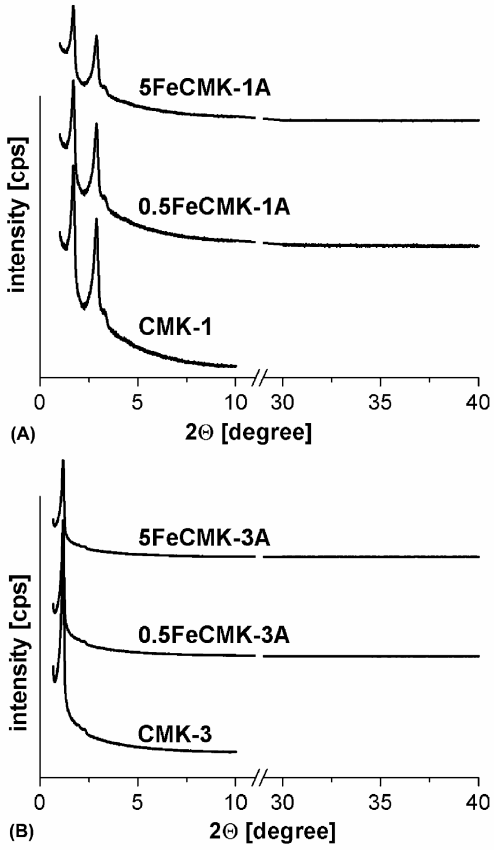

Fig. 1. PXRD of (A) CMK-1, 0.5FeCMK-1A and 5FeCMK-1A and (B) CMK-3, 0.5FeCMK-3A and 5FeCMK-3A.

3.1.2. Physisorption measurements

Figs. 2 and 3 exhibit the nitrogen physisorption isotherms of selected host/guest compounds as well as the corresponding pristine materials. All isotherms are of type IV (IUPAC classification [32]) typical for mesoporous materials. For all samples a reduced amount of physisorbed nitrogen combined with a small shift of the inflection point to lower values p/p_0 after loading is observed.

The pore size distributions (see the insets of Figs. 2 and 3) are slightly shifted to smaller values in contrast to the host materials. This effect is due to the mesopore filling with the iron oxide. Beside the reduction of the pore sizes, a slight broadening of the distributions is

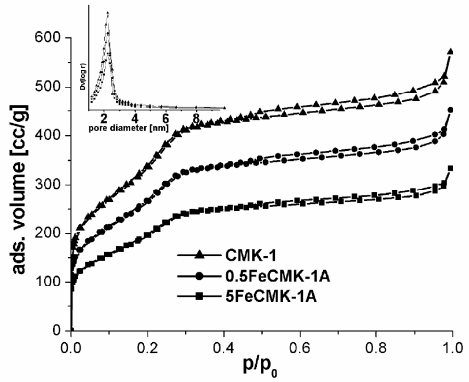

Fig. 2. Nitrogen adsorption/desorption isotherms (77 K) of CMK-1, 0.5FeCMK-1A and 5FeCMK-1A. Insets depict the corresponding pore diameter distributions (BJH) calculated from the adsorption branch.

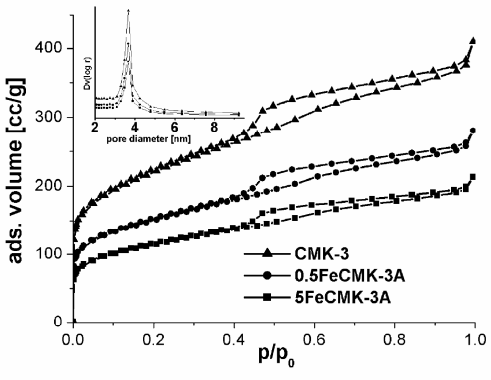

Fig. 3. Nitrogen adsorption/desorption isotherms (77 K) of CMK-3, 0.5FeCMK-3A and 5FeCMK-3A. Insets depict the corresponding pore diameter distributions (BJH) calculated from the desorption branch.

Table 1
N_2 physisorption data of the samples under investigation

Sample	S_{BET} [m^2/g]	D_p (BJH) [nm]	Fe_2O_3 content [weight %]	$S_{BET,red}$ [m^2/g]
CMK-1	1325	2.25	–	–
0.5FeCMK-1A	1049	2.20	3	40
0.5FeCMK-1B	1011	2.21	3	40
5FeCMK-1A	773	2.19	17	225
5FeCMK-1B	756	2.18	17	225
CMK-3	743	3.69	–	–
0.5FeCMK-3A	508	3.65	3	22
5FeCMK-3A	399	3.63	17	126
5FeCMK-3B	386	3.62	17	126

S_{BET}: total surface area by BET theory; D_p (BJH): BJH mean pore diameter; $S_{BET,red}$: reduction of the BET surface due to the introduction of Fe_2O_3.

observed for the host-guest compounds. A summary of the specific surface areas and the mean pore diameters of all compounds are listed in Table 1. One has to keep in mind that the loading of the host material itself leads to a reduction of the specific surface area. The values of these reductions as well as the weight contents of Fe_2O_3 are listed in Table 1, too.

3.1.3. X-ray absorption spectroscopy

X-ray absorption spectroscopic measurements were carried out at the Fe K-edge in order to prove the formation of nanostructured iron(III) oxide and to gain knowledge on the iron coordination. Fig. 4 exhibits exemplarily the Fourier transforms (not phase corrected) of the Fe K-edge EXAFS oscillations $\chi(k)*k^3$ of 0.5FeCMK-1A as well as of bulk haematite as reference compound. A strong reduction of the Fe–Fe shells is to be seen for all samples in contrast to bulk haematite. This effect is still known for nanosized iron oxides [27,33,34]. As an example, Fig. 5 shows the modified radial distribution function of a sample and the corresponding least-squares fit. The EXAFS results of bulk haematite are in good agreement with results extracted from single crystal data, see Table 2. In contrast to bulk haematite, a reduction of the coordination numbers in the host/guest compounds is observed. This is due to static disorder effects and small particle sizes of the iron(III) oxides. In contrast to bulk haematite the first iron–iron shells of the nanoparticles appear at about 2.90–2.95 Å, a distance which is in between face-shared (<2.9 Å) and edge shared (2.95–3.28 Å) iron oxide octahedra [35,36]. Taking all this into account we assume that the first three iron–iron shells are formed by edge shared and the fourth by corner-shared octahedra.

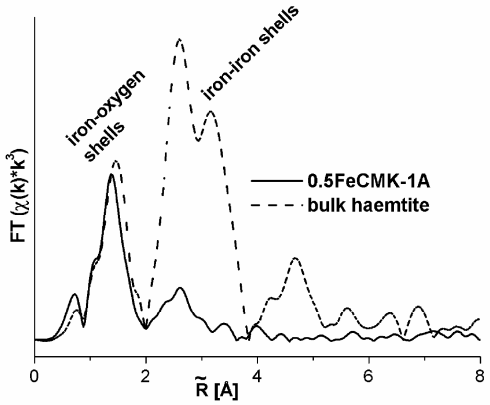

Fig. 4. Modified radial distribution function of the Fe K-edge oscillations $\chi(k)*k^3$ of 0.5FeCMK-1A and bulk haematite.

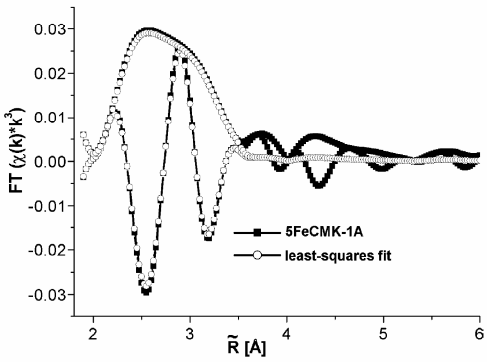

Fig. 5. Modified radial distribution function of 5FeCMK-1A and the results of the corresponding least-squares fit.

So far, the combination of the applied characterization methods show the preservation of the support structure during the wet impregnation process and the formation of nanosized haematite-like iron oxide predominantly inside the pores of the mesoporous host material [25,27,33].

3.1.4. Moessbauer spectroscopy

Further information upon the state of iron species was obtained by Moessbauer spectroscopy. The Moessbauer data of the air-pretreated samples are presented in Table 3. The recorded spectra (not shown) consist of lines of doublets (Dbl) and/or sextets (Sxt). The determined IS values are typical of high spin Fe(III) ions in octahedral co-ordination. The sextet component in all samples (except 0.5FeCMK-1A) is characterised with parameters close to those of α-Fe_2O_3 (Table 3). The low values of H_{eff} and asymmetrically broadened lines in the case of 0.5FeCMK-1A could be evidence for the presence of highly dispersed haematite-like particles (HD) with different sizes up to $D \approx 12$–13 nm. The doublet component in the spectra is assigned to iron (III) oxide with ultra-low particles sizes and superparamagnetic properties (SPM). Taking into account the CMK pore diameters the particle size with $D < 3$–4 nm could be assumed. However, the variations in the Sxt/Dbl

Table 2
Refined structure parameters of the Fe–Fe shells of different host/guest compounds and bulk haematite as reference as well corresponding results extracted from single-crystal data of haematite

	5FeCMK-1A	5FeCMK-1B	5FeCMK-3A	5FeCMK-3B	Bulk haematite	Haematite s.c.
N	0.63	0.75	0.52	0.66	0.99	1
R [Å]	2.94	2.93	2.90	2.91	2.89	2.89
$\Delta\sigma^2$ [Å^2]	0.004	0.004	0.004	0.004	0.004	–
N	1.31	1.47	1.27	1.29	2.99	3
R [Å]	3.00	2.99	2.99	2.99	2.97	2.96
$\Delta\sigma^2$ [Å^2]	0.005	0.004	0.004	0.005	0.004	–
N	0.66	0.70	0.71	0.69	3.01	3
R [Å]	3.19	3.21	3.20	3.20	3.37	3.35
$\Delta\sigma^2$ [Å^2]	0.002	0.003	0.003	0.002	0.004	–
N	0.60	0.59	0.82	0.78	5.13	6
R [Å]	3.48	3.49	3.60	3.62	3.68	3.69
$\Delta\sigma^2$ [Å^2]	0.004	0.004	0.004	0.003	0.004	
ΔE_0	−3.8	−4.9	−6.3	−3.9	−4.2	–

N: coordination number; R: bond length; $\Delta\sigma^2$: Debye–Waller factor; ΔE_0: energy shift; s.c.: single crystal data [25].

Table 3
Moessbauer parameters of air-pretreated samples

Sample	Components	IS [mm/s]	QS [mm/s]	H_{eff} [T]	FWHM [mm/s]	G [%]
0.5FeCMK-1A	Sxt-Fe_2O_3	0.36	−0.10	26.6	1.85	54
	Dbl-Fe_2O_3-SPM	0.35	0.75	–	0.54	46
0.5FeCMK-3A	Dbl 1-Fe_2O_3- SPM, core	0.35	0.70	–	0.61	73
	Dbl 2-Fe_2O_3-SPM, shell	0.35	1.63	–	1.20	27
5FeCMK-1A	Sxt-Fe_2O_3	0.37	−0.10	51.1	0.37	60
	Dbl-Fe_2O_3-SPM	0.35	0.74	–	0.53	40
5FeCMK-3A	Sxt-Fe_2O_3	0.37	−0.10	51.4	0.39	63
	Dbl-Fe_2O_3-SPM	0.34	0.74	–	0.62	37
0.5FeCMK-1B	Dbl 1-Fe_2O_3-SPM, core	0.35	0.66	–	0.44	56
	Dbl 2-Fe_2O_3-SPM, shell	0.35	0.99	–	0.66	44
5FeCMK-1B	Sxt-Fe_2O_3	0.38	−0.10	51.7	0.43	27
	Dbl-Fe_2O_3-SPM	0.35	0.80	–	0.59	73
5FeCMK-3B	Sxt-Fe_2O_3	0.38	−0.10	51.8	0.37	28
	Dbl-Fe_2O_3-SPM	0.35	0.82	–	0.53	72
0.5FeR	Dbl 1-Fe_2O_3-SPM, core	0.36	0.59	–	0.43	50
	Dbl 2-Fe_2O_3-SPM, shell	0.36	1.00	–	0.53	50
5FeR	Sxt-Fe_2O_3	0.37	−0.10	51.3	0.33	94
	Dbl-Fe_2O_3-SPM	0.36	0.74	–	0.50	6

IS: isomer shift; QS: quadrupole splitting; H_{eff}: effective internal magnetic field; FWHM: full line width at half maximum; G: relative weight of the partial components in the spectra; Dbl: doublet; Sxt: sextet.

components relative weights for the studied samples are observed and this could be ascribed to differences in the iron particles size distribution with their sizes. The higher relative weights of the doublet component (usually above 70%) which is found for the ethanolic samples in comparison with the corresponding aqueous ones (Table 3) could be an evidence for the higher iron oxide dispersion in the former materials. The favourable effect of the ethanolic medium on the supported iron oxide dispersion is well demonstrated for the samples with lower iron loading where only a Dbl component is found in the spectrum (0.5FeCMK-1B). For these samples an idealised core-shell model is applied in order to obtain more information from their spectra. The doublet with higher QS values is associated with surface iron atoms while the doublet with lower QS values belongs to iron atoms from the core of the particles. Here (0.5FeCMK-1B), the relative part of each type of ions is about 50% and it could be an evidence for the presence of very highly dispersed iron oxide particles. However no well-defined effect of the support pore structure on the iron particles dispersion could be established.

Practically similar ratios of HD/SPM haematite particles are found for 5FeCMK-1 and 5FeCMK-3 despite the variations in the impregnation medium (Table 3), while predominately presence of HD species ($G = 94\%$) is registered for the sample without regular pore structure (5FeR). At the same time at lower iron loading more highly dispersed haematite particles are observed for 0.5FeCMK-3A and 0.5FeR in comparison with 0.5FeCMK-1A. For the former materials MS spectra represent only quadruple doublets with core/shell ratio of about 2.7 and 1, respectively.

3.2. TPR experiments

The TPR patterns of 0.5FeCMK-1A and 0.5FeCMK-3A samples are compared in Fig. 6. The observed reduction peaks in the temperature interval of 450–720 K could be associated with Fe(III) → Fe(II) and Fe(II) → Fe(0) reduction transitions depending on the dispersion of the iron oxide particles and the support used. The data from the Moessbauer (Table 4) and XRD (not shown) measurements for the studied samples after the TPR experiments show predominantly the appearance of metal iron in all iron-modified samples. Higher reduction extent is found for both CMK-3A materials in comparison with their CMK-1A analogues (Table 4).

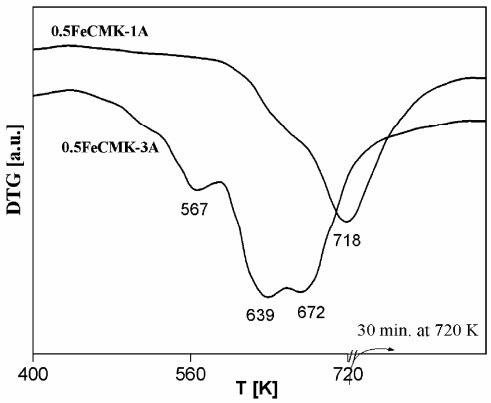

Fig. 6. DTG curves registered during TPR of 0.5FeCMK-1A and 0.5FeCMK-3A.

3.3. Catalytic study

In Fig. 7(A) are compared the temperature dependencies of methanol decomposition for various iron modified mesoporous carbons. In Fig. 7(B) are shown data on the products distribution (represented as methane selectivity) in this process under the same conditions. Depending on the iron loading, a significant catalytic effect is observed just above 670 and 625 K for the

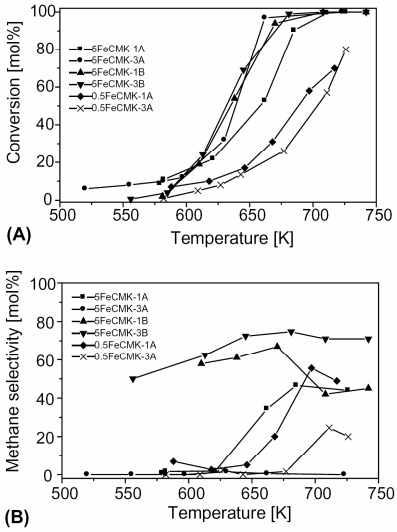

Fig. 7. Methanol conversion (A) and methane selectivity (B) vs. temperature on various iron modified mesoporous carbons.

Table 4
Moessbauer parameters of selected samples after TPR experiments

Sample	Components	IS [mm/s]	QS [mm/s]	H_{eff} [T]	FWHM [mm/s]	G [%]
0.5FeCMK-1A	Sxt-α-Fe	0.00	0.00	33.1	0.60	70
	Dbl-Fe_2O_3-SPM	0.36	0.75	–	0.70	30
0.5FeCMK-3A	Sxt-α-Fe	0.00	0.00	33.0	0.62	83
	Dbl 1-Fe_2O_3-SPM	0.36	0.96	–	0.50	10
	Dbl 2-Fe^{2+}	0.86	1.48	–	0.50	7
5FeCMK-1A	Sxt-α-Fe	0.00	0.00	33.0	0.29	79
	Dbl-Fe_2O_3-SPM	0.36	0.84	–	0.72	21
5FeCMK-3A	Sxt-α-Fe	0.00	0.00	33.0	0.36	95
	Dbl-Fe_2O_3-SPM	0.36	0.90	–	0.50	5

IS: isomer shift; QS: quadrupole splitting; H_{eff}: effective internal magnetic field; FWHM: full line width at half maximum; G: relative weight of the partial components in the spectra; Dbl: doublet; Sxt: sextet.

0.5FeCMK and 5FeCMK series of samples, respectively. The main registered carbon containing products in all cases are CO and methane. No essential differences in the total methanol conversion were found in each series of modified materials (Fig. 7(A)). In contrast, the pore structure of the support and the impregnation medium affect significantly the product distribution at each temperature (Fig. 7(B)). As a whole, a higher ability to methane formation is observed for the samples obtained by the ethanolic impregnation medium while for all aqueous obtained samples the methane selectivity remains below 40% in the whole investigated temperature interval. At the same time higher methane selectivity is found for CMK-1A based materials in comparison with CMK-3A ones. Practically no methane is registered for 5FeCMK-3A. These effects are also confirmed by the catalytic experiments under isothermal conditions (Fig. 8). Here, the methane selectivity decreases with time on stream (Fig. 8(B)) and this is more significant for 0.5FeCMK-3A compared to 0.5FeCMK-1A. A well-defined tendency for the catalytic activity decrease during the experiment is also found (Fig. 8(A)). Thus, some changes with the iron species due to the influence of the reaction medium could be proposed.

Moessbauer data of the samples after the catalytic test are shown in Fig. 9 and the corresponding parameters are presented in Table 5. The MS spectra represent the superposition of sextets and a doublet with different relative weight. The sextets belong to highly dispersed magnetite and as a whole, its relative weight is higher compared to the sextet parts in the spectra of the corresponding air-pretreated materials. The doublet part could be ascribed to the presence of unchanged SPM haematite particles. Only in the case of 5FeCMK-3A an additional component with parameters of α-Fe and $G = 27\%$ is also registered. Thus, two general effects with the state of the iron oxide species due to the reaction medium influence could be assumed. First, the reductive changes, predominantly to magnetite, occur with all the studied materials. They concern not only the HD haematite particles but a part of the SPM species as well. Next, a well-defined tendency for the iron particles agglomeration is also established. These effects are more significant for the CMK-3 based materials in comparison with the corresponding CMK-1 for both series (A and B) samples. Similar favourable effect of the CMK-3 structure on the haematite reduction transformations and agglomeration processes is also observed during the TPR experiments (Table 4). There, the relative part of the unchanged SPM haematite after the TPR treatment is less for both 0.5FeCMK-3 and 5FeCMK-3 in comparison with their corresponding CMK-1 analogues.

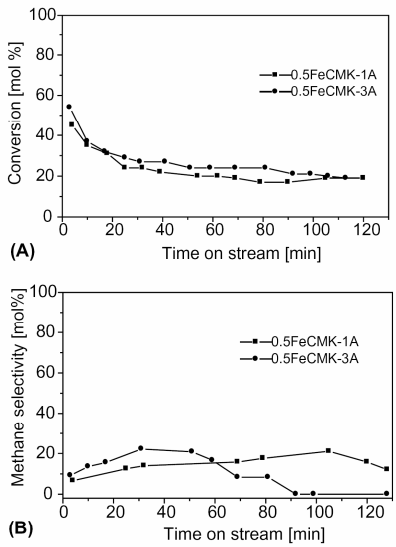

Fig. 8. Methanol conversion (A) and methane selectivity (B) vs. time on stream at 670 K on various iron modified mesoporous carbons.

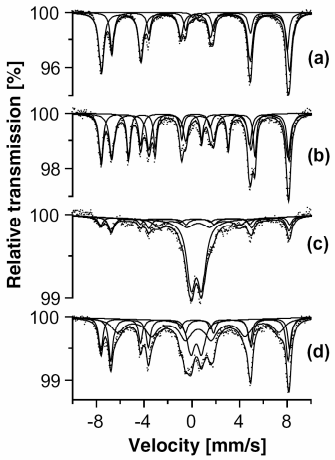

Fig. 9. Moessbauer spectra of 5FeCMK-1A (a), 5FeCMK-3A (b), 5FeCMK-1B (c) and 5FeCMK-3B (d) after catalytic test.

In conclusion, the combined physicochemical data (MS, XRD, TPR) show that the initial dispersion of the iron oxide particles supported on the mesoporous carbons strongly depends on the impregnation medium used during their preparation. More highly dispersed iron modified samples are obtained by using of ethanolic solution. However, the pore structure of the support seems to affect the iron state to a very low extent which is in contrast with the analogous mesoporous silica based materials [26]. Here, the relative part of HD and SPM iron oxide particles is almost similar for all ethanolic obtained samples. At the same time, several not very clear effects of the support structure are established for

Table 5
Moessbauer parameters of selected samples after the catalytic test

Sample	Components	IS [mm/s]	QS [mm/s]	H_{eff} [T]	FWHM [mm/s]	G [%]
5FeCMK-1A	Sxt 1-Fe^{3+}_{tetra} Fe_3O_4*	0.23	0.00	49.1	0.50	67
	Sxt 2 -$Fe^{2,5+}_{octa}$ Fe_3O_4*	0.66	0.00	45.7	0.39	31
	Dbl-Fe_2O_3-SPM	0.37	0.60	–	0.35	2
5FeCMK-3A	Sxt 1-Fe^{3+}_{tetra} Fe_3O_4*	0.28	0.00	49.1	0.41	30
	Sxt 2-$Fe^{2,5+}_{octa}$ Fe_3O_4*	0.68	0.00	45.9	0.52	43
	Sxt-α-Fe	0.00	0.00	33.0	0.33	27
5FeCMK-1B	Sxt 1-Fe^{3+}_{tetra} Fe_3O_4*	0.29	0.00	49.3	0.49	9
	Sxt 2-$Fe^{2,5+}_{octa}$ Fe_3O_4*	0.71	0.00	46.3	0.56	18
	Sxt 3-Fe_3O_4*	0.55	0.00	35.5	1.13	18
	Dbl-Fe_2O_3-SPM	0.39	0.89	–	0.86	55
5FeCMK-3B	Sxt 1-Fe^{3+}_{tetra} Fe_3O_4*	0.30	0.00	49.3	0.40	18
	Sxt 2-$Fe^{2,5+}_{octa}$ Fe_3O_4*	0.65	0.00	46.3	0.45	26
	Sxt 3-Fe_3O_4*	0.55	0.00	32.1	1.20	40
	Dbl-Fe_2O_3-SPM	0.37	0.90	–	0.72	16

IS: isomer shift; QS: quadrupole splitting; H_{eff}: effective internal magnetic field; FWHM: full line width at half maximum; G: relative weight of the partial components in the spectra; Dbl: doublet; Sxt: sextet.
* Sxt 1-Fe^{3+}_{tetra} and Sxt 2- $Fe^{2,5+}_{octa}$ belong to Fe_3O_4 large particles; Sxt 3 is a result of overlapping between Fe^{3+}_{tetra} and $Fe^{2,5+}_{octa}$ components of Fe_3O_4 small particles.

the aqueous prepared materials (Table 3). In this respect, the initial state of the iron oxide for both types of mesoporous carbon materials is predominantly determined by the hydrophobic graphitic surface nature of the support [3,4] and its different wetting with various impregnation media.

Well-defined effects of the iron oxide particles reduction transitions combined with their simultaneous agglomeration could be established due to the influence of the various reductive treatments (hydrogen or reaction medium). However, the observed phase transformations are more significant for the CMK-3 structure compared to the corresponding CMK-1 one (Tables 4 and 5), even in the case of the samples with very similar iron oxide initial state (Table 3). The presence of few functional groups on graphite-like carbon surface is reported for these materials [3,4] and as a result the existence of weak iron oxide-support interaction could be assumed. So, the reductive phase transformations seem to be determined predominantly by the iron species diffusion along the support pore channel system. In our opinion, the phase transformation of the hosted iron oxide species under the reductive conditions provides valuable information for the pore structure of these novel mesoporous carbons. In this aspect, a more accessible pore structure could be concluded to be present within CMK-3 in comparison with CMK-1 materials.

In our previous study the relation between the phase composition, the iron particles dispersion and the selectivity to methane in methanol decomposition on iron oxide modified mesoporous silicas was assumed [25]. Higher methane selectivity was observed for the samples with higher degree of magnetite formation during the catalytic test. At the same time, methanol was decomposed exclusively to CO when iron carbide forms under the same conditions. However no similar direct correlation for the carbon modified materials could be established. The relative part of magnetite in the samples after the catalytic test (700 K) changes as follows: 5FeCMK-1A > 5FeCMK-3B > 5FeCMK-3A > 5FeCMK-1B, (α-Fe is also found only for 5FeCMK-3A). At the same time the methane selectivity decreases in the order: 5FeCMK-3B > 5FeCMK-1B ≈ 5FeCMK-1A ≫ 5FeCMK-3A. We think, that the observed effect could be due to the complex factors, which determine the final state of iron under the reductive medium. Some possible changes in the reaction mechanism of the methanol decomposition [37–40] due to the weak iron/support interaction could not be excluded as well.

4. Conclusion

The dispersion of iron oxide nanoparticles supported on the mesoporous carbons could be controlled by the impregnation medium used during the impregnation process. However it is not strongly affected by the pore size of the support in comparison with the corresponding silica materials. The changes in the iron state under different reductive media are more significant for the CMK-3 structures compared to the CMK-1 ones due to the better structure connectivity of the former material. On the contrary to the analogous modified mesoporous silicas, here no clear relationship between the

initial state of the iron oxide particles, their phase transformations during the catalytic test and the observed methane selectivity in methanol decomposition is established.

Acknowledgement

Financial support by the Bulgarian National Scientific Fund (X-1208) and the Fonds der Chemischen Industrie is gratefully acknowledged.

References

[1] R. Ryoo, S.H. Joo, M. Kruk, M. Jaroniec, Adv. Mater. 13 (2001) 677.
[2] S.H. Joo, S.J. Choi, I. Oh, J. Kwak, Z. Liu, O. Terasaki, R. Ryoo, Nature 412 (2001) 169.
[3] H. Darmstadt, C. Roy, S. Kaliaguine, S.H. Joo, R. Ryoo, Micropor. Mesopor. Mater. 60 (2003) 139.
[4] H. Darmstadt, C. Roy, S. Kaliaguine, S.J. Choi, R. Ryoo, Carbon 40 (2002) 2673.
[5] R. Ryoo, S.H. Joo, S. Jun, J. Phys. Chem. B 103 (1999) 7743.
[6] M. Kruk, M. Jaroniec, J. Phys. Chem. B 104 (2000) 7960.
[7] S.H. Joo, S. Jun, R. Ryoo, Micropor. Mesopor. Mater. 44–45 (2001) 153.
[8] S. Jun, S.H. Joo, R. Ryoo, M. Kruk, M. Jaroniec, Z. Liu, T. Ohsuna, O. Terasaki, J. Am. Soc. 122 (2000) 10712.
[9] L.A. Solovyov, A.N. Shmakov, V.I. Zaikovskii, S.H. Joo, R. Ryoo, Carbon 40 (2002) 2477.
[10] K. Kaneda, T. Tsubakiyama, A. Carlsson, Y. Sakamoto, T. Ohsuna, O. Terasaki, S.H. Joo, R. Ryoo, J. Phys. Chem. B 106 (2002) 1256.
[11] L.A. Solovyov, V.I. Zaikovski, A.N. Shmakov, O.V. Belousov, R. Ryoo, J. Phys. Chem. B 106 (2002) 12198.
[12] S. Han, K.T. Lee, S.M. Oh, T. Hyeon, Carbon 41 (2003) 1049.
[13] K. Kuno, T. Naka, E. Negishi, H. Matsui, O. Terasaki, R. Ryoo, N. Toyota, Synth. Met. 135–136 (2003) 721.
[14] H. Juntgen, Fuel 65 (1986) 1436.
[15] C. Moreno-Castilla, M.A. Salas-Peregrin, F.J. Lopez-Garzon, Fuel 74 (1995) 835.
[16] J. Ma, Zh. Liu, Sh. Liu, Zh. Zhu, Appl. Catal. B: Environmental 45 (2003) 301.
[17] D. Santoro, V. de Jong, R. Louw, Chemosphere 50 (2003) 1255.
[18] C. Heisig, W. Zhang, S. Oyama, Appl. Catal. B: Environmental 14 (1997) 117.
[19] Yu.V. Maksimov, M.V. Tsodikov, M.A. Prerderi, Surf. Interf. Anal. 30 (2000) 74.
[20] Hui-Hsin Tseng, Ming-Yen Wey, Yu-Shen Liang, Ke-Hao Chen, Carbon 41 (2003) 1079.
[21] F. Rodriguez-Reinoso, Carbon 36 (1998) 159.
[22] Z. Liu, M. Kruk, M. Jaroniec, in: A. Sayari, M. Jaroniec (Eds.), Nanoporous Materials III, Studies in Surface Science and Catalysis, vol. 141, Elsevier, Amsterdam, 2002, p. 345.
[23] R. Ryoo, S.H. Joo, in: O. Terasaki (Ed.), Mesoporous Crystals and Related Nano-structured Materials, Studies in Surface Science and Catalysis, vol. 148, Elsevier, Amsterdam, 2004, p. 241.
[24] T. Tsoncheva, M. Dimitrov, D. Paneva, I. Mitov, R. Köhn, M. Fröba, C. Minchev, React. Kinet. Catal. Lett. 74 (2001) 385.
[25] R. Köhn, D. Paneva, M. Dimitrov, T. Tsoncheva, I. Mitov, C. Minchev, M. Fröba, Micropor. Mesopor. Mater. 63 (2003) 125.
[26] C. Minchev, H. Huwe, T. Tsoncheva, M. Dimitrov, D. Paneva, I. Mitov, M. Fröba, Proc. 14th Int. Zeol. Conf. (eds: E. van Steel et al.), Cape Town, South Africa, 2004, 841.
[27] H. Huwe, M. Fröba, Micropor. Mesopor. Mater. 60 (2003) 151.
[28] E.P. Barrett, L.G. Joyner, P.P. Halenda, J. Am. Chem. Soc. 73 (1951) 373.
[29] T. Ressler, J. Synchrotron Rad. 5 (1998) 118.
[30] J.J. Rehr, J. Mustre de Leon, S.I. Zabinsky, R.C. Albers, J. Am. Chem. Soc. 113 (1991) 5135.
[31] A.M. Van der Kraan, Hyperfine Interact. 40 (1988) 211.
[32] K.S.W. Sing, D.H. Everett, R.A.W. Haul, L. Mouscou, R.A. Pierotti, J. Rouquerol, T. Siemieniewska, Pure Appl. Chem. (1993) 1257.
[33] M. Fröba, R. Köhn, G. Bouffaud, O. Richard, G. van Tendeloo, Chem. Mater. 11 (1999) 2858.
[34] H. Huwe, M. Fröba, in preparation.
[35] A. Manceau, V.A. Drits, Clay Miner. 28 (1993) 165.
[36] R.L. Blake, R.E. Hessevick, T. Zoltai, L.W. Finger, Am. Mineral. 51 (1966) 123.
[37] R.J. Levis, J. Zhicheng, N. Winograd, J. Am. Chem. Sci. 110 (1988) 4431.
[38] R.J. Levis, J. Zhicheng, N. Winograd, J. Am. Chem. Sci. 111 (1989) 4605.
[39] M. Mavrikakis, M.A. Barteau, J. Mol. Catal. A: Chemical 131 (1998) 135.
[40] N. Takezawa, N. Iwasa, Catal. Today 36 (1997) 45.

research papers

Journal of
Synchrotron Radiation
ISSN 0909-0495

Received 21 November 2005
Accepted 10 March 2006

Temperature-resolved *in situ* X-ray absorption spectroscopic study on the reduction of nanostructured Fe_2O_3 within the pore system of mesoporous carbon CMK-1

Holger Huwe and Michael Fröba*

Institute of Inorganic and Analytical Chemistry, Justus Liebig University Giessen, Heinrich-Buff-Ring 58, 35392 Giessen, Germany. E-mail: michael.froeba@anorg.chemie.uni-giessen.de

Results of *in situ* X-ray absorption spectroscopy experiments on the reduction of thin-layered nanostructured X-ray amorphous iron(III) oxides inside the pore system of mesoporous carbon CMK-1 are presented. These *in situ* measurements were carried out using 4% hydrogen in nitrogen as reduction gas over a 300–1000 K temperature range. The thermochemical behaviour of the nanostructured materials was compared with that of the bulk phases. The spectra series examined by factor analysis gave a good insight into the reduction products of iron oxide nanoparticles occurring in mesoporous carbon CMK-1.

Keywords: XAFS; *in situ*; nanostructured iron oxide; mesoporous carbon; reduction; host structure.

1. Introduction

The reduction behaviour of 3*d* metal oxides has been investigated for more than a century, particularly for the system $Fe_2O_3 \rightarrow Fe_3O_4 \rightarrow Fe_{1-x}O \rightarrow Fe^0$ for which multiple experimental and theoretical studies have been carried out. In fact, the members of this group act in a sense often as model compounds for the varieties of transition metal oxides. This system was chosen owing to its application in *e.g.* catalysis or in potential hydrogen storage. Many experiments have been performed in order to learn more about the properties of the iron oxides or to study their redox behaviour, resulting in numerous papers and books (Bajt *et al.*, 1994; Becker *et al.*, 1995; Cornell & Schwertmann, 2003; Darken & Gurry, 1946; de Masi *et al.*, 2002; Dünwald & Wagner, 1931; Fjellvåg *et al.*, 2003; Fröba *et al.*, 1999; Köhn & Fröba, 2003; Köhn *et al.*, 2003; Rao & Moinpour, 1983).

New access to nanosized particles is provided by their synthesis within confined spaces of defined solid host materials. Generally, these spaces are ordered pores which serve as size-limiting matrices for the nanostructured guest species. Very often these host/guest compounds exhibit different physical and chemical properties in comparison with the respective bulk materials. For example the system $Cd_{1-x}Mn_xS$@MCM-48 silica shows strong size dependencies on the magnetic and optical properties of the guest compound (Brieler *et al.*, 2005; Klar *et al.*, 2004); the systems Fe_2O_3@SBA-15 silica and Fe_2O_3@CMK-3 carbon exhibit catalytic activities different from that of bulk haematite (Minchev *et al.*, 2005; Tsoncheva *et al.*, 2004). Depending on the reaction conditions it is also possible to form different nanostructured phases, *e.g.* magnetite owing to the intra-pore reduction of haematite, an example we will examine in this study. For a deeper insight into the redox behaviour of metal oxides, *in situ* X-ray absorption spectroscopy (XAS) is a very good probe for investigating these properties.

The present work undertakes the first study on the reduction behaviour of nanosized iron(III) oxides formed in mesoporous carbon atoms in comparison with the respective bulk materials. Apart from that it shows the potential of *in situ* XAS studies for gaining knowledge (in a simple manner) on redox processes.

2. Synthesis and experimental

Nanostructured X-ray amorphous iron(III) oxides were synthesized inside the pore system of mesoporous carbon CMK-1 (pore diameter $\simeq$ 3 nm), first reported by Huwe & Fröba (2003). The almost exclusive intra-pore formation of these nanosized particles and the preservation of the host structure during the synthesis procedure was proved by powder X-ray diffraction, nitrogen physisorption, transmission electron microscopy, Raman and X-ray absorption spectroscopy.

The *in situ* reductions were carried out in a specially designed and constructed cell (Huwe & Fröba, 2004) at the beamline EXAFS II (E4) at the storage ring Doris III (HASYLAB @ DESY, Hamburg, Germany). All spectra were recorded in fluorescence mode using a single-crystal Ge detector.

For the measurements the nanostructured host/guest compound as well as bulk haematite were pressed into boron

nitride pellets. As reduction gas, 4% hydrogen in nitrogen was used with a flow rate of 25 cm^3 min^{-1}. The spectra series were taken in the temperature range 300–1000 K (heating rate 5 K min^{-1}) with a spectrum recorded every 15 K under continuous heating.

The respective series of XANES spectra were analyzed using the program *WinXAS* (Ressler, 1998). After common data reduction procedures a principal component analysis (PCA, factor analysis) (Malinowaski & Howery, 1980; Ressler *et al.*, 2000) was carried out with respect to the corresponding reference spectra of the bulk materials. For a discussion of the results one has to take into account that the detection limit of the PCA is about 4–5%. The required reference spectra were recorded from commercially available oxides and metals in nitrogen atmosphere at the temperatures where they occur in the products during the reduction process.

3. Results and discussion

A series of energy-calibrated, normalized and background-corrected spectra of the reduction of Fe_2O_3@CMK-1 are shown in Fig. 1. Clearly visible is the decrease in the white-line intensity and changes in the EXAFS oscillations during the reduction process. In the XANES a change in the pre-edge region accompanied by an 8 eV shift of the absorption edge to smaller energies for the transformation $Fe_2O_3 \rightarrow Fe^0$ is observed.

The occurrence of the different phases of the host/guest system (extracted from the XANES) is shown in Fig. 2(*a*). The reduction process starts at about 580 K and ends at about 890 K. The first reduction product is magnetite. The major part of Fe_3O_4 is reached at 683 K (89%). This followed a decrease owing to the formation of $Fe_{1-x}O$, a non-stoichiometric wüstite phase. At 720 K the partition of Fe_3O_4 is equal to those of $Fe_{1-x}O$ (~48% each). Fe_3O_4 occurs up to ~800 K. The formation of $Fe_{1-x}O$ starts at about 650 K, has a maximum at 760 K (91%) and decreases due to the reduction to Fe^0.

Fig. 2(*b*) exhibits the corresponding results for the bulk haematite. At first glance the phases formed are the same, but the redox processes take place over a different temperature range. A more detailed presentation is shown in Figs. 3(*a*) and 3(*b*). Here the occurrence (as a function of the reduction temperature) of the respective phases in the case of the host/guest compound and the bulk material is compared. The reduction process starts at 650 K for the bulk material and ends at about 800 K. In contrast, the nanostructured host/guest system already begins to react at 580 K, an effect probably caused by the very small particle size (~3 nm) which leads to a higher thermochemical reactivity. In addition, the temperature interval in which the phase transformations occur is two times larger for Fe_2O_3@CMK-1 ($\Delta T \simeq 310$ K), an effect which could be due to the intra-pore diffusion limitations for the gaseous species. While for the host/guest compound the reduction to Fe_3O_4 has already reached its maximum (at 683 K), that of bulk haematite has just started. The formation of the bulk $Fe_{1-x}O$ phase has its maximum almost at the same temperature as $Fe_{1-x}O$@CMK-1, but the reduction to Fe^0 is much faster. Another difference between the host/guest compound and the bulk material is the maximum concentration of the two intermediate phases Fe_3O_4 and $Fe_{1-x}O$. Owing to the broader temperature range (caused by slower kinetics) the overlap of the different regimes of occurrence is reduced in the case of the host/guest compounds, which results in

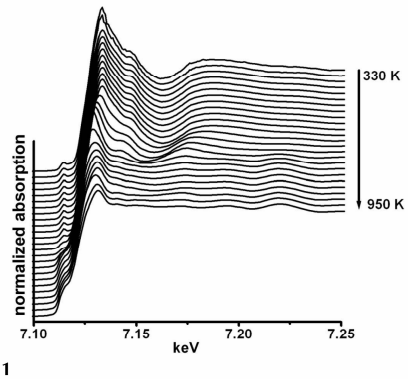

Figure 1
Temperature-dependent *in situ* XAS measurements at the Fe *K*-edge of Fe_2O_3@CMK-1 during reduction with hydrogen in nitrogen.

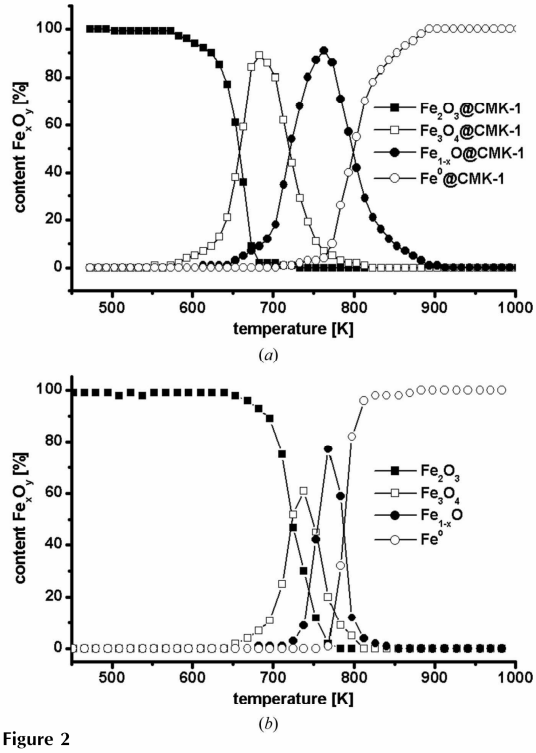

Figure 2
Occurrence of the respective iron oxide phases during the reduction process of (*a*) Fe_2O_3@CMK-1 and (*b*) bulk haematite.

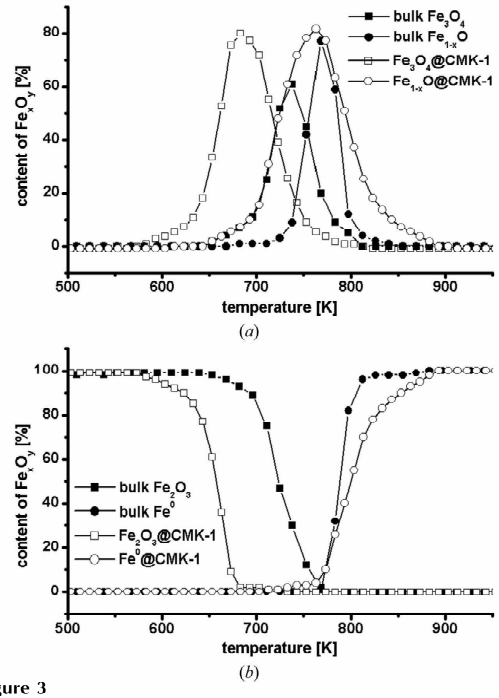

Figure 3
Comparison between the respective iron oxide phases occurring during the reduction process of Fe_2O_3@CMK-1 and bulk haematite: (*a*) bulk Fe_3O_4 and bulk $Fe_{1-x}O$ *versus* Fe_3O_4@CMK-1 and $Fe_{1-x}O$@CMK-1; (*b*) bulk Fe_2O_3 and bulk Fe^0 *versus* Fe_2O_3@CMK-1 and Fe^0@CMK-3.

contents of above 90% for the single phases. In contrast, the bulk material always exhibits mixtures of at least two (sometimes even three) phases which of course decreases the content of the respective majority phase. In general, one can say that the kinetics of the reduction steps $Fe_2O_3 \rightarrow Fe_3O_4 \rightarrow Fe_{1-x}O \rightarrow Fe^0$ are affected by the spatial and chemical environment. In the case of the host/guest compound the reduction starts at lower temperatures which can be attributed to the much smaller particle size. Nevertheless, there might also be some influence from the carbon host structure which could promote the reduction of the haematite. In conclusion, it seems that in the case of the host/guest system the reduction reactions are not that fast compared with the bulk material, which is probably caused by diffusion limitations. Nevertheless, this allows a much better separation of the respective single phases in comparison with the bulk material, an effect which might be useful for further studies.

4. Conclusion

This study shows the first results on the reduction of iron oxide nanoparticles within a mesoporous carbon CMK-1 host structure. The thermochemical behaviour was monitored by temperature-dependent *in situ* X-ray absorption spectroscopic measurements. While the reduction of the nanoparticles starts at lower temperatures, the velocity of the following transformations are slowed down in comparison with the bulk material which allows a much better separation of single phases. In summary, one can say that the kinetics of the reduction steps $Fe_2O_3 \rightarrow Fe_3O_4 \rightarrow Fe_{1-x}O \rightarrow Fe^0$ are mainly affected by the particle size as well as the spatial and chemical environment.

The authors would like to thank HASYLAB@DESY for allocating beam time and financial support. Further financial support by the Justus Liebig University Giessen and the Fonds der Chemischen Industrie is gratefully acknowledged.

References

Bajt, S., Sutton, S. R. & Delaney, J. S. (1994). *Cosmochim. Acta*, **58**, 5209–5214.
Becker, K. D., Niemeier, D., Wissmann, S., Oversluizen, M., Couves, J. W. & Chadwick, A. V. (1995). *Nucl. Instrum. Methods*, B**97**, 111–114.
Brieler, F. J., Grundmann, P., Fröba, M., Chen, L., Klar, P. J., Heimbrodt, W., Krug von Nidda, H.-A., Kurz, Th. & Loidl, A. (2005). *Chem. Mater.* **17**, 795–803.
Cornell, R. M. & Schwertmann, U. (2003). *The Iron Oxides*. Weinheim: Wiley-VCH.
Darken, L. S. & Gurry, R. W. (1946). *J. Am. Chem. Soc.* **68**, 798–819.
Dünwald, H. & Wagner, C. (1931). *Z. Anorg. Allg. Chem.* **199**, 321–819.
Fjellvåg, H., Hauback, B. C., Vogt, T. & Stølen, S. (2002). *Am. Mineral.* **87**, 347–349.
Fröba, M., Köhn, R., Bouffaud, G., Richard, O. & van Tendeloo, G. (1999). *Chem. Mater.* **11**, 2858–2865.
Huwe, H. & Fröba, M. (2003). *Micropor. Mesopor. Mater.* **60**, 151–158.
Huwe, H. & Fröba, M. (2004). *J. Synchrotron Rad.* **11**, 363–365.
Klar, P. J., Chen, L., Heimbrodt, W., Brieler, F. J., Fröba, M., Kurz, T., Krug von Nidda, H.-A. & Loidl, A. (2004). *Advances in Solid State Physics*, Vol. 44, edited by B. Kramer, pp. 491–502. Berlin/Heidelberg: Springer-Verlag.
Köhn, R. & Fröba, M. (2003). *Z. Anorg. Allg. Chem.* **629**, 1673–1682.
Köhn, R., Paneva, D., Dimitrov, M., Tsoncheva, T., Mitov, I., Minchev, C. & Fröba, M. (2003). *Micropor. Mesopor. Mater.* **63**, 125–137.
Malinowaski, E. R. & Howery, D. G. (1980). *Factor Analysis in Chemistry*. New York: Wiley.
Masi, R. de, Reinicke, D., Muller, F., Steiner, P. & Hufner, S. (2002). *Surf. Sci.* **516**, L515–L521.
Minchev, C., Huwe, H., Tsoncheva, T., Paneva, D., Dimitrov, M., Mitov, I. & Fröba, M. (2005). *Micropor. Mesopor. Mater.* **81**, 331–341.
Rao, Y. K. & Moinpour, M. (1983). *Metall. Trans. B*, **14**, 711–723.
Ressler, T. (1998). *J. Synchrotron Rad.* **5**, 118–122.
Ressler, T., Wong, J., Roos, J. & Smith, I. L. (2000). *Environ. Sci. Technol.* **34**, 950.
Tsoncheva, T., Paneva, D., Mitov, I., Huwe, H., Fröba, M., Dimitrov, M. & Minchev, C. (2004). *React. Kinet. Catal. Lett.* **83**, 299–305.

Anal Bioanal Chem (2006) 384: 817–826
DOI 10.1007/s00216-005-0234-z

ORIGINAL PAPER

Holger Huwe · Michael Fröba

Multiple-scattering extended X-ray absorption fine structure analysis of nanostructured iron(III) oxide in the pore system of mesoporous carbon CMK-1

Received: 19 August 2005 / Revised: 3 November 2005 / Accepted: 3 November 2005 / Published online: 12 January 2006

Abstract This work is devoted to the EXAFS analysis of nanostructured iron(III) oxide synthesized inside the pore system of mesoporous carbon CMK-1. A detailed study of the recording, preparation and evaluation of data recorded in fluorescence mode at the iron K-edge with and without multiple scattering is shown. The results obtained show that the local structure of Fe^{3+} inside nanostructured iron (III) oxide is different to that of the bulk material. Due to the small particle size, data analysis is much more difficult and data preparation more complex. Incorporating multiple scattering paths in the Fourier transforms and back-transforms during data evaluation gives structural insights that cannot be obtained using other spectroscopic methods, and this technique was used to draw conclusions about the first four coordination spheres of the nanostructured iron(III) oxide.

Keywords Fe-K XAFS · Nanostructured host/guest compounds · Mesoporous carbon · Nanostructured iron(III) oxide

Introduction

In recent years a variety of nanostructured host/guest compounds have been studied by several research groups. The mesoporous silica phases MCM-48 and SBA-15 silica are in the focus of much of this research. Numerous reports have been published on the incorporation of metal atoms into mesoporous MCM-48 (metal atoms such as Ag [1], Co [2, 3], Cu [3, 4], Fe [3–8], La [9], Mn [10], Ni [3], Pb [5], Pd [11],Ti [12–15], V [16–18], Zn [5]) and into mesoporous SBA-15 (metal atoms such as Ag [19], Au [19], Cd [20], Fe [21] Ge [22], Mn [20, 23], Pd [24], Pt [19], Ti [25]). These nanostructured host/guest compounds are of interest for a wide number of applications in materials science, such as in catalysis [3–5, 9, 16, 26, 27], magnetic and diluted magnetic semiconductors [20, 23], and magnetic studies [8].

A new family of host structures, mesoporous carbons, was introduced to host/guest chemistry in 2001 [28–34]. The advantages of mesoporous carbons over mesoporous silica phases include their stability in strong acids and bases. They are also stable under high pressure and have a reducible matrix. Joo et al. [35] first reported on platinum nanoparticle incorporation into the mesoporous carbon CMK-3. The electrocatalytic activity of his host/guest compound for oxygen reduction was tested, which may be relevant to fuel-cell devices. In 2003, the authors reported on the incorporation of iron(III) oxide inside the pore system of mesoporous carbon CMK-1 [36]. The focus then turned to the intrapore synthesis of iron(III) oxide. EXAFS (extended X-ray absorption fine structure spectroscopy) experiments were carried out to obtain information on the local structure of the iron(III) oxide. This new nanostructured host/guest compound Fe_2O_3@CMK-1 was found to be highly desirable for catalysis (of methanol decomposition for instance [37, 38]) and advanced magnetic material preparation after intrapore reduction of the iron(III) oxide.

Gathering information on the local structure and oxidation state of the guest species is a very important activity in host/guest chemistry. EXAFS is often used to characterize nanostructured metal oxides in host materials [3, 6, 38–42]. These EXAFS evaluations are mostly restricted to the first three metal–metal coordination shells. In this case, the radial distribution function (and therefore the potential structural insights that this could provide) is not fitted, and results are not refined by incorporating multiple scattering paths.

The crystal structure of alpha iron(III) oxide was first solved by Pauling and Hendricks in 1925 [44]; it was then

H. Huwe · M. Fröba (✉)
Institute of Inorganic and Analytical Chemistry,
Justus Liebig University Giessen,
Heinrich-Buff-Ring 58,
35392 Giessen, Germany
e-mail: michael.froeba@anorg.chemie.uni-giessen.de
Tel.: +49-641-9934100
Fax: +49-641-9934109

refined in 1966 by Blake [45], the results of which are still valid today. Submicron iron oxide particles can be synthesized with average crystallite dimensions of up to 5 nm using wet chemical techniques with stabilization procedures [43–47]. Nevertheless, these procedures reveal a broad size distribution, with only a few nanosized particles. In contrast, synthesis within mesoporous host structures leads to particles of a defined size (two dimensions are restricted by the pore diameter and the third dimension by the pore length). The absence of chemical boundaries between the host and the guest compound, as demonstrated in leach experiments, is another important point in relation to nanocomposites [48].

With the introduction of synchrotron radiation as an X-ray absorption spectroscopy source in the 1970s, the structures of haematite and other iron oxides were investigated once more. Several reviews of XAFS spectroscopy have been published [43, 49–66]. Very recently, a comprehensive review was published by Waychunas et al., who carried out XAFS investigations of nanoparticulate iron oxide minerals in soils and sediments [67].

However, XAFS investigations of nanostructured iron oxides in mesoporous materials have only been performed since 1999. In spite of the great potential of XAFS in this area, only a few papers have investigated it [3, 6, 36]. In these papers, the EXAFS analyses are mostly restricted to three coordination spheres about the iron atom, neglecting multiple scattering contributions to the experimental data.

Experimental

Synthesis and characterization

The synthesis of the host structure CMK-1 was carried out according to the procedures described in the literature [36]. Three impregnation, drying and calcination cycles were applied to form iron(III) oxide inside the host structure.

In a typical procedure, 1 g of dried CMK-1 was stirred for 30 minutes in 50 mL of an ethanolic solution of iron nitrate (4.6 mol/L) at room temperature. The carbon iron nitrate composite was separated from the solution by centrifugation and dried under vacuum at room temperature. Afterwards the host/guest compound was calcined at 573 K for five hours, leading to the transformation of the iron nitrate into iron(III) oxide. By performing this impregnation cycle three times, an iron content of ~65 weight percent [wt%] was obtained. Fe_2O_3@CMK-1 is also known as a host/guest compound. Bulk haematite, which served as the reference compound in this work, was synthesized in the same way as described above.

The host/guest compound was characterized using powder X-ray diffraction, infrared spectroscopy, nitrogen physisorption, transmission electron microscopy and Raman spectroscopy, in order to demonstrate the preservation of the host structure during the impregnation/calcination process and the formation of the iron(III) oxide almost exclusively inside the pore system of the mesoporous carbon. Further information on the characterization is given in [36].

XAFS: sample preparation

The bulk haematite and the host/guest compound were measured as freshly prepared polyethylene pellets (1 cm in diameter). After drying in vacuum at room temperature, 20–35 mg of the host/guest compound or 5–7 mg of the bulk haematite respectively were crushed and mixed together with 45 mg dried polyethylene to give a homogeneous mixture. The transition metal content of this mixture lead to an absorption jump of $\Delta\mu_d$=0.5–1.0.

Recording the spectra

Fe K-edge spectra were recorded at the EXAFSII beam line at HASYLAB@DESY in Hamburg, Germany. The positron storage ring DORIS III gave a positron energy of 4.45 GeV, an initial beam current of 140 mA and injection at 85 mA in five-bunch mode. The runtime was approximately eight hours.Nonfocused synchrotron radiation was obtained for the EXAFS experiments by bending magnets. The resolution of the Fe K-edge (7112 eV) was between 0.8 and 1.0 eV at the beam line used.

The experimental set-up is shown in Fig. 1. The desired wavelength of the white beam is filtered using a Si(111) double crystal (monochromator). The beam size at the host/guest compound was about 0.8×6 mm. The host/guest compounds were cooled to nearly liquid nitrogen temperature (85 K) using a liquid nitrogen cryostat. The fluorescence signal was detected with a five-element germanium fluorescence detector. The intensity of the beam was controlled using digital monochromator stabilization (DMOSTAB), which was set to 50% on the left side of the rocking curve in order to avoid higher harmonic oscillations.

The EXAFS spectra were collected for 6950–8200 eV (ΔE=1250 eV). Due to the small amount of iron(III) oxide inside the host, the spectra were recorded in fluorescence mode. All spectra were recorded up to four times to improve the signal-to-noise ratio after summation.

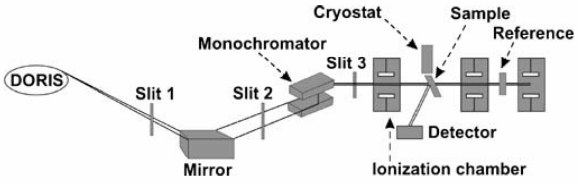

Fig. 1 Schematic representation of the set-up at the EXAFSII beamline at HASYLAB

Data reduction

The program WinXAS version 2.3 [68] was used for data reduction.

The formulae, theorems, menu items and so on used are described in detail in the program manual and in references therein [69]. Spectral preparation and reduction consists of

- Summation of four spectra
- Energy calibration
- Background correction
- Setting E_0
- Determination of the atomic absorption (μ_0–fit)
- Fourier transformation and back transformation

Data reduction was performed in order to convert the recorded data into a fittable form. The fitting and refinement were carried out on the Fourier transforms and their back-transforms.

To improve the signal-to-noise ratio, four energy-calibrated and normalized fluorescence spectra were averaged. Energy calibration was performed using a reference spectrum which was recorded in transmission mode for every host/guest compound spectrum. Background correction was achieved by using one polynomial at the pre-edge region and another at the post-edge region. The maximum order of each polynomials was restricted to two in order to keep the atomic adsorption function μ_0 oscillation-resistant. An advanced spline fit was carried out to determine the atomic absorption μ_0 in the EXAFS region. In contrast to the cubic spline fit, the range of k was divided up here into to four sections with its own number of knots. This spline function gives better results for the host/guest system. The extraction of the atomic absorption function is the trickiest part and must be carried out very carefully to prevent data manipulation. In the advanced spline fit, the number of knots for the spline and the selected spectral range were varied; the weighting of k was always three. The range setting is sensitive to the number of independent parameters N_{ind} (Eq. 1). In general the range was defined to be from the first minimum after the white line of the spectrum up to k=18 Å^{-1}, depending on the quality of the recorded spectra. This was used to obtain maximum information while minimizing the number of independent parameters. The EXAFS oscillations were separated using a Fourier transform with a Bessel window with a beta of 4.

$$N_{ind} = \frac{2\Delta R \Delta k}{\pi} + 2 \tag{1}$$

Here N_{ind} is the number of independent parameters, ΔR is the fit range, and Δk is the range in k-space.

The Fourier transformation gives a radial distribution function (RDF). The positions r of the emerged peak maxima are phase-shifted distances between the central and backscattering atom. Figure 2 shows the non-phase corrected RDF of bulk haematite.

The first peak corresponds to the iron–oxygen distance in haematite. The second peak corresponds to iron–iron distances between face- and edge-shared octahedra. Peak three corresponds mainly to the iron–iron distance between corner-shared octahedra. Peak four is determined through multiple scattering effects and cannot be assigned to coordination spheres.

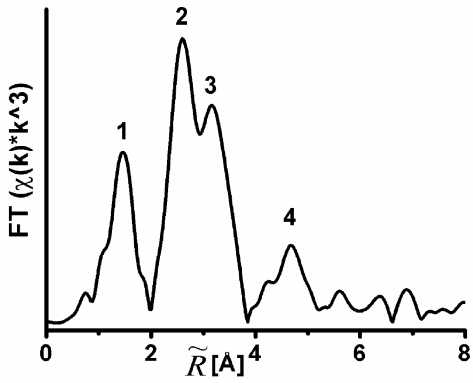

Fig. 2 Radial distribution function (RDF, not phase-corrected) of the $\Pi(k).k^3$ function from the EXAFS spectrum of bulk haematite

Back transformation was performed on the RDF with a k-weight of 3 in the range where the iron–iron shells appear; typically $\tilde{R} = 2.2 - 4.2\mathring{A}$. The distances obtained correspond to the distances between iron and its neighbouring atoms in the respective spheres in haematite.

Data analysis

Fit simulation and refinement was carried out on the Fourier transforms as well as on the back-transforms using the ab initio theoretical XAS code FEFF8.2 [70].

XAS simulation and refinement using the ab initio theoretical XAS code FEFF8.2 was carried out on the Fourier transforms and on the back-transforms in the same way. First the FEFF input file was generated.The input file for haematite (available on the ATOMS website [71]) was converted to an FEFF input file using the program ATOMS [72]. Single and multiple scattering paths were obtained by executing FEFF with the respective FEFF input file [68, 70].

To extract structural information the fast curve wave theory [73] was used. It can be described with Eq. (2). The parameters F_j, σ' and λ were calculated using the von Barth potential for ground states, the Hedin-Lundquist exchange potential for excited states [74] and the relaxed approximation for the core-hole [75].

$$\chi(k) = \sum_j \frac{N_j S_0^2 F_j(k)}{kR_1^2} * e^{(-2k^2\sigma_j^2)} * e^{\left(\frac{-2R_j}{\lambda}\right)} * e^{\left(2/3\sigma_j'' k^4\right)} * \sin\left[2kR_j + \delta_j(k) - 4/3\sigma_j' k^3\right] \tag{2}$$

where $F(k)$ is the backscattering amplitude, $\delta(k)$ is the phase, λ is the photoelectron mean free path, j is the j-th scattering path, N is the coordination number, R is the distance, σ^2 is the disorder parameter, S_0^2 is the amplitude reduction factor, σ' is the third cumulant, and σ'' is the fourth cumulant.

All of the single scattering paths and the multiple scattering paths with an amplitude intensity larger than 2% in comparison to the first shell up to the fifth angular path were used for bulk haematite. Normally this set of reduced FEFF input files is used for XAFS simulation and refinement. However, the problem with this is that these paths calculated from single-crystal data are often too large for nanosized clusters. Therefore, these FEFF input files were refined in two steps; see Fig. 3. Firstly, a FEFF simulation was carried out with the reduced FEFF input file. During this step, the current relative weights and angles for each path were calculated anew with respect to the adapted structure of bulk haematite. Secondly, these new FEFF files were filtered (relative weight >3%) and stored as optimized FEFF files.

The optimized FEFF file contains only significant FEFF paths and amplitudes for the host/guest compound and so is more suitable for the refinement procedures.

The distance R is chosen based on the appearance of the shells in the respective XAS function. To keep the number of free running parameters N_{frp} significantly smaller than the number of independent parameters N_{idp} during the refinements, some restrictions were placed on the variables:

- The amplitude reduction factor for bulk haematite was constrained to 0.5–0.95 and the result was used as a constant in the host/guest compound fit.
- The Debye-Waller factors were constrained to 0.001–0.01 Å^2
- The Debye-Waller factors for the multiple scattering paths were calculated from those of the single scattering paths
- The coordination numbers and distances of the multiple scattering paths were correlated with the respective single scattering paths
- The energy shift was set to be the same for each element in the system

The simulation was carried out with these restrictions and was it refined up to an acceptable level. These parameters were then used as the initial parameters in the next fit refinement procedure. The most restrictive refinement was done first of all, and then more and more parameters were set free. The refinement was continued as long as the following requirements were achieved:

- Low deviation parameter χ^2
- Residual is smaller than 10, calculated via Eq. 3
- Correlations in the correlation matrix are between 0.96 and 1
- F-Test result is >0.6 after refinement with more free variable running parameters, proving that a global minimum has been reached.

$$R[\%] = \frac{\sum_{i=1}^{N} \left| y_{\mathrm{exp}}(i) - y_{theo}(i) \right|}{\sum_{i=1}^{N} \left| y_{\mathrm{exp}}(i) \right|} \times 100, \qquad (3)$$

Here N is the number of data points, y_{exp} are the experimental data points, and y_{theo} are the theoretical data points.

In many cases the errors were estimated at 1% for the distance, 5% for the Debye-Waller factor, 10% for the inner potential correction and 5% for the coordination number [76]. Due to the (nano)sizes of the particles and the consequent distortion in the crystal structure of the iron(III) oxide, these error limits need more consideration.

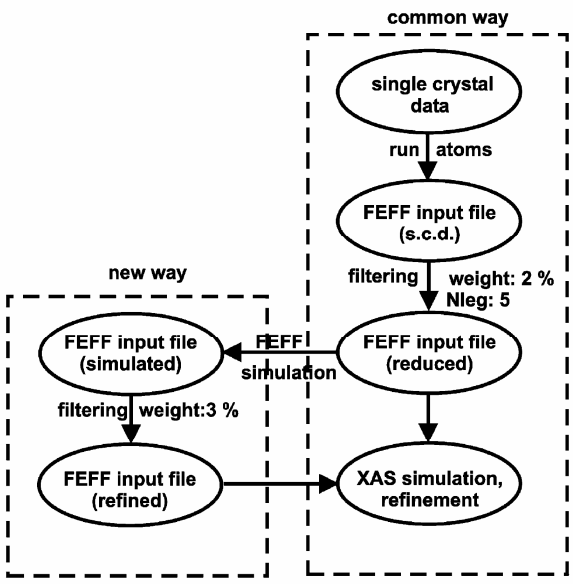

Fig. 3 Usual and new refinement procedures for the FEFF file

Results and discussion

XAFS measurements were carried out in fluorescence mode in order to investigate the nature of the iron coordination within the iron oxide nanoparticle.

Due to the conditions used during the synthesis of the host/guest compound, it can be assumed that iron(III) oxide with a haematite-like structure is formed inside the pore system of the mesoporous carbon.

Bulk haematite is isostructural with corundum. It can be thought of as consisting of hcp arrays of oxygen ions where two thirds of the octahedral sites filled with iron(III) ions [77]. The arrangement of the iron ions leads to FeO_6 octahedra. As shown in Fig. 4, three different kinds of

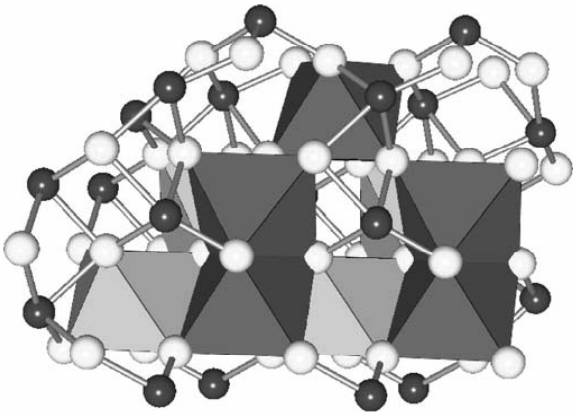

Fig. 4 Polyhedral model of haematite. *Dark*: iron, *light*: oxygen atoms

octahedra linkages exist. Iron–iron distances of about 2.90 Å are observed between face-shared and distances of about 2.97 Å between edge-shared octahedra. The two other iron–iron distances (3.36 and 3.71 Å) are due to a corner-shared linkages of the octahedra [44, 53].

The Fourier transforms of bulk haematite and the host/guest compound are shown in Fig. 5. The iron–oxygen shells of the host/guest compound are mostly unchanged from bulk haematite. The radial distribution function of bulk haematite shows peaks of up to 7.5 Å, while peaks of up to 4 Å are distinguishable for the host/guest compound. The strong reduction in backscattering amplitude intensity of the iron–iron shells of the host/guest compound is due to the small particle size (and therefore the limited vertical extension) and structural disorder; these effects are well known for systems lacking long-range order. Therefore either an increase in the Debye-Waller factors and/or a reduction in the coordination numbers of outer shells must be assumed. It should be noted that the Debye-Waller factors and the coordination numbers are strongly correlated and should not be neglected in a multiple shell fit. A significant reduction in the coordination

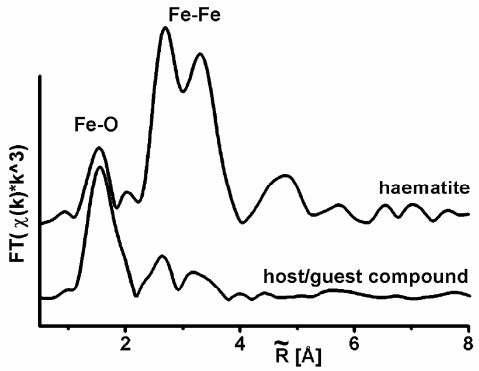

Fig. 5 Radial distribution functions (RDF, not phase-corrected) of the Fe K-edge oscillations $\chi(k)$. k^3 of the host/guest compound Fe_2O_3@CMK-1 and of bulk haematite. The RDF of bulk haematite has been divided by two

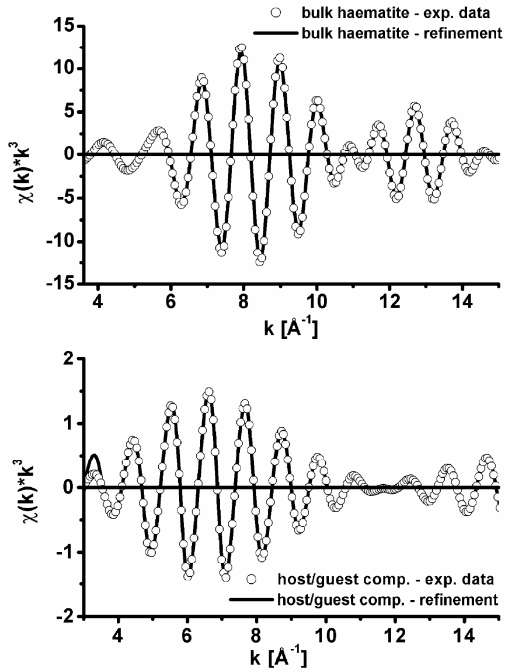

Fig. 6 Back-transforms of the Fe–Fe coordination shells and the results from least squares refinements of bulk haematite and the host/guest compound

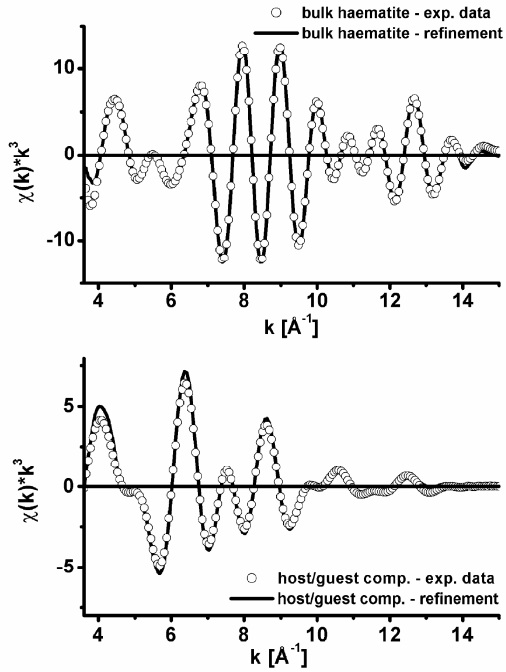

Fig. 7 Back-transforms of the Fe–O and Fe–Fe coordination shells and the results from least squares refinements of bulk haematite and the host/guest compound

Table 1 Refined structural parameters of the iron–iron shells of the host/guest compound and bulk haematite as well as corresponding results extracted from single-crystal data for haematite, obtained with.without refining the single scattering paths for the iron–oxygen coordination shells

Refinement	Shell	Host/guest compound		Bulk haematite		Haematite single-crystal [45]
		With Fe–O	Without Fe–O	With Fe–O	Without Fe–O	
N	Fe–O	2.90	-	3.01	-	3
R [Å]		1.91	-	1.95	-	1.94
$\Delta\sigma^2$ [Å^2]		0.007	-	0.003	-	-
N	Fe–O	2.85	-	3.01	-	3
R [Å]		2.13	-	2.10	-	2.11
$\Delta\sigma^2$ [Å^2]		0.008	-	0.004	-	-
N	Fe–Fe	0.74	0.73	0.90	0.91	1
R [Å]		3.00	3.01	2.88	2.88	2.89
$\Delta\sigma^2$ [Å^2]		0.003	0.004	0.004	0.003	-
N	Fe–Fe	1.35	1.31	2.98	3	3
R [Å]		3.04	3.03	2.94	2.95	2.96
$\Delta\sigma^2$ [Å^2]		0.004	0.005	0.003	0.004	-
N	Fe–Fe	0.53	0.62	3	2.87	3
R [Å]		3.39	3.40	3.34	3.36	3.35
$\Delta\sigma^2$ [Å^2]		0.003	0.003	0.004	0.003	-
N	Fe–O	2.66	fixed	2.89	fixed	3
R [Å]		3.40	fixed	3.38	fixed	3.39
$\Delta\sigma^2$ [Å^2]		0.008	fixed	0.006	fixed	-
N	Fe–O	2.84	fixed	2.93	fixed	3
R [Å]		3.60	fixed	3.61	fixed	3.59
$\Delta\sigma^2$ [Å^2]		0.009	fixed	0.006	fixed	-
N	Fe–Fe	-	-	2.90	2.89	3
R [Å]		-	-	3.72	3.71	3.69
$\Delta\sigma^2$ [Å^2]		-	-	0.003	0.002	-

Refinements were carried out on the back-transforms
N: coordination number; R: bond length; $\Delta\sigma^2$: Debye-Waller factor. Even though the two higher Fe-O shells make no significant contribution to the backscattering amplitude, they were included (as fixed values) in order to be able to compare them with the results gained from the refined Fourier transforms

numbers of the outer shells only occurs for particles smaller than 5 nm.

Refined structure parameters were obtained for bulk haematite (host/guest compound) by firstly fitting the back-transforms with four (three) iron–iron shells) (see Fig. 6), and then including the iron–oxygen shells (two shells in both cases, see Fig. 7).

Figures 6 and 7 show the back-transforms and the results of the refinements. The refined data are listed in Table 1, the refinement parameters in Table 2. The differences between experimental and fit data are marginal for both tables. Deviations at low k are probably due to the restricted energy shift, the influence of which is most prominent at low k values.

Comparing the fit results for the refinement with and without the iron–oxygen shells, it is remarkable that there are no significant differences between the distances and Debye-Waller factors. Due to this, and the structural information from the iron–iron shells, the iron–oxygen shell can be neglected in further data analyses and discussions.

There are three differences between the bulk material and the host/guest compound. Firstly, it is not possible to use four iron–iron shells for refinement in the case of the host/guest compound. The first or the fourth iron–iron shell cannot be fitted, as shown earlier in our group [3, 6]. The loss of important multiple scattering paths during the back-transform procedure might be one reason for this. The importance of the first iron–iron shell is apparent from the Fourier transformed fit results. Secondly, the increase in the coordination number is different, and thirdly the distances for the iron–iron shells are different too. The last two points will be discussed later on for the Fourier transform refinement results.

Figures 8 and 9 show the experimental RDFs of bulk haematite and the host/guest compound, as well as their fit results. Two iron–oxygen shells were used to fit the first peak around 1.5 Å and four iron–iron shells to fit the second FT peak. The fitted peaks at higher R-values are due to multiple scattering effects. The refined data are listed in Table 3, the refinement parameters in Table 4. The coordination numbers and distances are similar to the single crystal data for both. Normally the Debye-Waller factors increase for higher shells, as can be seen for the Fe–O shells, and tend to become smaller from Fe–Fe to Fe–O interactions, as observed in Fe–SiO_2 and NiO–SiO_2 nanocomposites [42]. This effect is not observed for the iron–

Table 2 Refinement parameters for the back-transform (BT) fitted host/guest compound and bulk haematite

	BT data without Fe–O		BT data with Fe–O	
	Bulk haematite	Host/guest compound	Bulk haematite	Host/guest compound
BTR	2.1–4.1 Å	2.1–4.1 Å	1.1–4.1 Å	1.0–4.1 Å
S_0^2	0.90	0.90	0.93	0.93
ΔE_0 [eV]	−3.03	−4.37	Fe: −4.11 O: −6.71	Fe: −5.55 O: −6.91
R [%]	4.6	5.0	6.2	7.0
N_{idp}	15	15	21	18
N_{frp}	10	9	11	10
SS	4+2 fixed	3+2 fixed	6	5
MS	0	0	0	0

BTR: Back-transform range from the Fourier transforms; S_0^2: amplitude reduction factor; ΔE_0: energy shift; R: residual; N_{frp}: number of free running parameters; N_{idp}: max number of free running parameters

iron shells here, and this can largely be explained by the smaller particle size.

The results and fit parameters gained from the refined backscattering and the Fourier transform calculations, performed with and without the iron–iron shells and the multiple scattering paths, are given in the respective tables and figures. The differences between the experimental and the refined fit data are marginal for all four bulk haematite Fe–Fe shells. Also, the refined fit results barely changed whether the iron–oxygen shells were included or not, which means that these shells can be neglected for further data analysis and discussion.

A good fit result was obtained for bulk haematite. The coordination numbers and distances agree well with the corresponding single-crystal data.

One exception can be seen, however, for the fourth iron–iron shell, where the coordination number is significantly smaller than for the single-crystal data. This reduction is

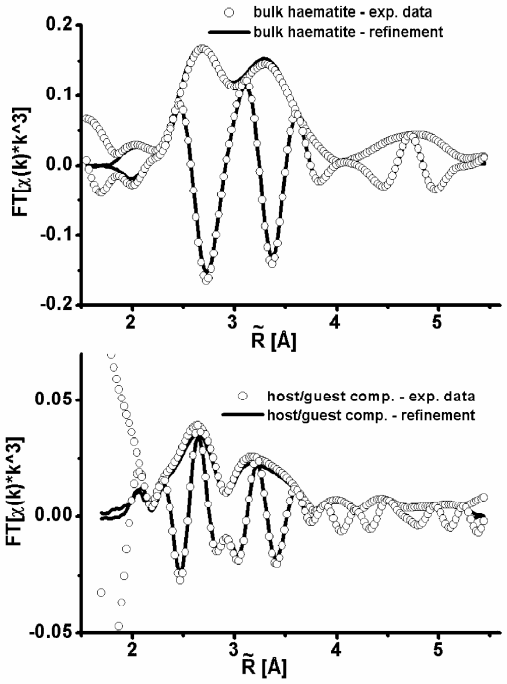

Fig. 8 Fourier transforms (FT) of bulk haematite and the host/guest compound Fe_2O_3@CMK-1, and the results of corresponding least square fits carried out on the respective iron–iron and iron–oxygen shells (fixed) with the aid of multiple scattering paths

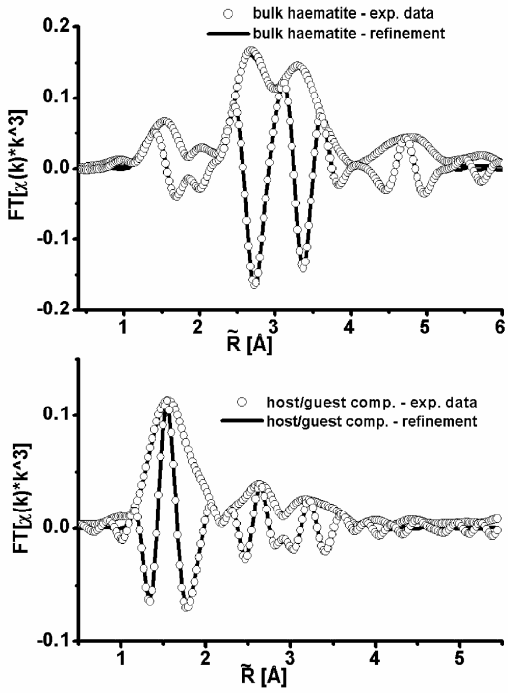

Fig. 9 Fourier transforms (FT) of bulk haematite and the host/guest compound Fe_2O_3@CMK-1, and the results of corresponding least square fits carried out on the respective iron–iron and iron–oxygen shells with the aid of multiple scattering paths

Table 3 Refined structural parameters of the iron–iron shells of the host/guest compound and bulk haematite as well as the corresponding results from single-crystal haematite data, obtained with/without refining the single scattering paths of the iron–oxygen coordination shells

Refinement	Shell	Host/guest compound		Bulk haematite		Haematite single-crystal [45]
		With Fe–O	Without Fe–O	With Fe–O	Without Fe–O	
N	Fe–O	2.92	-	3.01	-	3
R [Å]		1.92	-	1.95	-	1.94
$\Delta\sigma^2$ [Å^2]		0.008	-	0.006	-	-
N	Fe–O	2.88	-	2.99	-	3
R [Å]		2.12	-	2.10	-	2.11
$\Delta\sigma^2$ [Å^2]		0.008	-	0.007	-	-
N	Fe–Fe	0.52	0.46	0.87	0.85	1
R [Å]		2.95	2.96	2.90	2.90	2.89
$\Delta\sigma^2$ [Å^2]		0.004	0.003	0.004	0.004	-
N	Fe–Fe	1.05	0.90	2.99	2.98	3
R [Å]		2.99	2.98	2.96	2.97	2.96
$\Delta\sigma^2$ [Å^2]		0.003	0.004	0.003	0.004	-
N	Fe–Fe	0.76	0.38	3.00	2.99	3
R [Å]		3.26	3.23	3.36	3.37	3.35
$\Delta\sigma^2$ [Å^2]		0.003	0.004	0.004	0.003	-
N	Fe–O	2.79	fixed	3.03	fixed	3
R [Å]		3.31	fixed	3.40	fixed	3.39
$\Delta\sigma^2$ [Å^2]		0.007	fixed	0.006	fixed	-
N	Fe–O	2.81	fixed	2.96	fixed	3
R [Å]		3.50	fixed	3.61	fixed	3.59
$\Delta\sigma^2$ [Å^2]		0.009	fixed	0.007	fixed	-
N	Fe–Fe	1.39	0.73	4.22	3.87	3
R [Å]		3.53	3.54	3.71	3.70	3.69
$\Delta\sigma^2$ [Å^2]		0.004	0.004	0.004	0.003	-

Refinements were carried out on the Fourier transforms
N: coordination number; *R*: bond length; $\Delta\sigma^2$: Debye-Waller factor

probably due to powder particles in the bulk material, a well-known effect for higher shells. A significant shift in the Debye-Waller factors is not observed, which supports the presence of small particles.

A significant reduction in the coordination numbers for the host/guest compound can be observed. The reduction increases with distance. As for bulk haematite, the host/guest compound shows no significant shift in the Debye-Waller factors. These factors are very similar for both bulk haematite and the host/guest compound. The reduction in the coordination numbers combined with the minimal change in Debye-Waller factors shows that very small

Table 4 Refinement parameters for the Fourier transform-fitted host/guest compound and bulk haematite. The spectral range in *k* space is 3.0–15.0 Å^{-1} for all

	FT data without Fe–O		FT data with Fe–O	
	Bulk haematite	Host/guest compound	Bulk haematite	Host/guest compound
Fit range	2.1–5.3 Å	2.1–5.3 Å	1.1–5.3 Å	1.0–4.1 Å
S_0^2	0.94	0.94	0.92	0.92
ΔE_0 [eV]	−3.98	−6.07	Fe: −5.03	Fe: −6.11
			O: −6.42	O: −4.38
R [%]	5.1	7.7	4.3	6.2
N_{idp}	27	27	34	26
N_{frp}	14	13	22	15
SS	4+2 fixed	4+2 fixed	8	6
MS	7	7	7	7

S_0^2: amplitude reduction factor; ΔE_0: energy shift; *R*: residual; N_{frp}: number of free running parameters; N_{idp}: max number of free running parameters

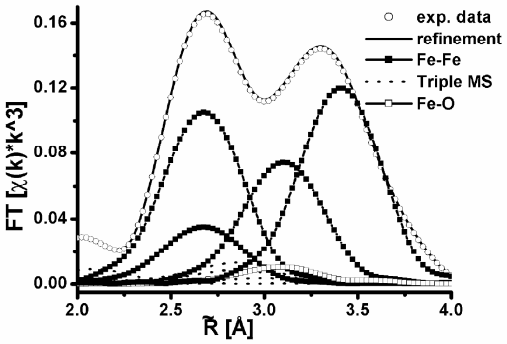

Fig. 10 XAFS refinement of bulk haematite to experimental haematite FT[$\chi(k)*k^3$]. The Fe–Fe coordination shells (weights 29, 87, 62 and 100%), the Fe–O coordination shells (weights 9 and 11%), as well as the four triple scattering paths with the highest contributions (weights estimated to be 6–18%) are shown

nanoparticles (<3 nm) are formed inside the pore system. The distances obtained for the second and fourth iron–iron shells differ from those obtained from single-crystal data. They correspond to edge- and corner-shared octahedra.

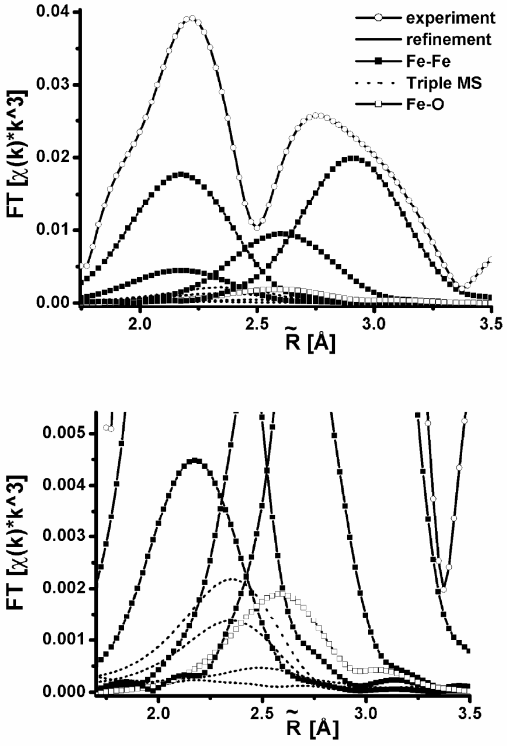

Fig. 11 XAFS refinement of the host/guest compound Fe_2O_3@-CMK-1 as an overview (*top*) and at a higher magnification (*bottom*). The Fe–Fe coordination shells (weights 23, 89, 47 and 100%), the Fe–O coordination shells (weights 9 and 10%) as well as the four triple scattering paths with the highest contributions (weights estimated to be 3–14%)

The first iron–iron shell appears at 3.01 nm, a distance where only edge-shared octahedra can form. This very important structural fact, that no face-shared octahedra are found in the host/guest compound, can be lost when refining the back-transforms. On the other hand, no proof of the corner-shared linkage of the fourth shell was found when refining the back-transforms of the first iron–iron shell. It is therefore difficult to ascertain whether the host has haematite structure or whether it is a haematite-like iron (III) oxide. Full information about the coordination numbers and the distances are only obtained by fitting the Fourier transform over a wide range and using the relevant multiple scattering paths. Furthermore, the distances obtained from the refined FT are closer to the distances observed in the single-crystal data than to those gained by refining the back-transforms, due to the reason mentioned above.

As discussed in earlier, a specially refined FEFF file was used for XAFS simulation and refinement. This means that the weights and angles of the multiple scattering paths were adapted to the structure of this bulk haematite. Figures 10 and 11 show the single and the two strongest multiple scattering paths that contribute to the EXAFS fits of the host/guest compound and bulk haematite for 2–4 Å. The declared weights of about 18% (16% for bulk haematite, referring to the strongest amplitude) for the multiple scattering paths underlines once more the need to use them. The influence of the multiple scattering paths increases with increasing amplitude, as shown by the quality of the results for the host/guest compound. The refined FEFF file, and therefore the application of the multiple scattering paths, allows us to reach the conclusions made here.

Conclusions

Fluorescence EXAFS investigations were carried out in order to obtain information on the structure of nanosized iron(III) oxide inside the pore system of mesoporous carbon. Due to large number of structures possible (not only in terms of the host/guest chemistry), a detailed study of the recording, preparation and evaluation of the data is presented. The EXAFS results show that most of the structural information can be obtained by refining the radial distribution function with the relevant multiple scattering paths over a wide range.

It was shown that the use of multiple scattering paths in refined Fourier transforms performed over a wide range can reveal results that are difficult or impossible to probe with other spectroscopic methods. The authors think that the procedure described above can be applied to nanostructured particles of <4 nm in general, and it is not restricted to host/guest chemistry.

Acknowledgements The authors would like to thank HASYLAB@DESY, Hamburg, Germany, for allocating beam time and financial support. Further financial support from the Justus Liebig University Giessen and the Fonds der Chemischen Industrie is gratefully acknowledged.

References

1. Wang L-Z, Shi J-L, Zhang W-H, Ruan M-L, Yu J, Yan D-S (1999) Chem Mater 11:3015
2. Köhn R, Brieler F, Fröba M (2000) Stud Surf Sci Catal 129:341–348
3. Köhn R, Fröba M (2001) Catal Today 68:227–236
4. Minchev C, Köhn R, Tsoncheva T, Dimitrov M, Mitov I, Paneva D, Huwe H, Fröba M (2002) Stud Surf Sci Catal 142:1245–1252
5. Dapurkar SE, Badamali SK, Selvam P (2001) Catal Today 68:63–68
6. Fröba M, Köhn R, Boufffaud G, Richard O, v. Tendeloo G (1999) Chem Mater 11:2858–2865
7. Köhn R, Paneva D, Dimitrov M, Tsoncheva T, Mitov I, Minchev C, Fröba M (2003) Microporous Mesoporous Mater 63:125–137
8. Köhn R, Fröba M (2003) Z Anorg Allg Chem 629:1673–1682
9. Nguyen SV, Szabo V, Trong On D, Kaliaguine S (2002) Microporous Mesoporous Mater 54:51–61
10. Zhao DY, Goldfarb DJ (1995) J Chem Soc Chem Commun 875–876
11. Yang C-M, Sheu H-S, Chao K-J (2002) Adv Funct Mater 12:143–148
12. Morey MS, O'Brien S, Schwarz S, Stucky GD (2000) Chem Mater 12:898
13. Walker JV, Morey M, Carlsson H, Davidson A, Stucky GD, Butler A (1997) J Am Chem Soc 119:6921
14. Widenmeyer M, Grasser S, Köhler K, Anwander R (2001) Microporous Mesoporous Mater 44:327–336
15. Schrijnemakers K, Vansant EF (2001) J Porous Mater 8:83–90
16. Selvam P, Dapurkar SE (2004) Appl Catal A: General 276: 257–265
17. Van der Voort P, Baltes M, Vansant EF (1999) J Phys Chem B 103:10102–10108
18. Van der Voort P, Vansant EF (2000) Microporous Mesoporous Mater 38:385–390
19. Han,Y-J, Kim JM, Stucky GD (2000) Chem Mater 8(12): 2068–2069
20. Brieler F, Grundmann P, Fröba M, Chen L, Klar PJ, Heimbrodt W, Krug von Nidda H-A, Kurz T, Loidl A (2005) Chem Mater 17(4):795–803
21. Martinez F, Han Y-J, Stucky G, Sotelo JL, Ovejero G, Melero JA (2002) Stud Surf Sci Catal 142B:1109–1116
22. Schlecht S, Yosef M, Fröba M (2004) Z Anorg Allg Chem 630:864–868
23. Brieler F, Grundmann P, Fröba M, Chen L, Klar PJ, Heimbrodt W, Krug von Nidda H-A, Kurz T, Loidl A (2004) J Am Chem Soc 126:797–807
24. Zhang Z, Dai S, Blom DA, Shen J (2002) Chem Mater 14: 965–968
25. Zhang WH, Lu J, Han B, Li M, Xiu J, Ying P, Li C (2002) Chem Mater 14:3413–3421
26. Trong On D, Desplantier-Giscard D, Danumah C, Kaliaguine S (2001) Appl Catal A: General 222:299–357
27. Weitkamp J, Glaeser R, Dittmeyer R (eds) (2004) Winnacker-Kuechler: Chemische Technik 1:645–718 Wiley-VCH Verlag, Weinheim, Germany
28. Ryoo R, Joo SH (2004) Stud Surf Sci Catal 148:241–260
29. Ryoo R, Joo SH, Jun S (1999) J Phys Chem B 103(37):7743–7746
30. Joo SH, Jun S, Ryoo R (2001) Microporous Mesoporous Mater 44(45):153–158
31. Kruk M, Jaroniec M, Ryoo R, Joo SH (2000) J Phys Chem B 104:7960–7968
32. Ryoo R, Joo SH, Krug M, Jaroniec M (2001) Adv Mater 13 (9):677–681
33. Kaneda M, Tsubakiyama T, Carlsson A, Sakamoto Y, Ohsuna T, Terasaki O (2002) J Phys Chem B 106:1256–1266
34. Jun S, Joo SH, Ryoo R, Kruk M, Jaroniec M, Liu Z, Ohsuna T, Terasaki O (2000) J Am Chem Soc 122(43):10712–10713
35. Joo SH, Choi SJ, Oh I, Kwak J, Liu Z, Terasaki O, Ryoo R (2001) Nature 412:169–172
36. Huwe H, Fröba M (2003) Microporous Mesoporous Mater 60:151–158
37. Minchev C, Huwe H, Tsoncheva T, Paneva D, Dimitrov M, Mitov I, Fröba M (2005) Microporous Mesoporous Mater 8:333–341
38. Tsoncheva T, Paneva D, Mitov I, Huwe H, Fröba M, Dimitrov M, Minchev C (2004) React Kinet Catal Lett 83:299–305
39. Tuel A, Arcon I, Millett JMM (1998) J Chem Soc Faraday Transactions 94(23):3501–3510
40. Wong S-T, Lee J-F, Cheng S, Mou C-Y (2000) Appl Catal A: General 198:115–126
41. Burch R, Cruise N, Gleeson D, Tsang SC (1998) J Mater Chem 8:227–231
42. Henke BL, Gullikson EM, Davis JC (1993) Atomic Data Nucl Data Tables 54:181–342
43. Corrias A, Ennas G, Mountjoy G, Paschina G (2000) Phys Chem Chem Phys 2:1045–1050
44. Pauling L, Hendricks SB (1925) J Am Chem Soc 47:781–790
45. Blake RL, Hessevick RE, Zoltai T, Finger LW (1966) Am Mineral 51:123–129
46. Ennas G, Marongiu G, Musino A, Falqui A, Ballirano P, Caminiti R (1999) J Mater Res 14:1570–1575
47. Onodera S, Kondo H, Kawana T (1996) MRS Bullettin 21: 35–41
48. Lund CRF, Dumesic JA (1982) J Phys Chem 86:130–135
49. Torok SB, Van Grieken RE (1994) Anal Chem 66:186–206
50. Becker KD, Niemeier D, Wissmann S, Oversluizen M, Couves JW, Chadwick AV (1995) Nucl Instr Meth Phys Res B 97:111–114
51. Lee PA, Citrin PH, Eisenberger P, Kincaid BM (1981) Rev Mod Phys 53:769–806
52. De Groot FM, Fuggle JC, Thole BT, Sawatzky GA (1999) Phys Rev B 42:5459–5468
53. Lee PA, Pendry JB (1975) Phys Rev B 11:2795–2811
54. Manceau A, Drits VA (1993) Clay Minerals 28:165–184
55. Moscovici J, Benzakour M, Decker S, Carnes C, Klabunde K, Michalowicz A (2001) J Synchrot Radiat 8:925–927
56. Rehr JJ, Ankudinov A, Zabinsky SI (1998) Catal Today 39:263–269
57. Meitzner G (1998) Catal Today 39:281–291
58. Wu ZY, Gota S, Jollett F, Pollak M, Gautier-Soyer M, Natoli CR (1997) Phys Rev B 55:2570–2577
59. Koningsberger DC, Mojet BI, Van Dorssen GE, Ramaker DE (2000) Topics Catal 10:143–155
60. Kitamura M, Muramatsu S, Sugiura C (1986) Phys Rev B 33:5294–5300
61. Crocombette JP, Pollak M, Jollett F, Thromat N, Gautier-Soyer M (1995) Phys Rev B 52:3143–3150
62. Chou SH, Guo J, Ellis DE (1986) Phys Rev B 34:12–24
63. Alberding N, Crozier ED (1983) Phys Rev B 27:3374–3382
64. Sevillano E, Meuth H, Rehr JJ (1979) Phys Rev B 20:4908–4911
65. Grunes LA (1983) Phys Rev B 27:2111–2131
66. Caliebe WA, Kao CC, Hastings JB, Taguchi M, Kotani A, Uozumi T, de Groot FMF (1998) Phys Rev B 58:13452–13458
67. Waychunas GA, Kim CS, Banfield JF (2005) J Nanoparticle Res 7:409–433
68. Ressler T (1998) J Synchrot Radiat 5:118–122
69. http://www.winxas.de
70. Newville M, Ravel B, Haskel D, Rehr JJ, Stern EA, Yacoby Y (1995) Phys B 208:154–156
71. http://leonardo.phys.washington.edu/~ravel/software/atoms/
72. Ravel B (2001) J Synchrot Radiat 8:314–316
73. Gurman SJ, Binsted N, Ross I (1984) J Phys C 17:143–151
74. Van Barth U, Hedin L (1972) J Phys C 5:1629–1642
75. Crozier ED (1997) Nucl Instr Meth Phys Res B 133:134–144
76. Li GG, Bridges F, Booth CH (1995) 52:6332–6648
77. Greegor RB, Lytle FW (1980) J Catal 63:476–486

CARBON 4265
13 October 2006 Disk Used
ARTICLE IN PRESS
No. of Pages 11, Model 5+

Available online at www.sciencedirect.com
ScienceDirect

ELSEVIER

Carbon xxx (2006) xxx–xxx

CARBON

www.elsevier.com/locate/carbon

Synthesis and characterization of transition metal and metal oxide nanoparticles inside mesoporous carbon CMK-3

Holger Huwe, Michael Fröba *

Institute of Inorganic and Analytical Chemistry, Justus Liebig University Giessen, Heinrich-Buff-Ring 58, 35392 Giessen, Germany

Received 16 April 2006; accepted 16 September 2006

Abstract

Transition metal oxides were synthesized inside the pore system of mesoporous carbon CMK-3. By a wet impregnation, drying and calcination procedure iron, copper, nickel, cobalt, manganese and zinc oxides were formed almost exclusively within the mesopores. A reduction into the metal forms with regard to structural array in the case of zinc oxide and a reduction to manganese(II) oxide for manganese(IV) oxide was accomplished by hydrogen. Powder X-ray diffraction (PXRD), Raman spectroscopy and transmission electron microscopy (TEM) proved the preservation of the host structure during impregnation and reduction procedures. The formation of nano-sized metal oxides inside the mesopore system was confirmed with PXRD and TEM. Nitrogen physisorption measurements still revealed micro- and mesoporosity for the host/guest compounds. A reduction of the surface areas and pore sizes in contrast to the host structure being an indication of the coating of the inner surfaces of the carbon walls is shown as well. Infrared and X-ray absorption spectroscopy (XAS) carried out in fluorescence mode confirm the formation of the respective oxides and metals. Furthermore, the existence of small, disordered nanoparticles was proved by XAS investigations and information on the local structure of the metals and metal oxides was obtained from these measurements.

Keywords: Molecular sieves; Chemically modified carbons; Porous carbon; Impregnation; Porosity

1. Introduction

Since the discovery of ordered mesoporous carbons by Ryoo et al. [1] these so-called CMK-*n* (*n* = 1–9) materials gained a rapidly growing interest in materials science. The most investigated carbon material of this series is the CMK-3 as it can be seen in a number of publications dealing with the synthesis, characterisation and the properties of this material (see, e.g. [2–16]). CMK-3 is synthesized by applying the mesoporous silica sieve SBA-15 as a template and sucrose as the carbon source via an impregnation procedure [3,4]. The pristine CMK-3 and the SBA-15 silica show couple of similarities. Both materials are 2-d hexagonal structured (space group: p6mm) and exhibit micro- and mesopores. The specific surface areas (BET) of the CMK-3 material up to 1600 m^2/g are higher compared to the SBA-15 (BET: ~600 m^2/g). In contrast to the pure mesoporous silica materials the carbon materials show characteristic features as for example the high stability in strong acids and bases, high mechanical stability and electric conductivity which is of particular importance [2–4,9,16]. There are numerous potential applications of carbonaceous materials such as adsorption, catalytic reactions, fuel–cell electrodes or molecular sieving [5,14–17]. Concerning these applications the mesopores within the CMK-3 network might be an advantage compared to the microporous carbonaceous materials such as zeolites [18–23]. Therefore, the mesoporous carbon CMK-3 is for instance investigated with respect to its adsorption behaviour [14,24] and as a carrier of catalysts [12]. It is also used for electronic application [16], electrochemical capacitance studies [25,26] as well as in the host/guest chemistry [5,10–12]. Whereas the host/guest

* Corresponding author. Tel.: +49 641 9934 100; fax: +49 641 9934 109.
E-mail address: michael.froeba@anorg.chemie.uni-giessen.de (M. Fröba).

0008-6223/$ - see front matter © 2006 Elsevier Ltd. All rights reserved.
doi:10.1016/j.carbon.2006.09.021

Please cite this article in press as: Huwe H, Fröba M, Synthesis and characterization of transition metal and metal ..., Carbon (2006), doi:10.1016/j.carbon.2006.09.021

CARBON 4265 ARTICLE IN PRESS No. of Pages 11, Model 5+
13 October 2006 Disk Used

chemistry with siliceous hosts and metal oxides or the respective metals is already established and represents a promising direction [27–32], the host/guest chemistry with carbon hosts is still in its initial stage.

Due to the pore structure, physical and chemical properties marginally discussed above, the mesoporous carbon CMK-3 might be of significance as a matrix for catalytic active species as Mn, Fe, Cu or Co as known from silicate mesoporous materials [28–30, and references therein]. Other fields of interests might be the investigation of the magnetic behaviour of metals, metal oxides and magnetic diluted semiconductors in the mesopores of CMK-3. Primal investigations concerning these topics have been carried out and will be published soon by the authors' group.

The synthesis of the host/guest compounds can be accomplished by two different procedures: Firstly, the addition of the metal ions during the synthesis of the mesoporous carbon and secondly, a post-synthetic incorporation of the metals into the pore network. In this study the post-synthetic incorporation via a wet impregnation and calcination procedure was chosen. The advantages of this method are the high quality mesoporous material as basic material and the possibility of a higher loading of the mesopores with the guest compound. A very accurate preparation is of great importance to reveal the host structure of high quality. During the last years our working group achieved a great deal by applying the wet impregnation technique in the host/guest chemistry [28,31–33, et al. in].

In this study the authors present a detailed examination on the intra-pore synthesis of manganese, iron, cobalt, nickel, copper and zinc in the oxide form inside the mesopores of CMK-3. An intra pore reduction was accomplished in order to transform the metal oxides into the metal form respectively, a structural array in the case of zinc oxide and a reduction to manganese(II) oxide for manganese(IV) oxide. With the combination of comprehensive characterization methods such as powder X-ray diffraction (PXRD), liquid nitrogen physisorption, Raman spectroscopy and transmission electron microscopy (TEM), the preservation of the host structure during these procedures is verified. The formation of the metal oxides almost exclusively inside the mesopore system is confirmed with PXRD and TEM. The formation of nanosized metal oxides and metals is shown with infrared spectroscopy and X-ray absorption spectroscopy (XAS). Additionally, XAS investigations were carried out in order to obtain information on the local structure of the respective metals and metal oxides.

2. Synthesis

2.1. Synthesis of mesoporous carbon

The synthesis of the host structure CMK-3 was carried out using SBA-15 silica as the hard template and sucrose as the carbon source following the synthesis procedure described by Jun et al. [3]. The preparation of the SBA-15 silica is based on the synthesis procedure first reported by Zhao et al. [34,35].

2.2. Synthesis of nanostructured metal oxides inside mesoporous carbon

The loading of the host structure was carried out by applying the wet impregnation method as reported by the authors [33]. The respective 1.6 molar ethanolic metal nitrate solution (100 mL) was stirred for 24 h at room temperature with 1 g dried CMK-3. The carbon–metal nitrate composition was separated from the solution by centrifugation (2900 rotations/min, 5 min). The resulting material was first dried in air and subsequent by means of vacuum at room temperature. It should be mentioned that rapid drying leads to formation of nanosized metal oxide particles outside the pores. By heating the samples to 573 K in an air stream for 4 h the transformation from the nitrate to the oxide form was achieved. The resulting host/guest compounds are designated as Me_xO_y@CMK-3 whereas Me_xO_y indicates the respective metal oxide. In the case of Fe_2O_3 the iron oxide with hematite like structure (α-Fe_2O_3) is meant. With the described procedure, metal oxide loadings in the range of 12–15 wt% were obtained.

To improve the synthesis procedure and as references for the XAFS investigations bulk metal oxides were synthesized in the same way and the formation of the bulk metal oxides was proved with powder X-ray diffraction.

2.3. Reduction

The reductions of the samples Me_xO_y@CMK-3 were carried out with a ChemBET 3000 (Quantachrome Instr.) at 1100 K for 1 h. The reduction gas was a mixture of 4% hydrogen in nitrogen, the gas flow was 25 cm^3/min. The reduced host/guest compounds are designated as Me@CMK-3 whereas Me indicates the respective metal, redZnO@CMK-3 in the case of ZnO@CMK-3 and MnO@CMK-3 for MnO_2@CMK-3.

As an evidence for the complete reduction and as references for the XAS investigations bulk metal oxides were reduced in the same way and the formation was proved with powder X-ray diffraction.

3. Characterization methods

The samples were analyzed by powder X-ray diffraction (PXRD) with filtered CuK_α radiation using a Bruker AXS D8 Advance diffractometer in Θ/Θ geometry (continuous scan mode: speed: 0.02 °(2Θ)/min and counting time of 6 s/data point).

Infrared spectra were recorded on a Perkin–Elmer spectrum GX FTIR spectrometer in the range between 400 and 4000 cm^{-1} using the KBr pellet method.

Nitrogen physisorption measurements were recorded with an Autosorb 6 (Quantachrome Instr.) for isotherm and surface area analysis and with an Autosorb 1 (Quanta-

Please cite this article in press as: Huwe H, Fröba M, Synthesis and characterization of transition metal and metal ..., Carbon (2006), doi:10.1016/j.carbon.2006.09.021

CARBON 4265 ARTICLE IN PRESS No. of Pages 11, Model 5+
13 October 2006 Disk Used

chrome Instr.) for micropore analysis, in each case at 77 K. Before starting the physisorption measurements the samples were outgassed at 423 K for 18 h. The specific surface areas were calculated from the adsorption branch in the p/p_0 range of 0.03 and 0.20 (depending on the number of points that were appropriate for a linear fit) applying the Brunauer, Emmet and Teller (BET) method [36]. The pore size distributions were calculated using the Barrett–Joyner–Halenda (BJH) formula [37] and the density functional theory with the respective kernels [38–43].

Raman spectra were recorded using a Raman microscope system (Jobin–Yvon). The argon-ion laser operated at 514.5 nm. The laser power is rough about 10–20 mW and the spot size is about 0.5–1.0 square millimetre. The resolution of the spectra was 1 cm^{-1}.

Transmission electron microscopic images were taken with a Philips CM30 operating at 300 kV in bright field mode. The sample preparation was accomplished by suspending the materials in acetone and dispersing them on a holey carbon grid.

X-ray absorption spectroscopic measurements were carried out at the storage ring DORIS III (HASYLAB@DESY, Hamburg, Germany) at the EXAFS beam line A1 that was equipped with a Si(1 1 1) double-crystal monochromator. The metal-K edge spectra were acquired at liquid nitrogen temperature (77 K). All spectra were recorded in fluorescence mode up to four times to improve the signal to noise ratio by addition of the single spectra. The samples were measured in form of fresh pressed boron nitride pills. For further data analysis the programs WinXAS3.1 [44] and FEFF8 [45] were used.

4. Results and discussion

4.1. Infrared spectroscopy

The transformation from the nitrate into the oxide form was confirmed with infrared spectroscopic measurements. Fig. 1 shows the IR spectra of the pristine host CMK-3 (a), the CMK-3 loaded with iron nitrate (c) and iron oxide (b) as well as the CMK-3 loaded with manganese nitrate (e) and manganese(IV) oxide (d). The disappearance of the IR vibration of the NO_3^- ion at 1380 cm^{-1} after heating indicates the complete transformation.

4.2. Powder X-ray diffractometry

Powder X-ray diffraction investigations permit the characterization of ordered micro- and mesoporous materials by analysing the packing of the pores. The determination of the host/guest compounds and the confirmation of the incorporation of scattering material inside the mesopores can be obtained as well by this method.

From the diffraction patterns (example see Fig. 2) we can conclude the formation of the metal oxides almost exclusively inside the mesopores of the host structure. The d-spacings and the lattice constants of the host material and the host/guest compounds as metal oxides and metals inside the CMK-3 extracted from the PXRD data are listed in Table 1.

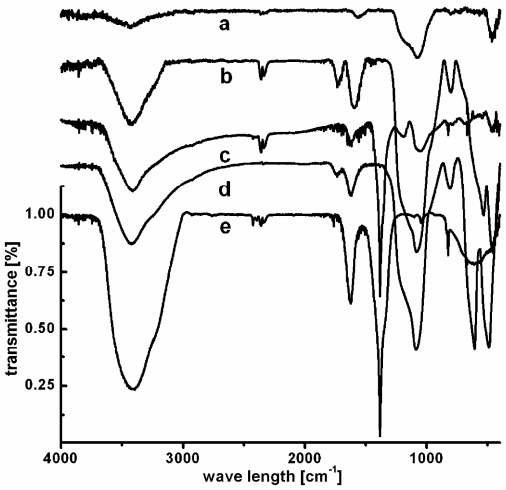

Fig. 1. Infrared spectra of (a) the pristine host CMK-3, (b) Fe_2O_3@CMK-3, (c) $Fe(NO_3)_3$@CMK-3, (d) MnO_2@CMK-3 and (e) $Mn(NO_3)_2$@CMK-3.

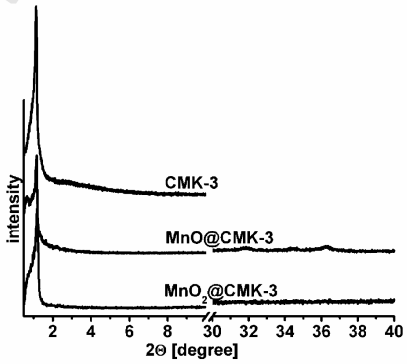

Fig. 2. PXRD patterns of Mn_xO_y@CMK-3 and the pristine host structure CMK-3.

The first reflection of the host CMK-3 can be indexed as 100 reflection of the 2-d hexagonal structure with the space group p6mm [8]. The incorporation of the metal oxides into the pore network of the carbon material leads to a reduction of the scattering intensities of all Bragg reflections. As expected, a slow shift to smaller d-spacings could be observed which was discussed in previous publications [29,31] (see Table 1). Additionally, no reflections in the higher 2Θ range could be observed for Fe_2O_3@CMK-3, Co_3O_4@CMK-3, NiO@CMK-3 and ZnO@CMK-3. The absence of the most prominent reflections of the metal oxi-

Please cite this article in press as: Huwe H, Fröba M, Synthesis and characterization of transition metal and metal ..., Carbon (2006), doi:10.1016/j.carbon.2006.09.021

CARBON 4265 ARTICLE IN PRESS No. of Pages 11, Model 5+
13 October 2006 Disk Used

Table 1
D-spacings and lattices constants of the CMK-3 and the host/guest compounds

Sample	d_{100} (nm)	a (nm)	Sample	d_{100} [nm]	a (nm)
CMK-3	7.78	8.98	–	–	–
MnO_2@CMK-3	7.65	8.83	MnO@CMK-3	7.67	8.85
Fe_2O_3@CMK-3	7.58	8.75	Fe@CMK-3	7.63	8.81
Co_3O_4@CMK-3	7.39	8.53	Co@CMK-3	7.66	8.84
NiO@CMK-3	7.51	8.67	Ni@CMK-3	7.68	8.87
CuO@CMK-3	7.48	8.64	Cu@CMK-3	7.60	8.78
ZnO@CMK-3	7.38	8.52	redZnO@CMK-3	7.61	8.79

d_{100}: d-spacing; a: lattice constant, $a = 2 * 3^{-1/2} * d_{100}$.

des indicates no crystalline metal oxide particles being outside the mesopore system. The appearances of broad high order Bragg reflections in the region of $2\Theta = 30°–40°$ as noticed for MnO_2@CMK-3 and CuO@CMK-3 corresponds to very small amorphous metal oxide crystallites. By applying the Scherrer formula the crystallite size can be roughly estimated to be about 2.5 nm in diameter for CuO@CMK-3 and 2.1 nm in diameter for MnO_2@CMK-3. From these calculations we assume the oxide particles synthesized within the pores to be too small to lead to X-ray reflections.

As it can be seen from Fig. 2 the host structure is still intact after the reduction procedure. Due to the transformation from the oxide into the pure metal form, the broad high order Bragg reflections observed in the region of $2\Theta = 30°–40°$ for CuO@CMK-3 disappeared. In the case of MnO_2@CMK-3 we assume that the disappearance of the high order Bragg reflections can probably be attributed to a tempering effect due to the heat treatment during the reduction process. The bump observed for Co@CMK-3 in the higher 2Θ range is undersized and too broad to be indexed as a scattering reflection.

Moreover, the absence of these reflections in the higher 2Θ range for all samples, prove the preservation of the host structure during the formation of the nanosized metals respective MnO and ZnO in the pore system of CMK-3. As it can be extracted from Table 1, the d-spacings and the latter constants are shifted slightly to higher values after reduction, indicating the oxygen atoms to be disappeared from the pore system respective a structural enhancement in the case of ZnO@CMK-3.

4.3. Raman spectroscopy

In order to verify the preservation of the host structure during the impregnation and reduction procedure Raman spectroscopic measurements were carried out. The recorded Raman spectra are depicted in Fig. 3. For CMK-3 as well as for all host/guest compounds two bands appear at 1333 cm^{-1} and 1592 cm^{-1} as known from iron(III)oxide in mesoporous carbon CMK-1 [33]. These Raman bands are described as "disordered sp^2 bonded graphite" in the literature [46]. This is in agreement with the presumption of Darmstadt et al. who propose a graphite like structure for CMK-3 [14].

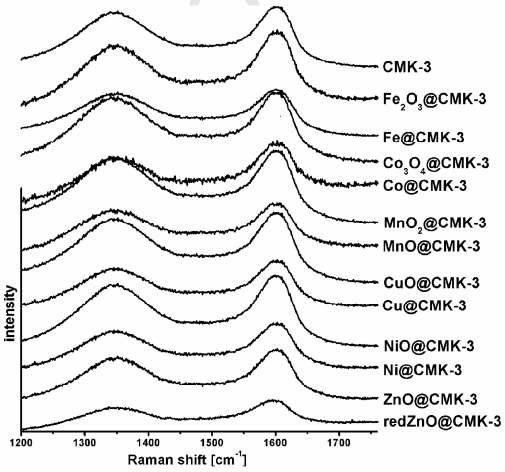

Fig. 3. Raman spectra of the parent CMK-3 material, the host/guest compounds loaded with the metal oxides and the host/guest compound loaded with the reduction products.

4.4. Transmission electron microscopy

The transmission electron micrographs (Fig. 4) show the selected representative host-guest compounds MnO@CMK-3 and redZn@CMK-3. It can clearly be seen, that the host structure reveals intactness after the impregnation and reduction procedure. In addition, no metal oxide particles could be detected on the surface in particular for MnO_2@CMK-3 and CuO@CMK-3. Due to the low metal oxide loading theirs detection is hampered in some regions of the host structure. No spots of metal oxides were detectable onto the surface. This fact is a further hint of the formation of the metal oxides inside the pore system. The micrographs of the reduced samples show the preservation of the host structure as well.

4.5. Nitrogen physisorption

Beside powder X-ray diffraction the most important characterization method of micro- and mesoporous materials is nitrogen physisorption measurements. From the

Please cite this article in press as: Huwe H, Fröba M, Synthesis and characterization of transition metal and metal ..., Carbon (2006), doi:10.1016/j.carbon.2006.09.021

CARBON 4265
13 October 2006 Disk Used
ARTICLE IN PRESS
No. of Pages 11, Model 5+

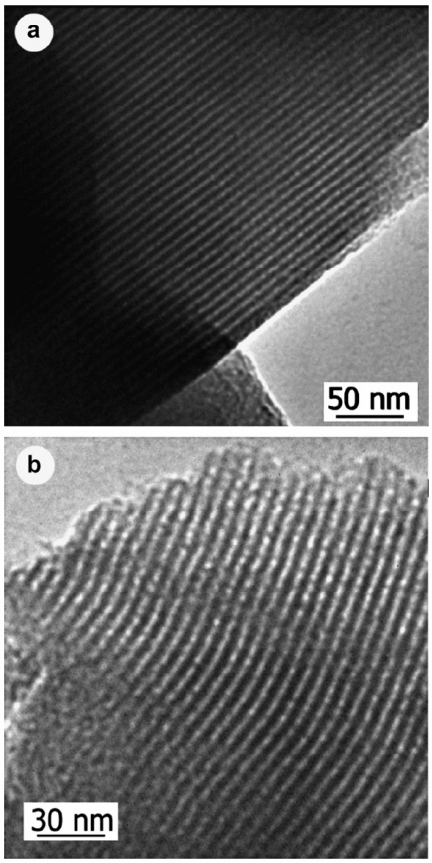

Fig. 4. Representative high resolution TEM photographs of (a) MnO@CMK-3 and (b) redZn@CMK-3.

IUPAC classifications of the isotherms information about the porous nature of the materials could be obtained. By applying the Brunauer, Emmet and Teller (BET) theory accurate statements of the specific surface areas can be made. But the correct evaluation of the mean pore diameters of our synthesised host materials and especially the host/guest compounds is difficult. Applying the BJH theory, pore diameter investigations are correct for pore diameters larger than 4 5 nm. For pore diameters below 4 5 nm the calculation via the BJH theory is awkward and leads to incorrect results, but in spite of this problem this method is still commonly used. The BJH calculations are based on the Kelvin equation and lead to an underestimation of the pore size of about 1 nm for pores <4–5 nm [41,42]. The concluding underestimation of the pore sizes can be attributed to a filling of the pores with liquid nitrogen in a continuous way rather than in stepwise layering [38]. However, the BJH theory is commonly used for the calculation of pore diameters up to 2 nm with in spite of the fault mentioned above.

The host compound CMK-3 and also the host/guest compounds described above show BJH mesopore diameters in the range of 3–4 nm and, what is more important, a high amount of micropores. Therefore calculations of pore diameters were made by applying the more accurate non-local density functional theory (NLDFT) [39,40] even though it includes some other problems that will be discussed later.

The isotherm of the host material CMK-3 is shown in Fig. 5a. By loading the CMK-3 with the respective metal oxides the adsorbed amount of liquid nitrogen decreases for all investigated samples, see Table 2. After the reduction the adsorbed volume of nitrogen increases except for samples loaded with nickel and copper. The increase of the adsorbed amounts of liquid nitrogen is due to the transformation from the oxide to the reduced form combined with it a loss of the oxygen atoms and, accordingly, a structural transformation leading to smaller and/or better structured particles. Another reason might be the disappearance of an eventual pore blocking.

All isotherms are classified as type IV isotherms, which are typical for mesoporous materials and slit pore geometry by IUPAC [47]. At a relative pressure p/p_0 of about 0.5 a step occurs, associated with the filling of the mesopores due to capillary condensation. In some cases only a weak step appears as for NiO@CMK-3 and Fe_2O_3@CMK-3, indicating a very high degree of pore filling and/or pore blocking. With the intra-pore formation of the ZnO and Fe_2O_3 in the resulting materials ZnO@CMK-3 and Fe_2O_3@CMK-3 the step of the capillary condensation is slightly broadened, representing a less uniform remaining pore size probably caused by inhomogeneous pore filling. All samples still exhibit micropores as to be seen in the run of the isotherms taken for NLDFT analysis (Fig. 6).

Starting from a BET surface area of about 1154 m^2/g for the pristine host material CMK-3 the surface areas decrease significantly after incorporating the respective metal oxide compound in the pore network as listed in Table 2. After the reduction process the surface areas are the same dimension except for the samples enriched with iron, cobalt and zinc oxide. Here an increase of about 100 m^2/g is observed. Nevertheless, it has to be kept in mind that the fault of the estimation of the surface areas calculated from the amounts of adsorbed liquid nitrogen is in the region of approximately ± 50 m^2/g depending on the weight error of the sample and the enrichment of the host material, which itself leads to a decrease of the inner surface areas.

The evaluation of the pore diameters is, as mentioned above, not satisfying. Fig. 5b shows the pore diameter distribution of the pristine host CMK-3 calculated with the BJH and the NLDFT method. The mesopore diameter differs round about 1 nm, whereas the discrepancy in the micropore range is serious. For the pore size distribution in the micropore range the NLDFT method gives more

Please cite this article in press as: Huwe H, Fröba M, Synthesis and characterization of transition metal and metal ..., Carbon (2006), doi:10.1016/j.carbon.2006.09.021

CARBON 4265
13 October 2006 Disk Used
ARTICLE IN PRESS
No. of Pages 11, Model 5+

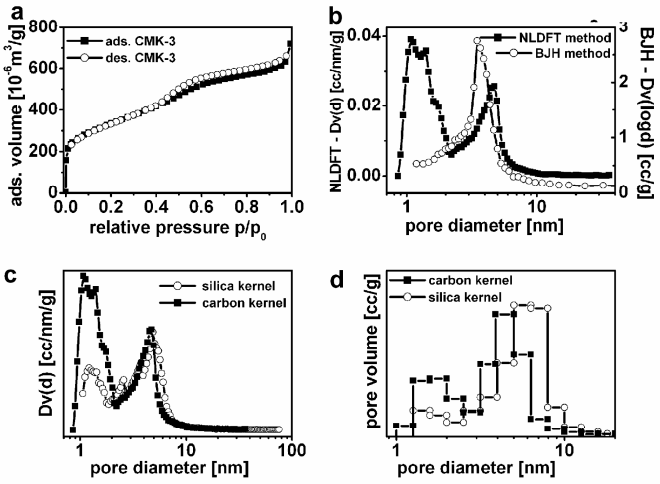

Fig. 5. The pristine host material CMK-3: (a) Liquid nitrogen isotherm, comparison of the (b) pore diameter distributions calculated, applying the BJH and the NLDFT method, (c) pore diameter distributions calculated with the NLDFT method, applying the silica kernel with cylindrical pore geometry and the carbon kernel with slit pore geometry and (d) pore volume histograms calculated with the NLDFT method, applying the silica kernel with cylindrical pore geometry and the carbon kernel with slit pore geometry.

Table 2
Liquid nitrogen physisorption data

Sample	S_{BET} (m^2/g)	D_p (nm)	$V_{p,total}$ (cc/g)	$V_{p,micro}$ (cc/g)	$V_{p,meso}$ (cc/g)
CMK-3	1154	3.82	0.87	0.11	0.76
MnO_2@CMK-3	390	3.63	0.37	0.03	0.34
Fe_2O_3@CMK-3	172	3.45	0.09	0.01	0.08
Co_3O_4@CMK-3	262	3.63	0.22	0.01	0.21
NiO@CMK-3	364	3.77	0.22	0.04	0.18
CuO@CMK-3	287	3.68	0.36	0.01	0.35
ZnO@CMK-3	135	3.69	0.17	0.01	0.16
MnO@CMK-3	403	3.65	0.41	0.04	0.37
Fe@CMK-3	270	3.80	0.16	0.04	0.12
Co@CMK-3	356	3.64	0.34	0.04	0.30
Ni@CMK-3	372	3.78	0.23	0.05	0.18
Cu@CMK-3	303	3.69	0.38	0.02	0.36
redZnO@CMK-3	279	3.72	0.31	0.02	0.29

S_{BET}: total surface area by BET theory; D_p: mean mesopore diameter by BJH calculated from the respective desorption branch; $V_{p,x}$ respective pore volumes by NLDFT.

realistic values. This is not surprising taking into account that the BJH theory is not valid in this pore diameter region. That is the reason why the NLDFT method is the better choice.

The NLDFT method works with so-called kernels. For each adsorbent a special kernel has to be chosen depending on the pore structure and the surface of the adsorbent. In the case of CMK-3 a carbon kernel with cylindrical pore geometry should be applied for NLDFT calculations. Unfortunately, such a kernel does not exist up to now, so that a carbon kernel with slit pore geometry has to be appropriate under these circumstances. In case of the host/guest compounds an oxygen (siliceous) kernel with cylindrical pore geometry was used. These kernels are applicable in a pore diameter range of 1.8–100 nm for siliceous and 0.35–8 nm for carbonaceous materials [43]. The NLDFT results gained with the carbon and silica kernel are shown in Fig. 5c. For mesopore diameters the results are nearly the same, a slight increase to larger mesopores can be observed for results gained with the silica kernel. In contrast, the estimated micropore diameters differ significantly with respect to the adsorbed volume. However, for samples with a high amount of micropores combined with a broad pore size distribution as observed for our samples, it is more convenient to show the pore volume histogram instead of the average pore size distribution. By showing

Please cite this article in press as: Huwe H, Fröba M, Synthesis and characterization of transition metal and metal ..., Carbon (2006), doi:10.1016/j.carbon.2006.09.021

CARBON 4265
13 October 2006 Disk Used
ARTICLE IN PRESS
No. of Pages 11, Model 5+

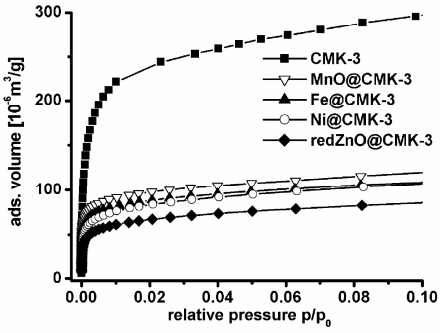

Fig. 6. Liquid nitrogen adsorption isotherms of the host material CMK-3 as well as selected host/guest compounds, recorded with the Autosorb1 for NLDFT analysis. The relative pressure range is shown up to $0.1p/p_0$.

the histogram instead of the pore size distribution the noise occurring in the micropore range can be avoided. Fig. 5d exhibits the pore volume histogram of the CMK-3 calculated with the carbon and silica kernel. The mesopore range show clear differences between the calculations with both kernels. In contrast to the slight broadening of the pore size distribution in the mesopore rangeoccuring by the comparison between the calculation with the silica and the carbon kernel, the histograms resulting from both kernels show a significant difference of approximate 1.5 nm in the maximum of the mesopore range. This effect might be due to the assumed slit pore geometry of the carbon kernel; a carbon kernel with pronounced cylindrical pore geometry does not exist for better comparison.

Fig. 7 shows the pore volume histograms of the host/guest compounds calculated with the NLDFT theory. Additionally the histogram of the pristine CMK-3 is depicted in combination with the histograms of the samples loaded with cobalt. The pore diameters calculated with the BJH method are given in Table 2 (distribution is not shown here). For all compounds, the mesopore diameter decreases after loading with the respective metal oxide combined with a broadening of the diameter distribution. Even after reduction the distribution is nearly the same, except for the samples loaded with manganese, iron and zinc oxide. For these three samples an increase of the adsorbed volume appears.

The micropore region shows a decrease of the adsorbed volume for all samples, caused probably by the filling of the micropores with very small metal oxide particles or micropore blocking. For the samples loaded with manganese, cobalt, copper and zinc, we assume a filling of the micropores whereas for the samples loaded with iron and nickel a pore blocking seems to be existent. This theory is supported by the results of the nitrogen physisorption investigations after reduction, where micropores still occur in the samples loaded with iron and nickel. Caused by the heat treatment a thermal movement of the metal and metal oxide nanoparticles begins and results in a release of the

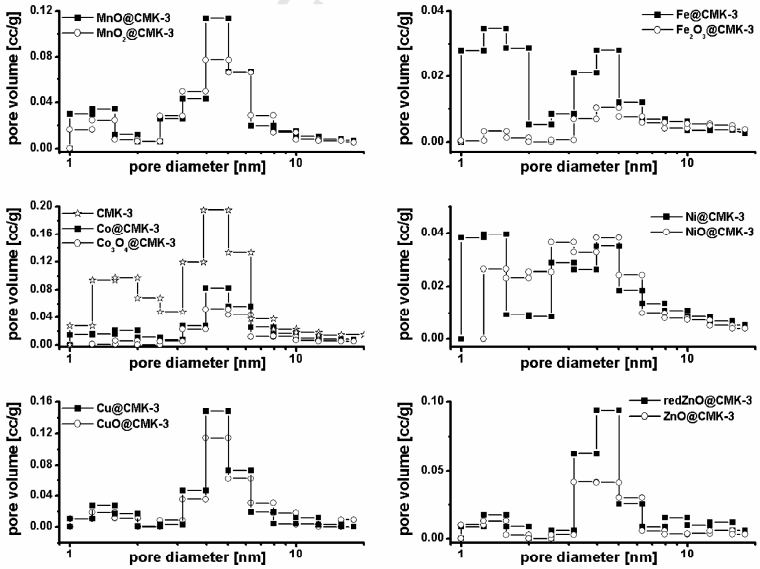

Fig. 7. Pore volume histograms of the host/guest compounds calculated from the adsorption isotherms shown in Fig. 8 by applying the NLDFT method. In the samples loaded with cobalt the pore volume histogram of the host material CMK-3 is embedded.

Please cite this article in press as: Huwe H, Fröba M, Synthesis and characterization of transition metal and metal ..., Carbon (2006), doi:10.1016/j.carbon.2006.09.021

CARBON 4265 ARTICLE IN PRESS No. of Pages 11, Model 5+
13 October 2006 Disk Used

micropore entrance. In case of the samples loaded with manganese, cobalt, copper and zinc no significant changes in the micropore diameter distributions are visible, indicating a reduction of the metal oxides formed inside the micropores.

Nevertheless, all samples show mesoporosity to a higher or lower extent, indicating a coating of the inner surface and a preservation of the host structure even after the reduction process.

4.6. X-ray absorption spectroscopy

X-ray absorption spectroscopy is an important method of gaining knowledge about the local structure not only of metal oxides in host/guest chemistry. This element specific method gives information upon the structure of the metals and metal oxides itself, which is not accessible by methods like PXRD due to their X-ray amorphous character. The recorded absorption spectra are divided into two regions: The first is assigned to the X-ray absorption near-edge structure (XANES) and the second to the extended X-ray absorption fine structure (EXAFS). It should be noted, that the regions overlap. The XANES region is determined by intra-atomic electron transitions and inter-atomic multiple scattering effects. Thus, it is used here as a fingerprint to identify the respective oxide compound. The EXAFS region is the range where single and multiple scattering effects appear. With the knowledge about the respective oxide compound, the EXAFS evaluation is applied to obtain structural information on the metal coordination within the host/guest compounds.

For XANES and EXAFS evaluations of the host/guest compounds as well as of reference materials, spectra at the respective K-edges were recorded. After preparation of the spectra with a conventional data analysis, i.e. energy calibration, background correction and normalization of the edge-jump, XANES and EXAFS analysis were carried out.

The XANES regions of the respective absorption edges for the host/guest compound Mn_xO_y@CMK-3 and bulk materials are shown in Fig. 8a. It can be seen that for every host/guest compound one bulk oxide or bulk metal has the same edge position. The edges of the host/guest compounds themselves are smeared out in contrast to the respective bulk materials. This is an effect that is still known for nanostructured materials [31]. Some of the spectra (e.g. Fe_2O_3, NiO and Cu@CMK-3) show a small pre-edge peak caused by dipole-allowed electronic transitions. The pre-edge peak features are the same compared with the respective bulk materials. A comparison of the energy positions of the absorption edges of the Me_xO_y@CMK-3 to Me@CMK-3 shows the expected shift to lower energies. For example, the energy shift metal oxide minus metal is about 8 eV for $Fe_2O_3 \rightarrow Fe$, 0.8 eV for $NiO \rightarrow Ni$ and 4 eV for $CuO \rightarrow Cu$. These values are in agreement with those reported in literature [48]. With it, the determination of the energy position of the absorption edge and the comparison of the spectra shapes give a first hint on the formed metal oxide compound and the respective reduction products.

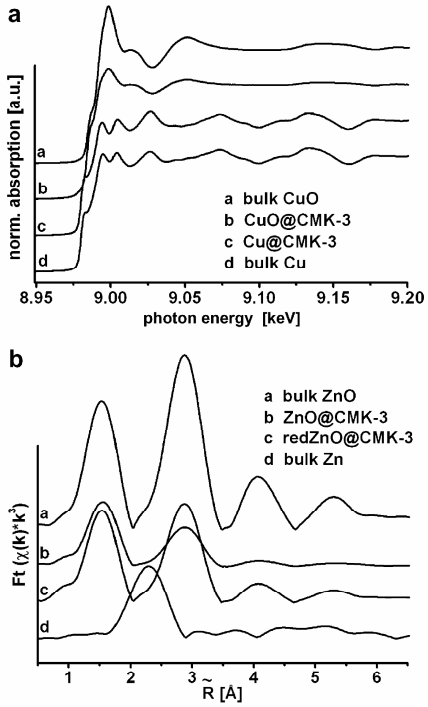

Fig. 8. (a) Normalized metal-K-XANES spectra of the host/guest compound Cu_xO_y@CMK-3 and their respective bulk materials and (b) Fourier transforms (not phase corrected) of a metal K-edge XAFS oscillations of a representative host/guest compound and the corresponding bulk materials. It should be noted, that the XAFS oscillations of the bulk materials are multiplied by a factor <1.

To reveal a better-funded assignment of the bulk oxides and bulk metals to those in the host compounds, a linear combination (LC) XANES fit was carried out for each material. The LC XANES fit permits the quantifying of the species in multiple component mixtures from their fingerprint in the near edge region and here it is used to detect the prevalent species. For that purpose, spectra of all eligible metal and metal oxide compounds were recorded and examined as described above. Afterwards the spectra of each host/guest compound were fitted with the set of each reference compound in order to verify the present chemical structure. Table 3 shows the results of the first LC XANES fit and with it percentage composition of the respective Me_xO_y@CMK-3 and Me@CMK-3 compounds. Reference spectra of metal oxides or metals that are not contained in the sample lead to negative partial concentrations and/or unreasonable energy shifts ($\Delta E > 1$ eV). Their parameters are fixed to zero and the fit was started again to verify the species.

Please cite this article in press as: Huwe H, Fröba M, Synthesis and characterization of transition metal and metal ..., Carbon (2006), doi:10.1016/j.carbon.2006.09.021

CARBON 4265 ARTICLE IN PRESS No. of Pages 11, Model 5+
13 October 2006 Disk Used

Table 3
Results of the first linear combination XANES fit

Sample/r.c.	p.c. (%)	ΔE (eV)	Sample/p.c. (%)	ΔE (eV)
	MnO_2@CMK-3		MnO@CMK-3	
MnO	−44	−0.03	98	0.0007
MnO_2	99	−0.022	-87	14
Mn_2O_3	−0.4	3.1	−3.9	0.03
Mn	−54	0.5	−22	−3.6
	Fe_2O_3@CMK-3		Fe@CMK-3	
Fe_2O_3	98	0.004	−2	−4.3
γ-Fe_2O_3	0.6	1.5	0	3.4
Fe_3O_4	−12	7.3	0	2.2
FeO	−7	0.8	−5	−0.04
Fe	−0.003	2.1	97	−0.014
	Co_3O_4@CMK-3		Co@CMK-3	
CoO	2	−0.083	-2	14
Co	−56	1.6	−33	−0.007
Co_3O_4	99	−2.7	97	3.8
	NiO@CMK-3		Ni@CMK-3	
NiO	97	0.004	−32	2.7
Ni	−7	1.6	98	−0.051
	CuO@CMK-3		Cu@CMK-3	
CuO	94	0.013	1	12
Cu_2O	2	2.8	−65	−8.1
Cu	−7	−7.9	95	0.021
	ZnO@CMK-3		redZnO@CMK-3	
ZnO	97	0.002	99	0.001
Zn	−12	1.8	−0.5	1.7

r.c.: reference compound; p.c.: partial concentration; ΔE: energy shift.

To support the XANES results and gain knowledge about the local structure of the metals, EXAFS evaluations were carried out. For that purpose the prepared and k^3-weighted spectra were Fourier transformed using a Bessel window. Refined structure parameters were obtained by fitting the Fourier transforms in R-space. In general, (1) the amplitude reduction factor was always kept constant to 0.9; (2) the energy shift ΔE_0 was the same for each element and (3) the number of free running parameters in the fits was always significantly smaller than the possible number of independent parameters. A more detailed description of data analysis was recently published by the authors [10]. To prove the accuracy of the refinement and once more the assumed structural agreement with the used theoretical calculated phases, bulk materials were fitted in the same way.

A representative Fourier-transformed and k^3-weighted EXAFS spectra (not phase corrected, mRDF) is shown in Fig. 8b. A first hint on the nano size of the guest compounds is the reduction of the higher metal–metal shells and the missing of further high order shells in the mRDF in contrast to the bulk materials. Please note that for Fig. 8b the amplitudes of the EXAFS oscillations for the reference materials are multiplied by a factor <1 due to the strong reduction in the backscattering amplitude of the host/guest compounds. The radial distribution functions of the reference materials show peaks up to 6 Å but some of them are not appropriate for fitting. In contrast, the peaks of the host/guest compounds are only visible at clearly shorter distances. Reasons are the nanosizing of the particles and a slight structural disorder mentioned above.

Representative structural parameters obtained from the analysis of the spectra are listed in Table 4. The results received conform with those obtained from the respective single crystal data. The agreement of the distances combined with the relatively low coordination numbers compared to those in the bulk materials show the small sizing of the nanoparticles inside the mesoporous carbon network. Because of the loss of the long-range order, it is not possible to fit higher shells of the host/guest compounds as performed for the reference materials. Furthermore, it proves the coating of the inner surfaces of the CMK-3 with a thin layer of metal oxides or the respective metals.

The combination of XANES and EXAFS proved the formation of slightly disordered nanoparticles of 3d transition metals and metal oxides inside the pore system of CMK-3. In the case of ZnO@CMK-3 a structural reordering and for MnO_2@CMK-3 the reduction to MnO@CMK-3 was shown.

Table 4
Representative refined structure parameters extracted from the respective metal K-EXAFS of the host/guest compounds, bulk materials and their reduction products as well as corresponding results extracted from single crystal data (s.c.d.)

Shell	CN	R (Å)	CN	R (Å)	CN	R (Å)
	MnO_2@CMK-3		Bulk MnO_2		s.c.d.	
Mn–O	1.01	1.89	2.00	1.90	2	1.88
Mn–O	3.01	1.92	3.99	1.90	4	1.89
Mn–Mn	1.22	2.94	1.91	2.85	2	2.87
Mn–O	1.39	3.40	3.78	3.30	4	3.34
Mn–Mn	2.98	3.35	7.71	3.46	8	3.42
Mn–O	–	–	3.55	3.46	4	3.43
	Fe_2O_3@CMK-3		Bulk Fe_2O_3		s.c.d.	
Fe–O	2.90	1.91	2.97	1.95	3	1.95
Fe–O	2.85	2.13	2.93	2.10	3	2.11
Fe–Fe	0.74	3.00	0.90	2.88	1	2.90
Fe–Fe	1.35	3.04	2.98	2.94	3	2.97
Fe–Fe	0.53	3.39	3	3.34	3	3.36
Fe–O	2.66	3.40	2.89	3.38	3	3.39
Fe–O	2.84	3.60	2.93	3.61	3	3.59
Fe–Fe	–	–	2.90	3.72	3	3.69
	MnO@CMK-3		Bulk MnO		s.c.d.	
Mn–O	3.45	2.20	6.00	2.23	6	2.22
Mn–Mn	7.32	3.09	11.82	3.16	12	3.14
Mn–O	4.26	3.72	7.42	3.91	8	3.85
Mn–Mn	–	–	3.21	4.46	6	4.44
	Fe@CMK-3		Bulk Fe		s.c.d.	
Fe–Fe	6.32	2.48	8.01	2.50	8	2.49
Fe–Fe	3.81	2.88	5.87	2.87	6	2.87
Fe–Fe	7.73	4.00	11.8	4.02	12	4.06
Fe–Fe	11.0	4.70	21	4.77	24	4.76
Fe–Fe	–	–	7.24	4.88	8	4.97

N: coordination number; *R*: bond length; s.c.d.: single crystal data; for all: Debye-Waller factors below $0.5 * 10^{-2}$ Å^2; $\Delta E_0 < \pm 7.5$ eV; $R < 9.8$; $s_0^2 = 0.9$ fixed.

Please cite this article in press as: Huwe H, Fröba M, Synthesis and characterization of transition metal and metal ..., Carbon (2006), doi:10.1016/j.carbon.2006.09.021

CARBON 4265 ARTICLE IN PRESS No. of Pages 11, Model 5+
13 October 2006 Disk Used

5. Conclusion

Via a wet impregnation/calcination procedure 3d transition metal oxides were synthesized inside the pore system of the mesoporous carbon host CMK-3. This in-situ formation leads to highly dispersed, nanosized metal oxide particles with average diameters determined by the pore diameter of the host. By applying an intra-pore reduction, the transformation from the oxide to the metal form for iron, cobalt, nickel and copper was achieved. As expected, in the case of manganese (IV) oxide, a reduction to manganese (II) oxide and for zinc no transformation was detected. Here, the high temperature treatment under reduction conditions leads to a better structural order. The preservation of the host structure even after reduction was proved by PXRD, nitrogen physisorption, Raman spectroscopy and transmission electron microscopy. Additionally, these methods show the formation of nanostructured guest compounds almost exclusively inside the pore system of the mesoporous carbon. As shown in this study, XAS investigations provide a complete picture of the nature of the hosts. The XANES evaluations reveal the chemical structure of the host, affirmed by EXAFS evaluations. Accordingly, the EXAFS fits substantiate the formation of small slightly disordered nanoparticles.

Acknowledgements

The authors thank HASYLAB@DESY for allocating beamtime, Dr. M. Thommes from Quantachrome Instr., Florida, USA for discussion on the sorption part and M. Güngerich from the Department of Physics at the Philips-University Marburg, Germany, for carrying out the Raman spectroscopic measurements. Financial support by the Fonds der Chemischen Industrie (FCI) is gratefully acknowledged.

Appendix A. Supplementary data

Supplementary data associated with this article can be found, in the online version, at doi:10.1016/j.carbon.2006.09.021.

References

[1] Ryoo R, Joo SH, Jun S. Synthesis of highly ordered carbon molecular sieves via template-mediated structural transformation. J Phys Chem B 1999;103(37):7743–6.
[2] Kruk M, Jaroniec M, Ryoo R, Joo SH. Characterization of ordered mesoporous carbons synthesized using MCM-48 silicas as templates. J Phys Chem B 2000;104(33):7960–8.
[3] Jun S, Joo SH, Ryoo R, Kruk M, Jaroniec M, Liu Z, Ohsuna T, Terasaki O. Synthesis of new, nanoporous carbon with hexagonally ordered mesostructure. J Am Chem Soc 2000;122(43):10712–3.
[4] Ryoo R, Joo SH, Kruk M, Jaroniec M. Ordered mesoporous carbons. Adv Mater 2001;13(9):677–81.
[5] Joo SH, Choi SJ, Kwak J, Liu Z, Terasaki O, Ryoo R. Ordered nanoporous arrays of carbon supporting high dispersions of platinum nanoparticles. Nature 2001;412(6843):169–72.
[6] Shin HJ, Ryoo R, Kruk M, Jaroniec M. Modification of SBA-15 pore connectivity by high-temperature calcination investigated by carbon inverse replication. Chem Commun 2001;4:349–50.
[7] Lee JS, Joo SH, Ryoo R. Synthesis of mesoporous silicas of controlled pore wall thickness and their replication to ordered nanoporous carbons with various pore diameters. J Am Chem Soc 2002;124(7):1156–7.
[8] Solovyov LA, Shmakov AN, Zaikovskii VI, Joo SH, Ryoo R. Detailed structure of the hexagonally packed mesostructured carbon material CMK-3. Carbon 2002;40(13):2477–81.
[9] Darmstadt H, Roy C, Kaliaguine S, Choi SJ, Ryoo R. Surface chemistry of ordered mesoporous carbons. Carbon 2002;40(14):2673–83.
[10] Huwe H, Fröba M. Multiple-scattering extended X-ray absorption fine structure analysis on nanostructured iron(iii) oxide in the pore system of mesoporous carbon CMK-1. Anal Bioanal Chem 2006;384:817–26.
[11] Roggenbuck J, Tiemann M. Ordered mesoporous magnesium oxide with high thermal stability synthesized by exotemplating using CMK-3 carbon. J Am Chem Soc 2005;127:1096–7.
[12] Minchev C, Huwe H, Tsoncheva C, Paneva D, Dimitrov M, Mitov I, Fröba M. Iron oxide modified mesoporous carbons: Physicochemical and catalytic study. Microporous Mesoporous Mater 2005;81:333–41.
[13] Fuertes AB. Synthesis of ordered nanoporous carbons of tunable mesopore size by templating SBA-15 silica materials. Microporous Mesoporous Mater 2004;67:273–81.
[14] Darmstadt H, Roy C, Kaliaguine S, Joo SH, Ryoo R. Pore structure and graphitic surface nature of ordered mesoporous carbons probed by low-pressure nitrogen adsorption. Microporous Mesoporous Mater 2003;60(1-3):139–49.
[15] Ryoo R, Joo SH. Nanostructured carbon materials synthesized from mesoporous silica crystals by replication. Stud Surf Sci Catal 2004;148:241–60.
[16] Lee J, Yoon S, Hyeon T, Oh SM, Kim KB. Synthesis of a new mesoporous carbon and its application to electrochemical double-layer capacitors. Chem Commun 1999:2177–8.
[17] Mariwala RK, Acharya M, Foley HC. Adsorption of halocarbons on a carbon molecular sieve. J Microporous Mater 1998;22(2):281–8.
[18] Kyotani T. Control of pore structure in carbon. Carbon 2000;38(2):269–86.
[19] Tamai H, Kakii T, Hirota Y, Kumamoto T, Yasuda H. Synthesis of extremely large mesoporous activated carbon and its unique adsorption for giant molecules. Chem Mater 1996;8(2):454–62.
[20] Lu W, Chung DDL. Mesoporous activated carbon filaments. Carbon 1997;35(3):427–30.
[21] Hu Z, Srinivasan MP, Ni Y. Preparation of mesoporous high-surface-area activated carbon. Adv Mater 2000;12:62–3.
[22] Han S, Sohn K, Hyeon T. Fabrication of new nanoporous carbons through silica templates and their application to the adsorption of bulky dyes. Chem Mater 2000;12:3337–41.
[23] Kawashima D, Aihara T, Kobayashi Y, Kyotani T, Tomita A. Preparation of mesoporous carbon from organic polymer/silica nanocomposite. Chem Mater 2000;12(11):3397–401.
[24] Kruk M, Jaroniec M, Joo SH, Ryoo R. Characterization of regular and plugged SBA-15 silicas by using adsorption and inverse carbon replication, and explanation of the plug formation mechanism. J Phys Chem B 2003;107(10):2205–13.
[25] Zhou H, Zhu S, Hibino M, Honma I. Electrochemical capacitance of self-ordered mesoporous carbon. J Power Sources 2003;122:219–23.
[26] Zhou H, Zhu S, Hibino M, Honma I, Ichihara M. Lithium storage in ordered mesoporous carbon (CMK-3) with high reversible specific energy capacity and good cycling performance. Adv Mater 2003;15(24):2107–11.
[27] Tang Q, Zhang Q, Wang P, Wang Y, Wan H. Characterizations of cobalt oxide nanoparticles within faujasite zeolites and the formation of metallic cobalt. Chem Mater 2004;16:1967–76.
[28] Köhn R, Paneva D, Dimitrov M, Tsoncheva T, Mitov I, Minchev C, Fröba M. Studies on the state of iron oxide nanoparticles in MCM-41

Please cite this article in press as: Huwe H, Fröba M, Synthesis and characterization of transition metal and metal ..., Carbon (2006), doi:10.1016/j.carbon.2006.09.021

CARBON 4265 ARTICLE IN PRESS No. of Pages 11, Model 5+
13 October 2006 Disk Used

and MCM-48 Silica materials. Microporous Mesoporous Mater 2003;63:125–37.
[29] Köhn R, Fröba M. Nanoparticles of 3 d transition metal oxides in mesoporous MCM-48 silica host structures: Synthesis and characterization. Catalysis Today 2001;68:227–63.
[30] Minchev C, Huwe H, Tsoncheva T, Dimitrov M, Paneva D, Mitov I, Fröba M. Effect of Support Pore Size on the Structural and Catalytic Properties of Iron and Cobalt Oxides modified SBA-1, SBA-15, MCM-41 and MCM-48 Silica Materials. Proc. 14th Internat. Zeolite Conf., 2004, p. 841, ISBN: 0-958-46636-X.
[31] Fröba M, Köhn R, Bouffaud G, Richard O, van Tendeloo G. Fe_2O_3 nanoparticles within mesoporous MCM-48 silica: In situ formation and characterization. Chem Mater 1999;11:2858–65.
[32] Brieler F, Grundmann P, Fröba M, Chen L, Klar PJ, Heimbrodt W, et al. Size dependence of the magnetic and optical properties of $Cd_{1-x}Mn_xS$ nanostructures confined in mesoporous silica. J Am Chem Soc 2005;17:795–803.
[33] Huwe H, Fröba M. Iron (III) oxide nanoparticles within the pore system of mesoporous carbon CMK-1: intra-pore synthesis and characterization. Microporous Mesoporous Mater 2003;60:151–8.
[34] Zhao D, Feng J, Huo Q, Melosh N, Fredrickson GH, Chmelka BF, Stucky GD. Triblock copolymer syntheses of mesoporous silica with periodic 50 to 300 angstrom pores. Science 1998;279:548–52.
[35] Zhao D, Huo Q, Feng J, Chmelka BF, Stucky GD. Nonionic triblock and star diblock copolymer and oligomeric surfactant syntheses of highly ordered, hydrothermally stable, mesoporous silica structures. J Am Chem Soc 1998;120:6024–36.
[36] Brunauer S, Emmet PH, Teller E. Adsorption of gases in multimolecular layers. J Am Chem Soc 1938;60:309–19.
[37] Barrett EP, Joyner LG, Halenda PP. The determination of pore volume and area distributions in porous substances: 1. Computations from nitrogen isotherms. J Am Chem Soc 1951;73:373–80.
[38] Sonwane CG, Bhatia SK, Characterization of Pore Size Distributions of Mesoporous Materials from Adsorption Isotherms. J Phys Chem B 2000;104:9099–110.
[39] Neimark AV, Ravikovitch PI. Capillary condensation in MMS and pore structure characterization. Microporous Mesoporous Mater 2001;44-45:697–707.
[40] Vishnyakov A, Ravikovitch PI, Neimark A. Molecular level models for CO_2 sorption in nanopores. Langmuir 1999;15:8736–42.
[41] Rouquerol F, Rouquerol J, Sing K. Adsorption by powders & porous solids. Academic Press; 1999.
[42] Ravikovitch PI, Wei D, Haller GL, Neimark AV. Evaluation of pore structure parameters of MCM-41 catalyst supports and catalysts by means of nitrogen and argon adsorption. J Phys Chem B 1997;101:3671–9.
[43] Thommes M. Pore Size Analysis by Gas Adsorption. Part I: Aspects of the Application of Density Functional Theory (DFT) and Monte Carlo Simulation (MC) for Micro/Mesopore Size Analysis. Powder Tech Note 31, Fa Quantachrome Instruments, Florida, USA.
[44] Ressler T. WinXAS: a program for X-ray absorption spectroscopy data analysis under MS-Windows. J Synchr Rad 1998;5:118–22.
[45] Ankudinov AL, Bouldin CE, Rehr JJ, Sims J, Hung H. Parallel calculation of electron multiple scattering using Lanczos algorithms. Phys Rev B 2002;65:104107–17.
[46] Dresselhaus MS, Pimenta MA, Eklund PC, Dresselhaus G. Raman scattering in fullerenes and related carbon-based materials. In: Weber WH, Merlin R, editors. Raman Scattering in Materials Science. Berlin-Heidelberg: Springer-Verlag; 2000. p. 314. Chapter 8.
[47] Sing KSW, Everett DH, Haul RAW, Moscou L, Pierotti RA, Rouquerol J, Siemieniewska T. Reporting physisorption data for gas/solid systems with special reference to the determination of surface area and porosity. Pure Appl Chem 1985;57(4):603–19.
[48] Grunes LA. Study of the K edges of 3d metals in pure and oxide form by X-ray absorption spectroscopy. Phys Rev B 1983;27(4):2111–31.

Please cite this article in press as: Huwe H, Fröba M, Synthesis and characterization of transition metal and metal ..., Carbon (2006), doi:10.1016/j.carbon.2006.09.021

Supplementary data to V2.7 (Appendix A)

Table S1: Refined structure parameters extracted from the respective metal-K EXAFS of the host/guest compounds and bulk materials as well as corresponding results extracted from single crystal data (s.c.d.).

Table S2: Refined structure parameters extracted from the metal-K EXAFS of the reduced host/guest compounds and reduced bulk materials as well as corresponding results extracted from single crystal data.

Figure S1: Representative high resolution TEM photographs of (a) the pristine CMK-3 host structure, (b) CuO@CMK-3, (c) Ni@CMK-3, (d) MnO@CMK-3, (e) redZn@CMK-3 and (f) Co@CMK-3.

Figure S2: Liquid nitrogen isotherms of the respective host/guest compounds.

Figure S3: Normalized metal-K-XANES spectra of the host/guest compounds and their respective bulk materials.

Figure S4: Fourier transforms (not phase corrected) of the respective metal K-edge XAFS oscillations of the host/guest compound and the corresponding bulk materials. It should be noted, that the XAFS oscillations of the bulk materials are multiplied by a factor < 1.

shell	CN	R [Å]	CN	R [Å]	CN	R [Å]
	MnO_2@CMK-3		**bulk MnO_2**		**s.c.d.**	
Mn-O	1.01	1.89	2.00	1.90	2	1.88
Mn-O	3.01	1.92	3.99	1.90	4	1.89
Mn-Mn	1.22	2.94	1.91	2.85	2	2.87
Mn-O	1.39	3.40	3.78	3.30	4	3.34
Mn-Mn	2.98	3.35	7.71	3.46	8	3.42
Mn-O	-	-	3.55	3.46	4	3.43
	Fe_2O_3@CMK-3		**bulk Fe_2O_3**		**s.c.d.**	
Fe-O	2.90	1.91	2.97	1.95	3	1.95
Fe-O	2.85	2.13	2.93	2.10	3	2.11
Fe-Fe	0.74	3.00	0.90	2.88	1	2.90
Fe-Fe	1.35	3.04	2.98	2.94	3	2.97
Fe-Fe	0.53	3.39	3	3.34	3	3.36
Fe-O	2.66	3.40	2.89	3.38	3	3.39
Fe-O	2.84	3.60	2.93	3.61	3	3.59
Fe-Fe	-	-	2.90	3.72	3	3.69
	Co_3O_4@CMK-3		**bulk Co_3O_4**		**s.c.d.**	
Co-O	4.44	1.90	5.97	1.91	6	1.91
Co-Co	3.25	2.80	4.71	2.86	6	2.85
Co-O	1.09	3.07	1.22	3.27	2	3.30
Co-Co	1.99	3.27	2.00	3.31	6	3.35
Co-O	-	-	1.84	3.50	6	3.56
	NiO@CMK-3		**bulk NiO**		**s.c.d.**	
Ni-O	5.11	2.01	5.89	2.09	6	2.08
Ni-Ni	8.88	2.88	11.81	2.93	12	2.95
Ni-O	4.23	3.42	7.55	3.55	8	3.61
Ni-Ni	2.01	3.87	4.71	3.99	6	4.17
	CuO@CMK-3		**bulk CuO**		**s.c.d.**	
Cu-O	0.88	1.97	1.98	1.96	2	1.95
Cu-O	0.78	1.97	1.99	1.96	2	1.96
Cu-O	0.64	2.74	1.97	2.77	2	2.78
Cu-Cu	1.45	2.87	3.73	2.91	4	2.91
Cu-Cu	1.39	3.00	3.71	3.09	4	3.08
Cu-Cu	-	-	1.43	3.25	2	3.17
	ZnO@CMK-3		**bulk ZnO**		**s.c.d.**	
Zn-O	0.55	1.77	1.00	1.81	1	1.79
Zn-O	2.01	2.32	2.34	2.04	3	2.04
Zn-Zn	2.65	3.44	5.82	3.23	6	3.21
Zn-Zn	2.87	3.45	4.75	3.30	6	3.25
Zn-O	-	-	4.79	3.74	6	3.71
Zn-Zn	-	-	4.21	4.50	6	4.56

N: coordination number; R: bond length; s.c.d.: single crystal data; for all: Debye-Waller factors below $0.5*10^{-2}$ Å^2; $\Delta E_0 < \pm$ 7.5 eV; R < 9.8; $s_0^2 = 0.9$ fixed.

shell	CN	R [Å]	CN	R [Å]	CN	R [Å]
	MnO@CMK-3		**bulk MnO**		**s.c.d.**	
Mn-O	3.45	2.20	6.00	2.23	6	2.22
Mn-Mn	7.32	3.09	11.82	3.16	12	3.14
Mn-O	4.26	3.72	7.42	3.91	8	3.85
Mn-Mn	-	-	3.21	4.46	6	4.44
	Fe@CMK-3		**bulk Fe**		**s.c.d.**	
Fe-Fe	6.32	2.48	8.01	2.50	8	2.49
Fe-Fe	3.81	2.88	5.87	2.87	6	2.87
Fe-Fe	7.73	4.00	11.8	4.02	12	4.06
Fe-Fe	11.0	4.70	21	4.77	24	4.76
Fe-Fe	-	-	7.24	4.88	8	4.97
	Co@CMK-3		**bulk Co**		**s.c.d.**	
Co-Co	3.46	2.48	5.98	2.46	6	2.50
Co-Co	2.21	2.53	5.89	2.21	6	2.51
Co-Co	3.01	3.50	5.73	3.51	6	3.54
Co-Co	1.09	4.00	1.51	4.01	2	4.07
Co-Co	-	-	6.66	4.30	12	4.34
	Ni@CMK-3		**bulk Ni**		**s.c.d.**	
Ni-Ni	9.34	2.48	11.8	2.50	12	2.49
Ni-Ni	4.44	3.50	6.01	3.54	6	3.52
Ni-Ni	11.39	4.27	22.07	4.28	24	4.31
Ni-Ni	-	-	9.56	4.84	12	4.98
	Cu@CMK-3		**bulk Cu**		**s.c.d.**	
Cu-Cu	8.54	2.55	12	2.55	12	2.56
Cu-Cu	2.92	3.55	5.98	3.60	6	3.61
Cu-Cu	-	-	16.3	4.32	24	4.43
	redZnO@CMK-3		**bulk ZnO**		**s.c.d.**	
Zn-O	0.56	1.81	0.99	1.81	1	1.79
Zn-O	2.11	2.05	2.86	2.04	3	2.04
Zn-Zn	3.21	3.22	5.76	3.23	6	3.21
Zn-Zn	3.03	3.17	5.34	3.30	6	3.25
Zn-O	3.00	3.51	5.44	3.74	6	3.71
Zn-Zn	-	-	5.65	4.44	6	4.56

N: coordination number; R: bond length; s.c.d.: single crystal data; for all: Debye-Waller factor below $0.5*10^{-2}$ Å^2; $\Delta E_0 < \pm$ 7.5 eV; R < 9.8; $s_0^2 = 0.9$ fixed

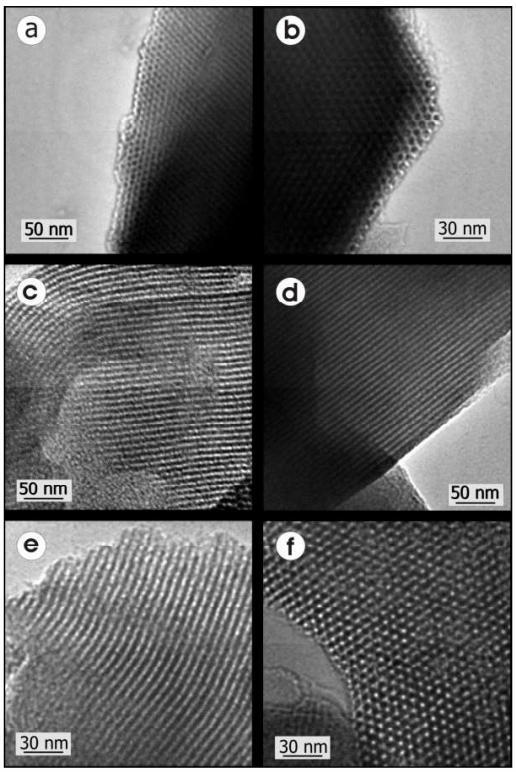

Figure S1: Representative high resolution TEM photographs of (a) the pristine CMK-3 host structure, (b) CuO@CMK-3, (c) Ni@CMK-3, (d) MnO@CMK-3, (e) redZn@CMK-3 and (f) Co@CMK-3.

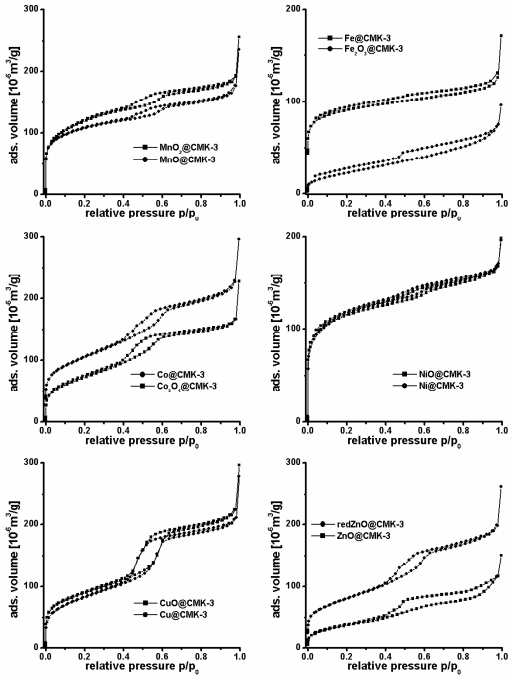

Figure S2: Liquid nitrogen isotherms of the respective host/guest compounds.

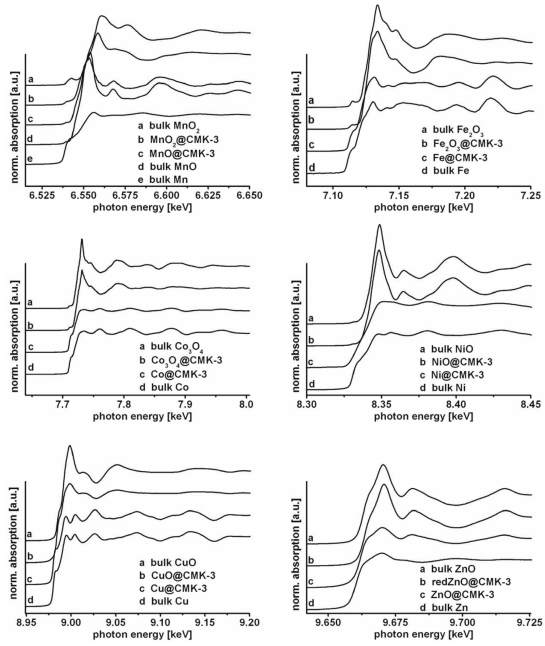

Figure S3: Normalized metal-K-XANES spectra of the host/guest compounds and their respective bulk materials.

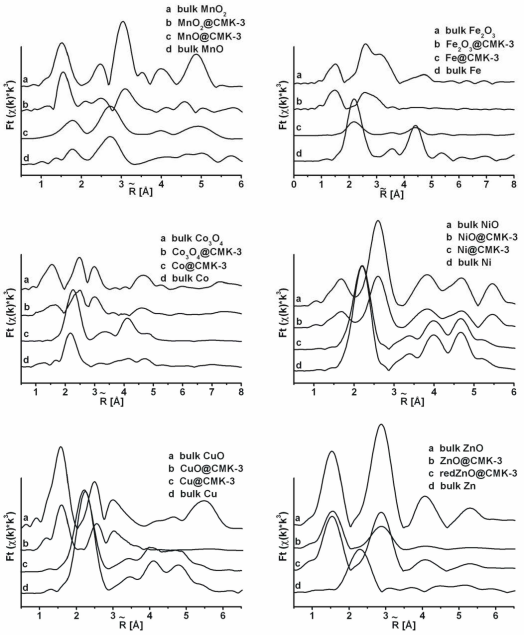

Figure S4: Fourier transforms (not phase corrected) of the respective metal K-edge XAFS oscillations of the host/guest compound and the corresponding bulk materials. It should be noted, that the XAFS oscillations of the bulk materials are multiplied by a factor < 1.

Intra pore reduction of nanostructured α-Fe_2O_3 within the pore system of mesoporous carbon – a comprehensive study

Holger Huwe and Michael Fröba*

Institute of Inorganic and Analytical Chemistry, Justus Liebig University Giessen
Heinrich-Buff-Ring 58, D-35392 Giessen, Germany

Abstract

For the first time fundamental research of the reduction behavior of nanostructured iron(III) oxide incorporated in mesoporous carbon will be presented in this study. The first part will describe the formation of the individual reduction phases in detail, taking into account the composition of reduction gas as well as the influence of the heating rate. These results are compared to results gained from bulk iron(III) oxide. In the second part, the means of synthesizing nanostructured pure Fe_3O_4 and Fe^0 as well as a high amount of FeO in the pore system of mesoporous carbons is shown. This is achieved by the elegant method of an intra-pore reduction with a constantly kept temperature. The findings of the fundamental research on nanoscaled iron(III) oxides pursued, will serve for a better understanding of reduction behavior of the complex system haematite → magnetite → wüstite → iron.

Keywords: nanostructured iron oxide; mesoporous carbon; reduction; host structure.

Introduction

The reduction behavior of 3d metal oxides has been investigated for over a century. The system iron oxide/iron haematite → magnetite → wüstite → iron is of particular significance. It often stands as a model system for the multitude of transition metal oxides and numerous experiments and extensive theoretical investigations on this subject.[1-22] It is applied for instance in catalysis, fuel cells and recently as storage site for hydrogen, which is still in progress.[2,9,12,14,15,18]

First investigations concerning the properties of the different iron oxides such as crystal structure but also first results of the reduction behavior of different iron oxides were published in the early nineteen twenties by Pauling and Hendricks.[22] The aim of numerous following experiments was obtaining a better understanding of the properties of iron oxide in order to study its reduction behaviour.[5,19-26]

During the reduction process, the iron oxides are transformed from the haematite structure, which is isostructural with corundum, over an inverse spinel structure (magnetite) to a defect sodium chloride structure (wüstite) and ends with the body-centered cubic (bcc) iron.

*Corresponding author. Fax ; +49-641-9934-109.
E-mail address: Michael.Froeba@anorg.chemie.uni-giessen.de (M. Fröba)

The proceeding reaction mechanisms are sensitive to all reduction parameters and thus, it is not surprising, that there are often discrepancies between the statements of various investigators.[27] Complete reduction studies on bulk haematite with hydrogen in water were carried out by St. John et al.[28] in 1984 and Rau et al. in 1987.[29] First experiments involving small iron oxide particles (50 - 800 µm) were carried out by Hayes and Grieveson in 1981[30] and by El-Tabirou et al. in 1988.[31] During these investigations they showed that the reduction process is dependent on the reaction temperature and the concentration of the reduction gas, which was CO in their case.

A new synthesis approach to nanosized particles was given with the introduction of host/guest chemistry. Particles synthesized inside the pore systems of mesoporous materials often reveal different properties than the respective bulk materials caused by the size limitation due to the pore size of the host material, e.g. silica.[26,32] Even in the host/guest chemistry the system of the iron oxides/iron was a field of interest. The influence of pore sizes, loadings and the catalytic system of Fe_2O_3@SBA-15 and Fe_2O_3@CMK-3 on their catalytic activities compared to the catalytic activity of bulk haematite has been investigated in several studies.[10-12,14-16,33-38]

The introduction of mesoporous carbons with ordered pore systems in 1999 by Ryoo et al.

established a new field of host/guest chemistry.[39,40] The advantage of mesoporous carbons compared to silica is the reducing property of the carbon framework. Again the focus was set on the system α- Fe_2O_3 → Fe_3O_4 → $Fe_{1-x}O$ → Fe^0 because the reduced iron oxide species remain unchanged under circumstances such as storing at low temperatures or inert atmosphere due to the carbeneous host material. In contrast, the application of mesoporous silica as a host material reveals reoxidation caused by oxygen of the silica framework, which hampers the synthesis of particular iron oxides in their pore systems. With these new carbon-like representatives of mesoporous substances, it is now possible to intensively investigate the host/guest system Fe_2O_3@CMK-n with respect to its reduction behaviour.[40-52]

Another possibility of investigating the reduction behavior of the system Fe_2O_3@CMK-n is an in situ method which is described by the authors.[37,38] As a result of the in situ experiments, the formation of each reduction product (α- Fe_2O_3, Fe_3O_4, $Fe_{1-x}O$, Fe^0) is dependent on the reduction gas composition, heating rate, temperature and the particle size (limited by the pore size of the carbon host material). For example, the here reported intra pore reduction method is a proper way to synthesize pure nanostructured magnetite. Given this prerequisite, it is furthermore possible (with some restrictions of course) to tune the portions of the respective iron phases in a desired way.

The present work undertakes a comprehensive study of the reduction behavior of nanosized iron(III) oxides accompanied in mesoporous carbons under various conditions. We believe that these are the first experiments on nanostructured iron(III) oxides of this kind.

Synthesis

Synthesis of mesoporous carbon. The synthesis of the host structures CMK-1 and CMK-3 was carried out according to the procedure reported in literature.[39,41] In general, a silica host matrix (MCM-48 respective SBA-15) was infiltrated twice with sucrose. After carbonization at 1100 K in vacuum the silica framework was destroyed and removed by hydrofluoric acid to obtain the pristine host structures.

Synthesis of the host/guest compounds. The incorporations of the iron(III) oxides inside the pore systems of the mesoporous carbon host structures were carried out applying the wet impregnation method. In general, a 0.5 molar solution of iron(III) nitrate in ethanol was stirred with the host material. A separation of the solution by centrifugation and gentle drying at room temperature followed. Afterwards the transformation from the nitrate into the oxide was conducted by thermal treatment at 300 K in an air stream. This impregnation cycle was repeated up to three times in order to obtain two different amounts of iron(III) oxide loading. Further on they are signed as single and triple allocations. For more details of the impregnation procedure see references.[33,34]

Synthesis of reference compounds. In order to obtain the respective reference compounds, iron(III) nitrate was treated the same way as described for the synthesis of the host/guest compounds. After transformation to iron(III) oxide it was reduced as specified in the next chapter. The formation of the respective bulk phases was confirmed with powder X-ray diffraction. Additionally, commercially available iron oxides were used.

Temperature programmed reduction (tpr). The reductions were carried out with a ChemBET3000 (Quantachrome) operating with two thermal conductivity detectors (tcd, oxygen detection). For gas mixing a Linear Mass Flow Controller (Quantachrome) was used. The gas flow rate was 25 cm^3/min for all experiments.

The temperature reduced reductions (tpr) were carried out running three different temperature ramps (1, 5 and 10 K/min), three different reduction gas mixtures (1, 5 and 50 % H_2 in N_2) and two amounts of weighted samples (15 and 30 mg). Usually 30 mg of the samples were used for the investigations. For experiments carried out in order to obtain dependence between the sample weight and the reduction behavior 15 mg and 30 mg of each sample were used.

During the reduction procedure samples were taken in intervals of 25 K in the range from 300 up to 1150 K. The quenching of the reduction is the trickiest part. During the reduction one of two wüstite-like phases occurs. They are the stoichiometric FeO or the non-stoichiometric $Fe_{1-x}O$ phases. Regrettably, the formation of the phases during the reduction is not controllable. As far as we know there is no way to stabilize the stoichiometric phase at room temperature in air; it dissociates visible to Fe_2O_3 and Fe^0. For this reason, these samples have no explanatory power and the reduction was repeated. In order to stabilize the non-stoichiometric phase at room temperature several investigations were carried out. Here the samples were cooled down rapidly in liquid nitrogen combined with a changing of the atmosphere to pure nitrogen. The samples are stable over several weeks under nitrogen atmosphere at 250 K.

Furthermore, reductions at defined temperatures (573, 623, 673, 723, 873 K) were carried out using 5 % hydrogen in nitrogen with a heating rate of 20 K/min for all experiments. The reduction was conducted until the tcd signal rises to zero. At this point, the samples were cooled down rapidly in liquid nitrogen combined with a changing of the atmosphere to pure nitrogen. To avoid a reduction or oxidation of the samples, they were stored under nitrogen atmosphere at 250 K.

Characterization

The (i) formation of the iron(III) oxides almost exclusively inside the pore systems of the host structures, the (ii) preservation of the host structures during the impregnation cycles, the (iii) preservation of the host/guest compounds after reduction and (iv) the remaining guest species inside the pore system after the reduction (thermal movement) was confirmed with powder X-ray diffraction, liquid nitrogen physisorption, transmission electron microscopy, Raman spectroscopy, infrared spectroscopy and X-ray absorption fine structure analysis, respectively. An extensive description of the usage of this canon of methods is given elsewhere.[33-35]

To examine the reduction products X-ray absorption spectroscopic measurements (XAFS) were carried out at the storage ring DORIS III (HASYLAB@DESY, Hamburg, Germany). The used XAFS beam line A1 was equipped with a Si(111) double-crystal monochromator. The Fe-K edge spectra were taken at liquid nitrogen temperature (77 K). All spectra were recorded in fluorescence mode up to four times to improve the signal to noise ratio after summation. The samples were measured as pressed polyethylene pills in inert atmosphere. For further data analysis the program WinXAS3.2 was used.[53]

After a common data analysis (e.g. energy calibration, background correction, normalization) a linear combination XANES fit procedure was applied as described in reference [34]. With that the partitions of the reduction products were determined. As reference materials common available compounds as well as synthesized ones were taken.

For extended X-ray absorption fine structure (EXAFS) analysis the data were first prepared in the common way (e.g. energy calibration, Fourier transformation). Then the theoretical calculations of the phase shifts were calculated using the program FEFF8 embedded in WinXAS.[53,54] A detailed description of EXAFS data analysis is given in reference [35].

Results and Discussion

Results and discussion of the temperature independent reductions. In this chapter we will show the influence of different parameters (such as heating rate, amount of hydrogen, allocation with α-Fe_2O_3) on the reduction profile as well as the development of the specific iron oxide phases. A typical reduction profile of 30 mg host/guest compound is depicted in Figure 1. Regarding the tpr curve the first maximum is ascribed to the transition of α-Fe_2O_3 to Fe_3O_4, the second to the transition of Fe_3O_4 to $Fe_{1-x}O$ and the third is equivalent to the reduction of $Fe_{1-x}O$ to metallic iron. Figure 1 also includes the development of the specific phases. The correlation of the maximum of the Fe_3O_4-phase (□) with the maximum of the reduction profile can clearly be observed in this Figure. The second maximum in the reduction profile corresponds to the position where the following conditions are fulfilled: the sum of the amounts of increase of $Fe_{1-x}O$ (■) and the decrease of Fe_3O_4 (□) is maximal. The last maximum corresponds to the point with the highest possible amounts of formed $Fe_{1-x}O$ (■). At this point nearly all $Fe_{1-x}O$ is reduced and the tpr signal decreases afterwards.

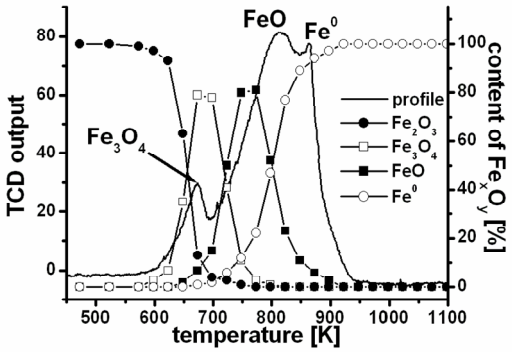

***Figure 1:** Typical reduction profile for the reduction of Fe_2O_3CMK-1 with the evaluation of the respective iron oxide phases. The heating rate was 5 K/min and the amount of hydrogen 5 %.*

In the following part, reduction profiles and the development of the corresponding phases will be predominantly discussed for the sake of a better illustration. The influence of the individual parameters will be shown on the example of the host/guest compound Fe_2O_3@CMK-3, although this analysis was also carried out on Fe_2O_3@CMK-1. However, as will be shown later, the results are comparable and therefore we shall refrain from a presentation and discussion thereon. It is taken for granted that the analytical study is reproducible and representative. The minimal amount of hydrogen used was enough to reduce the iron oxide completely within a couple of seconds. This assures that the effects discussed later will not be distorted or falsified by lack of reduction gas.

Reduction from Fe_2O_3@CMK-n with different parameters. In this chapter the influence of the heating rate and the amount of hydrogen upon the reduction behavior will be examined more closely. Figure 2 shows the profile of the reduction from Fe_2O_3@CMK-3 in dependence of three different heating rates and hydrogen fractions respectively. In order to figure out the different effects during the reduction of the single samples the correlations between the heating rate, the hydrogen concentration, the maximal content of each iron oxide phase, the temperature and the reduction intervals were extracted from the formation of each iron oxide shown in Figure 3 and summarized in 4.

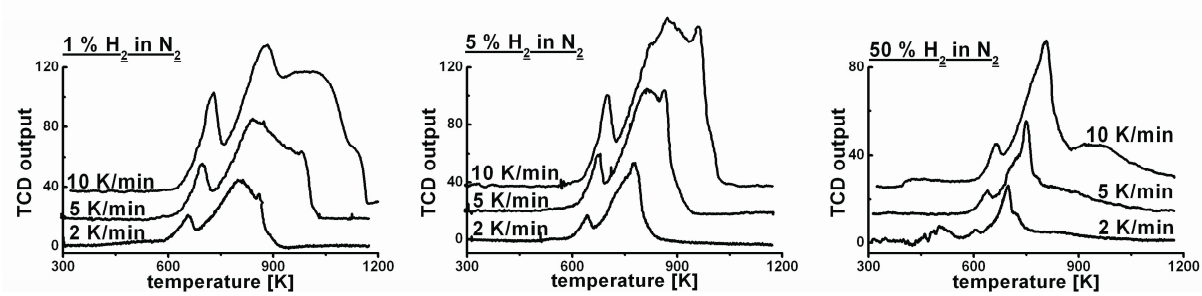

Figure 2: Reduction profiles of the reduction from Fe_2O_3@CMK-3 in dependence of three different heating rates and hydrogen fractions respectively.

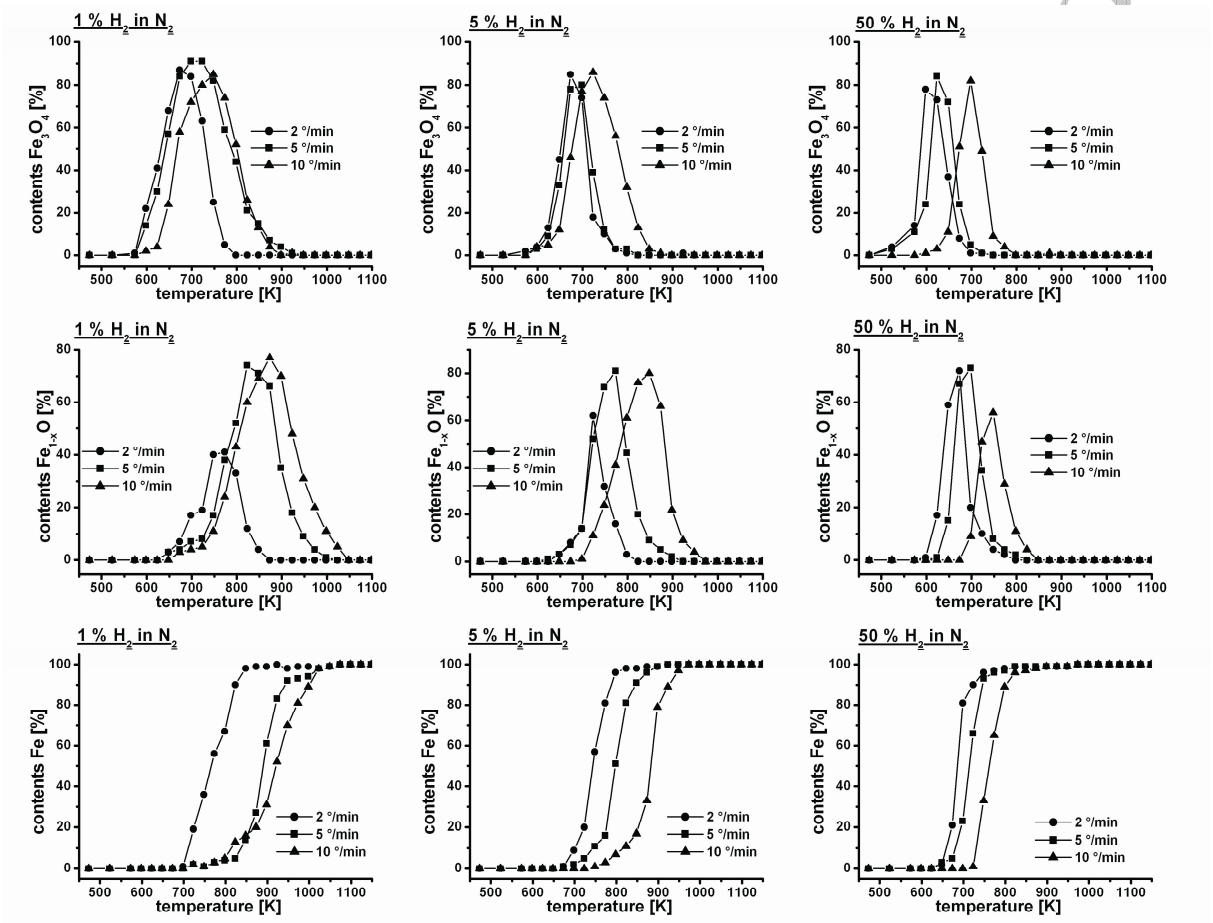

Figure 3: Evaluation of the Fe_3O4-phase (top), the $Fe_{1-x}O$-phase (middle) and the Fe-phase (bottom) from the reduction of Fe_2O_3@CMK-3 in dependence of three different heating rates and hydrogen fractions respectively.

Figure 4a shows the correlation between the maximal Fe_3O_4 content and the heating rate for each hydrogen concentration. Figure 4b depicts the temperature of the magnetite concentration maximum in dependence of the heating rate and the hydrogen concentration. Figure 4c presents the correlation between the reduction interval ΔT [K] (full width half maximum (FWHM)) respective Figure 4d the reduction interval Δt [min] and the heating rate for each hydrogen concentration.

From Figure 4a one can conclude that the differences between the magnetite contents dependent on the hydrogen concentration and the heating rate are quite low. The magnetite content is above 80 % in every investigated sample. The highest magnetite contents are obtained for the lowest hydrogen concentration. This effect can be explained by the slower reduction rate due to the lower hydrogen concentration and thus, to a lower reaction rate for following the reduction from Fe_3O_4 to $Fe_{1-x}O$. An increase of the heating rate from 2 to 5 K/min leads to a further increase of the magnetite content for the sample reduced with only 1 % hydrogen in nitrogen. A further increase of the heating rate to 10 K/min leads to a reduced concentration of magnetite due to the higher concentration of wüstite in all measured samples.

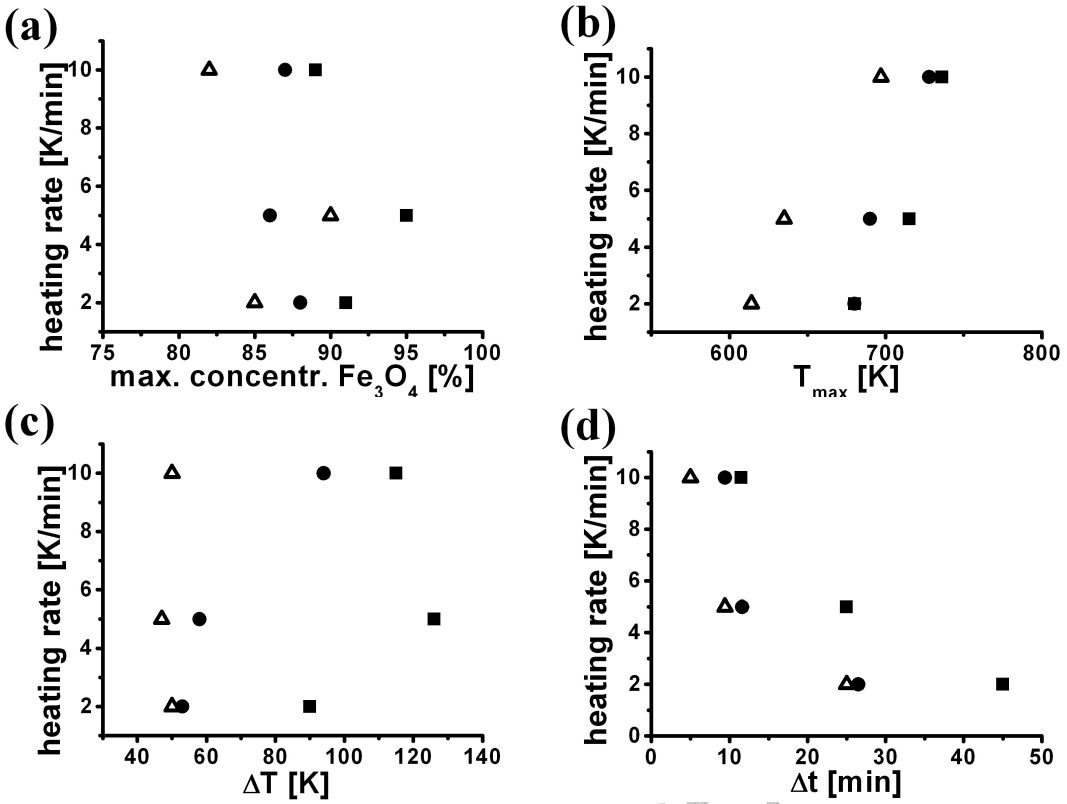

Figure 4: Correlation between (a) the maximal Fe_3O_4 content, (b) the temperature of the Fe_3O_4 concentration maximum, (c) the reduction interval ΔT in [K] (full width half maximum (FWHM)) and (d) the reduction interval Δt in [min] and the heating rate for each hydrogen concentration from the reduction of Fe_2O_3@CMK-3. Legend: (□) 50 % H_2; (●) 5 % H_2; (■) 1 % H_2 in N_2.

Linear correlations between the heating rate and the temperature T_{max} (temperature at the point of the highest magnetite concentration) in the measured region can clearly be concluded from Figure 4b for each hydrogen concentration. The temperatures where the maximal magnetite contents were obtained is nearly the same for the samples reduced with 1 and 5 % hydrogen starting at 680 K for a heating rate of 2 K/min increasing up to 730 K for a heating rate of 10 K/min. The influence of the hydrogen concentration on the temperature T_{max} is significant. The maximum content is reached at lower temperatures that can be explained by a faster reduction rate due to the high hydrogen concentration. The influence of the hydrogen concentration and the heating rate on the reduction interval (FWHM, ΔT) does not follow such a clear trend. Thus, a careful interpretation of Figure 4c should be carried out. First, the influence of the hydrogen concentration on the reduction interval is obvious. Due to the low concentration of 1 % hydrogen in the reduction gas the reaction takes more time which leads to an increase of the reduction interval. The reduction interval seems to increase with increasing heating rate for the hydrogen concentrations of 1 and 5 % but no clear linear correlation between ΔT and the heating rate can be figured out. For the increase of the reduction interval one should consider the time of the measurement additional to the temperature, which has not been mentioned yet. The reduction interval ΔT is given by the difference between the starting temperature T_S and the finishing temperature T_F. These temperatures are reached after different periods of time due to the different heating rates of 2, 5 and 10 K/min. Due to the faster process at a heating rate of 10 K/min the reduction interval increases because the system still needs time for equilibrating. Thus, the consideration of the reduction intervals is in this case quite complex. The highest hydrogen concentration of 50 % seems to lead to a narrowing of the reduction interval with increasing heating rate. This effect is due to a higher reaction velocity caused by the high hydrogen concentration, although the reduction period is short and should lead to an increase of ΔT. But in this case the difference between 5 % and 50 % hydrogen in the reduction gas has a serious effect. In order to show the dependence between the reduction interval and the heating rate the reduction interval Δt [min] was calculated and plotted for each hydrogen concentration. As one can see from Figure 4d the time for the reduction decreases with increasing heating rate. Highest Δt values were obtained for the lowest hydrogen concentration. This can easily be explained by the slower reaction due to the low hydrogen concentration of 1 %. The Δt values of the samples reduced with 5 % and 50 % hydrogen show only slight differences (2 K/min: 5 % H_2: 26.5 min, 50 % H_2: 25 min).

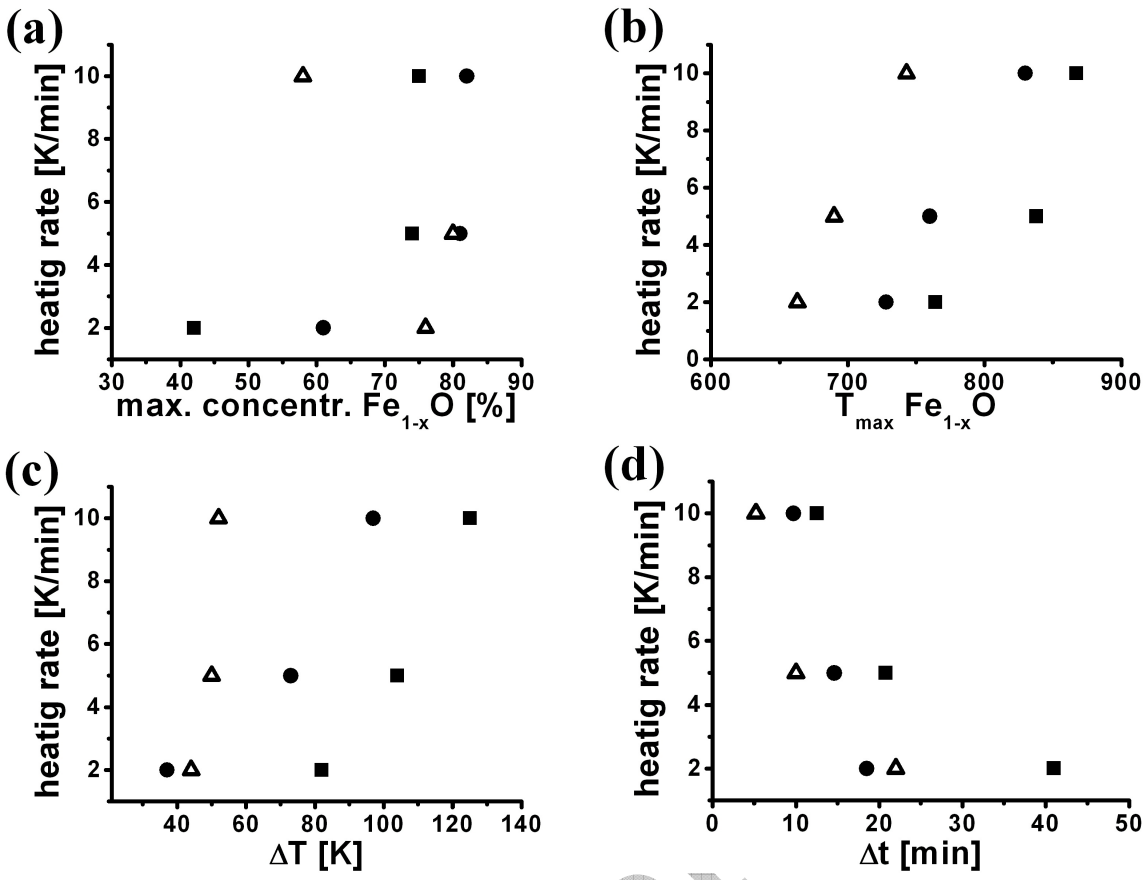

Figure 5: *Correlation between (a) the maximal $Fe_{1-x}O$ content, (b) the temperature of the $Fe_{1-x}O$ concentration maximum, (c) the reduction interval ΔT in [K] (full width half maximum (FWHM)) and (d) the reduction interval Δt in [min] and the heating rate for each hydrogen concentration from the reduction of Fe_2O_3@CMK-3. Legend: (□) 50 % H_2; (●) 5 % H_2; (■) 1 % H_2 in N_2.*

For the highest heating rate the differences between the different hydrogen concentrations decrease and the reduction intervals is between 5 and 11.5 minutes for each sample. This effect can be explained by the higher thermic movement of the particles at higher temperatures and a higher probability of encounter between a hydrogen molecule and a Fe_2O_3 particle.

One important fact that should be discussed in this context is the change in the crystal structure when reducing haematite to magnetite. The haematite, which is isostructural with corundum possesses a hexagonal shaped unit cell. Six oxygen atoms surround each iron atom. In the usual bulk haematite, these octahedrons are face-, edge- and corner-linked. For the guest species Fe_2O_3 in the pore system of the mesoporous host materials only corner- and edge-linked octahedra could be observed which leads to the assumption that there are slight differences between the structures of the bulk and the guest material within the pores of mesoporous systems which might be due to the limited particle size. With the reduction of the guest material from Fe_2O_3 to Fe_3O_4 the structure changes from the haematite like structure (corundum structure) to the inverse spinel structure of the magnetite which implies a cubic unit cell.

The dependence between the formation of $Fe_{1-x}O$ from Fe_3O_4, the heating rate as well as the hydrogen concentration is shown in Figure 3. For a better understanding the dependencies between the heating rate and the maximum concentration of $Fe_{1-x}O$ for each hydrogen concentration (Figure 5a), between T_{max} and the heating rate for each hydrogen concentration (Figure 5b) and between ΔT [K] and the heating rate (Figure 5c) as well as between Δt [min] and the heating rate (Figure 5d) for each hydrogen concentration are plotted. Similar plots were already described for the reduction of Fe_2O_3 to Fe_3O_4.

In contrast to the reduction of Fe_2O_3 the reduction of Fe_3O_4 and the formation of $Fe_{1-x}O$ differs significantly dependent on the hydrogen concentration. At a heating rate of 2 K/min the maximum concentration of $Fe_{1-x}O$ is only 42 % for a hydrogen concentration in the reduction gas of 1 %. At such low heating rate the maximum concentration of $Fe_{1-x}O$ is significantly dependent on the hydrogen concentration. For 5 % hydrogen 61 % and for a hydrogen concentration of 50 % 76 % of $Fe_{1-x}O$ can be detected. An increase of the heating rate to 5 K/min leads to a decrease of these discrepancies. Wüstite amounts between 74 and

81 % are obtained. At least, the increase of the heating rate up to 10 K/min leads to the assumption that concentrations of $Fe_{1-x}O$ above 82 % cannot be realized with further increase of the heating rate of an increase of the hydrogen concentration. An interesting evolution of the maximum amounts should be mentioned at this place. A heating rate of 10 K/min and a hydrogen concentration of 50 % in the reduction gas lead to a significant decrease of the wüstite concentration to 58 %. These extreme reduction conditions lead to a rapid reduction of Fe_3O_4 to $Fe_{1-x}O$ and a further reduction to pure Fe in nearly one step. Thus, in order to obtain a material containing the maximum concentration of wüstite the reduction conditions has to be carefully chosen due to the further reduction of $Fe_{1-x}O$ to pristine Fe.

As shown in Figure 5b the temperature with the maximum of $Fe_{1-x}O$ formation is increasing with increasing heating rate. This observation can be made for all hydrogen concentrations. As already explained for the reduction of Fe_2O_3 to Fe_3O_4 highest temperatures are needed for the lowest hydrogen concentration, which is due to the slower reduction at lower hydrogen concentrations as mentioned already above. In the measured range the correlation between T_{max} and the heating rate seem to be linear.

From Figure 5c one can conclude that the reduction interval ΔT is increasing for the samples synthesized with all three different hydrogen concentrations. Highest ΔT values are observed for the samples reduced with the lowest amount of hydrogen as expected. The reduction intervals measured for the samples synthesized with 50 % hydrogen show only a slight decrease. Similar observations as already described for the reduction of Fe_2O_3 could be made from Figure 5d. The correlation between Δt and the heating rate shows a decrease for the reduction time with increasing heating rate for each hydrogen concentration. With increasing hydrogen concentration the region of the reduction intervals decreases as well (for a heating rate of 10 K/min: 5 – 12.5 minutes). An explanation for these effects is given above.

The different formations of the individual phases dependent on the different synthesis parameters show the complexity of the reduction system $\alpha\text{-}Fe_2O_3 \rightarrow Fe_3O_4 \rightarrow Fe_{1-x}O \rightarrow Fe^0$. The results described above for the formation of Fe_3O_4 from $\alpha\text{-}Fe_2O_3$ and for the formation of $Fe_{1-x}O$ from Fe_3O_4 can be basically explained as follows:

On the one hand the thermal agility of the iron oxide particles at high temperatures might play an important role because agglomeration to larger particles can take place and thus, the change of the particle size might influence the reduction behavior of the iron oxides. The surface to volume (particle) ratio decreases with increasing particle size and thus, the reduction is shifted to higher temperatures and takes place in shorter reduction intervals, which is shown for the bulk material later on. On the other hand the probability of the encounter between the iron oxide particles and the hydrogen molecules is of great importance for the reduction. At high hydrogen concentrations more encounters between iron oxide particles and the hydrogen molecules take place and thus, the probability of a reaction increases. The main reason however is the complexity of the reduction reactions. Competing reactions take place in which the oxygen released by the reduction causes an opposed reaction. These competing reactions are all linked in a mutual thermic equilibrium attempting to permanently adjust itself due to the increasing reduction temperature. The continual new adjustment of the thermic equilibration and the opposed reaction directly affected by the heating rate and concentration of hydrogen, could explain the above observed and discussed results.

The Fe_2O_3@CMK-1 system provides comparable results. For the host/guest compounds (Fe_2O_3@CMK-3, Fe_2O_3@CMK-1) as well as for the bulk material a detailed kinetic analysis of the reduction would be desirable. Unfortunately, the state of scientific knowledge today does not allow the kinetic interpretation of these complex not time, but temperature dependent reactions.

Comparison of Fe_2O_3@CMK-1 with Fe_2O_3@CMK-3. The transferability of the results from the host-system CMK-3 to the host-system CMK-1 has been mentioned above and Figure 6 is shown here as an example thereof. Two host/guest compounds with approximately the same amount of iron(III) oxide and acceptable similar nanoparticle size distribution are compared. As depicted in Figure 6 Fe_2O_3@CMK-1 and Fe_2O_3@CMK-3 show nearly the same reduction profiles. The anticipated conformity in the formation of the individual reduction phases shows that the texture of the host-system has no influence in both cases. If the amount of iron(III) oxide and its nanoparticle size distribution is approximately the same, then the results can be transferred nearly one-to-one. Both parameters can be affected more or less during the synthesis, so that comparable sample batches are more or less available.

Influence of the amount of iron(III) oxide. The amount of iron oxide used for reduction influences the evolution of the reduction phases to some extent. Figure 7 shows the evolution of the phases with two different amounts (15 mg and 30 mg host/guest compound) of sample weight. A better resolution of the reduction profile with higher sample weight is visible. This is not surprising, taking into consideration that the thermal conductivity detectors work at the bottom end of the detection limit; therefore an increase of sample weight leads to a shift to a higher range of operation of the detectors and thus, to higher resoluted reduction profiles. The development of the single

reduction phases is not affected by the sample weight.

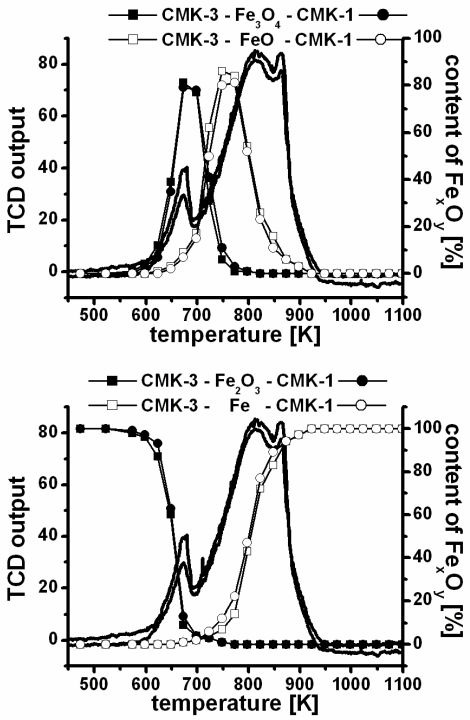

Figure 6: *Comparison of the evaluation of the reduction products of two host/guest compounds (Fe_2O_3@CMK-1 and Fe_2O_3@CMK-3) with approximately the same amount of iron(III) oxide and acceptable similar size distribution.*

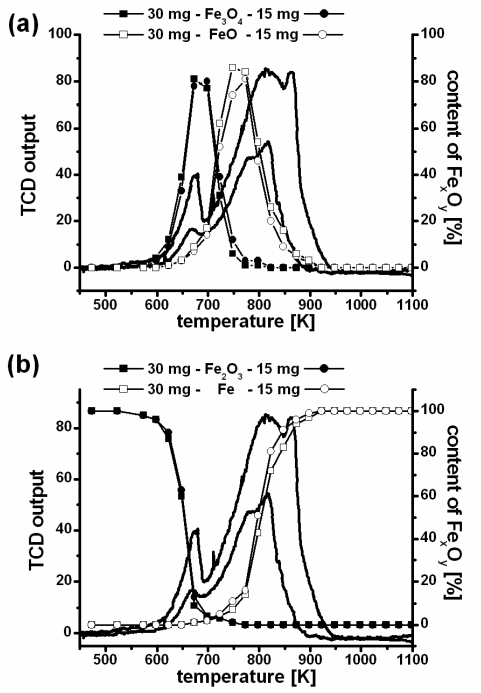

Figure 7: *Comparison of the evaluation of the reduction products of two host/guest compounds with approximately the same amount of iron(III) oxide per mg compound and acceptable similar size distribution. The difference is the weighted amount of sample for the tpr.*

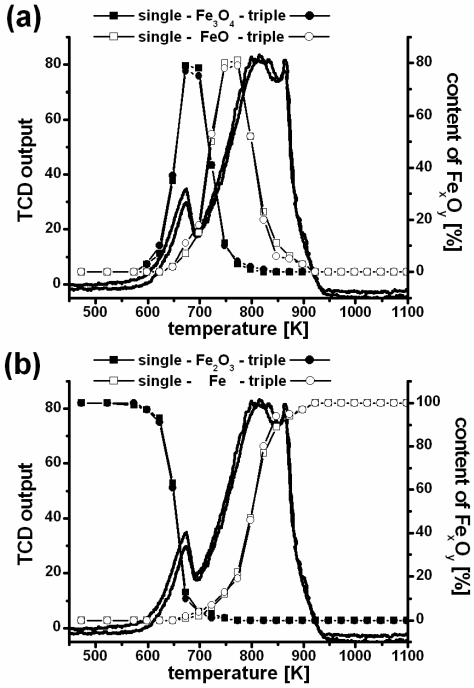

Figure 8: *Comparison of the evaluation of the reduction products of two host/guest compounds with approximately the same amount of iron(III) oxide and acceptable similar size distribution but single and triple loading with iron(III) oxide.*

Another possibility of increasing the amount of the reducible substance is the increase of the iron(III) oxide fraction in the host's mesopores. This can be achieved by multiple impregnations. A comparison of a single and a threefold impregnation of CMK-1 is depicted in Figure 8. The amounts of iron(III) oxides are 16 respectively 25 weight percent. By the use of multiple impregnations not only the proportion of iron(III) oxide is raised, but also the particle size is enlarged by the thickening of the layers or agglomeration. This type of increase however, does neither lead to a significant change in the reduction profile, nor to a change in the evolution of the different phases. This might be due to a too low mass change or to the impreciseness of the LC XANES evaluation.

Comparison with bulk haematite. Differences between the phase evolution of the host/guest compounds and the bulk material are published in a recent article and shall therefore just summarized briefly.[38] Generally, one can say that under the same reduction conditions the reduction of bulk material i) is initiated at higher temperatures, ii) is less selective and iii) takes place in shorter intervals. This can be explained by the fact that in the host/guest material iron oxide is located in thin layers in the mesopores of the host system, which results in the surface to volume ratio being much higher than in the respective bulk material. Thus, the hydrogen stream has access to more iron oxide

molecules in the host/guest compound compared to the accessibility of iron oxide molecules in the respective bulk material. The shorter reduction interval can be explained by diffusion control inside the pore system.

Results and discussion of the reduction at constant temperatures

Further interest occurs on the question, if it will be possible to produce the individual iron oxide phases within the pore system by means of the reductive method. For that purpose, the samples were heated up to the desired temperature and hold there until the detector signal fell to almost zero, which indicates the completeness of the reduction at this temperature. Figure 9 shows the reduction profiles of Fe_2O_3@CMK-3 at 573 K and 723 K, respectively.

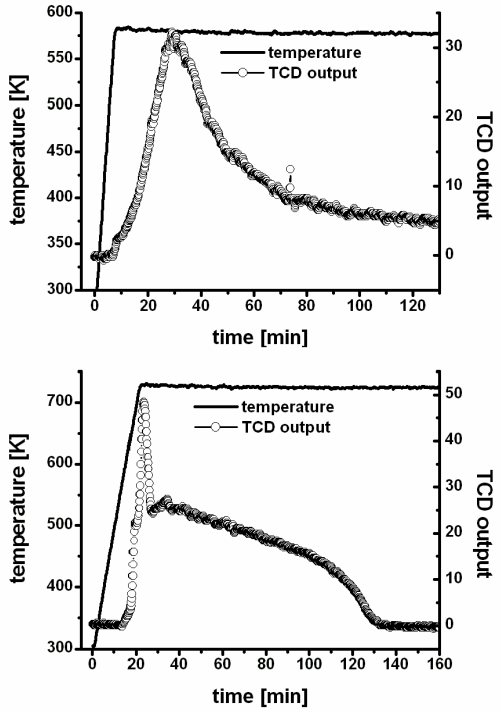

Figure 9: *Reduction profiles of Fe_2O_3@CMK-3 reduced at 573 K (top) respectively 723 K (bottom).*

The steep increase of the reduction profile during the heating phase is characteristic. After reaching the respective reduction temperature the signal falls and slowly approaches to zero. These time-dependent experiments were carried out in a temperature range of 523 K to 900 K with an interval of 25 K. The results from 573, 623, 723 and 873 K are discussed here because at these temperatures the highest amounts of the individual reduction phases occur.

As one can see from the conducted LC-XANES fit (data see Table 1) the reduction of the host/guest compound at 573 K leads to a pure Fe_3O_4-Phase. An additional EXAFS-analysis confirms the phase purity of Fe_3O_4 in the host/guest compound within the scope of the limits of detection (for detailed data see Table 2). In comparison with the bulk material the conventional reduction of the coordination numbers for nanostructured particles can be found for the host/guest compound. The distances themselves nearly correspond to those of the bulk materials.[35] Furthermore it is important, that the bulk material can only be reduced to a mixture of haematite (40 %) and magnetite (60 %) at this temperature. Here again, the influence of particle size upon the reduction behavior is evident (see above).

Table 1: *Results of the Linear Combination XANES fit for the host/guest compound (hgc) Fe_2O_3@CMK-3 as well as the bulk material (bm) after the reduction process at different temperatures.*

temp.	comp. / amount	Fe_2O_3	Fe_3O_4	$Fe_{1-x}O$	Fe^0
573 K	hgc	-	99 %	-	-
	bm	40 %	60 %	-	-
623 K	hgc	4 %	76 %	20 %	-
	bm	-	99 %	-	-
723 K	hgc	-	10 %	74 %	16 %
	bm	-	28 %	64 %	7 %
873 K	hgc	-	-	-	100 %
	bm	-	-	-	99 %

"-" means no contribution part or not detectable with the used method.

Table 2: *Refined structure parameters extracted from the Fe-K EXAFS of the reduced host/guest compounds and bulk materials as well as corresponding results extracted from single crystal data.[21]*

shell	CN	R [Å]	CN	R [Å]	CN	R [Å]
	Fe_3O_4@CMK-3 (573 K)		bulk Fe_3O_4 (623 K)		s.c.d.	
Fe-Fe	8.42	2.48	8.03	2.48	8	2.48
Fe-Fe	4.92	2.84	5.74	2.86	6	2.87
Fe-Fe	9.52	4.03	10.52	4.04	12	4.05
Fe-Fe	-	-	19.43	4.72	24	4.75
	Fe^0@CMK-3 (873K)		bulk Fe^0 (873 K)		s.c.d.	
Fe-O	3.54	1.86	3.99	1.88	4	1.88
Fe-Fe	9.76	3.47	11.30	3.49	12	3.48
Fe-O	8.79	3.46	10.98	3.51	12	3.49
Fe-Fe	2.71	3.67	3.55	3.62	4	3.64
Fe-O	-	-	10.01	4.50	12	4.52

CN: coordination number; R: bond length; s.c.d.: single crystal data[21]; for all: Debye-Waller factors below $0.48*10^{-2}$ Å^2; $\Delta E_0 < \pm 6.9$ eV; $R < 9.5$; $s_0^2 = 0.9$ fixed.

Bulk haematite is reduced to phase pure magnetite at a temperature of 623 K only. However, the reduction of the host/guest compound to $Fe_{1-x}O$ has already started at this temperature (see Table 1).

Amounts of $Fe_{1-x}O$ up to 20 % were detected whereas still 4 % Fe_2O_3 and 76 % Fe_3O_4 are existent in a phase blend. The maximum concentration of $Fe_{1-x}O$ from 74 % in presence of small amounts of Fe_3O_4 (10 %) and pure Fe (16 %) in the host/guest compound is obtained at a reduction temperature of 723 K (Tab. 1). The composition of the bulk material at this reduction temperature is 28 % Fe_3O_4, 64 % $Fe_{1-x}O$ and 7 % pure Fe. At a reduction temperature of 873 K the entire iron oxide is finally reduced to metallic iron for the host/guest compound as well as for the bulk material. The results of the EXAFS-analysis carried out for this studies are shown in Table 2. Similar to the Fe_3O_4-phase the distances are in good agreement with those of the bulk material. The anticipated decrease of the coordination numbers for the nanostructured particles is also evident.
Finally it can be said, that by means of an intra-pore reduction, up to 74 % $Fe_{1-x}O$ as well as pure Fe_3O_4 and $Fe_{1-x}0$ in the pore systems of CMK-3 and CMK-1 has been successfully synthesized.

Conclusion
In these studies the influence of the heating rate and the composition of reduction gas on the reduction performance of both host/guest compounds Fe_2O_3@CMK-1 and Fe_2O_3@CMK-3 has been shown. The kinetic reaction coherences of this complex reduction system α-$Fe_2O_3 \rightarrow Fe_3O_4 \rightarrow Fe_{1-x}O \rightarrow Fe^0$ do not allow an unambiguous interpretation of the dependencies shown at the present state of scientific research.
Nevertheless, the development of the individual reduction phases under different conditions has been described. Comparisons with different sample weights and with bulk material are useful for a better understanding of this complex system. The reduction steps α-$Fe_2O_3 \rightarrow Fe_3O_4 \rightarrow Fe_{1-x}O \rightarrow Fe^0$ are mainly affected by the spatial and chemical environment.
The nanostructured iron(III) oxide particles in the host/guest compounds were reduced to pure Fe_3O_4 (at 573 K), to a maximum of $Fe_{1-x}O$ of 74 % (723 K) and to pure metallic iron (873 K) with the help of the constant temperature reduction process.

The fundamental research described in this work enables an access to further investigations. Magnetic measurements on the magnetite-phase which show promising results are in progress. Besides this, the reduced phases shall undergo catalytic tests regarding the decomposition of methanol.

Acknowledgements
The authors would like to thank HASYLAB@DESY, Hamburg, Germany, for allocating beam time and financial support. Further financial support by the Justus Liebig University Giessen and the Fonds der Chemischen Industrie is gratefully acknowledged.

References
[1] Weitkamp, J.; Hunger, M.; Rymsa, U. Microporous Mesoporous Mater. 2001, 48(1-3), 255-270.
[2] Weitkamp, J.; Glaeser, R. Catalysis in Winnacker-Kuechler: Chemische Technik (5. Auflage) 2004, 1, 645-718. Publisher: Wiley-VCH Verlag GmbH & Co. KGaA, Weinheim, Germany CODEN: 69GEIJ, general review written in german.
[3] Bajt, S.; Sutton, S.R.; Delaney, J.S. Cosmochimica Acta 1994, 58, 5209-5214.
[4] Becker, K.D.; Niemeier, D.; Wissmann, S.; Oversluizen, M.; Couves, J.W.; Chadwick, A.V. Nucl. Instr. Meth. 1995, B97, 111-114.
[5] Cornell, R.M.; Schwertmann, U. The Iron Oxides, Wiley-VCH, Weinheim. 2003.
[6] Darken, L.S.; Gurry, R.W. J. Am. Chem. Soc. 1946, 68, 798-819.
[7] de Masi, R.; Reinicke, D.; Muller, F.; Steiner, P.; Hufner, S. Surf. Sci. 2002, 516, L515-L521.
[8] Dünwald, H.; Wagner, C. Z. Anorg. Allg. Chem. 1931, 199, 321-819.
[9] Fjellvang, H.; Hauback, B.C.; Vogt, T.; Stolen, S. Am. Mineral. 2003, 87, 347-349.
[10] Fröba, M.; Köhn, R.; Bouffaud, G.; Richard, O.; van Tendeloo, G. Chem. Mater. 1999, 11, 2858-2865.
[11] Köhn, R.; Fröba, M. Z. Anorg. Allg. Chem. 2003, 629, 1673-1682.
[12] Köhn, R.; Paneva, D.; Dimitrov, M.; Tsoncheva, T.; Mitov, I.; Minchev, C.; Fröba, M. Micropor. Mesopor. Mater. 2003, 63, 125-137.
[13] Rao, Y.K.; Moinpour, M. Metal Trans. B: Process Metallurgy 1983, 14B; 711-723.
[14] Minchev, C.; Huwe, H.; Tsoncheva, T.; Paneva, D.; Dimitrov, M.; Mitov, I.; Fröba, M. Micropor. Mesopor. Mater. 2005, 8, 333-341.
[15] Tsoncheva, T.; Paneva, D.; Mitov, I.; Huwe, H.; Fröba, M.; Dimitrov, M.; Minchev, C. React. Kinet. Catal. Lett. 2004, 83, 299-305.
[16] Basinska, A.; Jozwiak W.K.; Goralski J.; Domka F. Appl. Catal., A: General 2000, 190(1,2), 107-115.
[17] Chen, L.; Lu, G.L. J. Mater. Sci. 1999, 34, 17, 4193-4197.
[18] Takenaka, S.; Son, V.T.D.; Otsuka, K. Energy & Fuels 2004, 18, 3, 820-829.
[19] Waychumas, G.A.; Kim, C.S.; Banfield, J.F. J. Nanoparticles Res. 2005, 7, 409-433.

[20] Jolivet, J.P.; Chameac, C.; Tronc, E. Chem. Comm. 2004, 481-488.
[21] Blake, R.L.; Hessevick, R.E.; Zoltai, T.; Finger, L.W. Am Mineral 1966, 51, 123-129.
[22] Pauling, L.; Hendricks, S.B. J. Am. Chem. Soc. 1925, 47, 781-790.
[23] Selvam, P.; Dapurkar, S.E.; Badamali, S.K.; Murugasam, M.; Kuwano, H. Ad. Func. Mater. 2002, 12(2), 143-148.
[24] Redl, F.X.; Black, C.T.; Papaefthymiou, G.C.; Sandstrom, R.L.; Yin, M.; Zeng, H.; Murray, C.B.; O`Brien, S.P. J. Am. Chem. Soc. 2004, 126, 44, 14583-14599.
[25] Weng, Y.C.; Rusakova, I.A.; Baikalov, A.; Chen, J.W.; Wu, N.L. J. Mater. Res. 2005, 20, 1, 75-80.
[26] Brieler, F.J.; Grundmann, P.; Fröba, M.; Chen, L.; Klar, P.J.; Heimbrodt, W.; Krug von Nidda, H.-A.; Kurz, Th.; Loidl, A. Chem. Mater. 2005, 17, 4, 795-803.
[27] Bradshow, A.V. Trans Inst Min Metall 1970, 79C, 281-294.
[28] St. John, D.H.; Mathews, S.P.; Hayes, P.C. Met Trans. 1984, 15B, 701-708.
[29] Rau, M.; Rieck, D.; Evans, J.W. Met Trans. 1987, 18B, 257-278.
[30] Hayes, P.C.; Grieveson, P. Trans Chim B 1981, 12B, 319-326.
[31] El-Tabirou, M.; Dupre, B.; Gleitzer, C. Met Trans. 1988, 19B, 311-317.
[32] Klar, P.J.; Chen, L.; Heimbrodt, W.; Brieler, F.J.; Fröba, M.; Kurz, T.; Krug von Nidda, H.-A.; Loidl, A. Advances in Solid State Physics, 2004, vol 44, edited by B. Kramer, pp. 491-502, Springer-Verlag, Berlin Heidelberg.
[33] Huwe, H.; Fröba, M. Microporous Mesoporous Mater 2003,60, 151-158.
[34] Huwe, H.; Fröba, M. Carbon 2006 in press.
[35] Huwe, H.; Fröba, M. Anal Bioanal Chem 2006, 384, 817-826
[36] Minchev, C.; Huwe, H.; Tsoncheva, C.; Paneva, D.; Dimitrov, M.; Mitov, I.; Fröba, M. Microporous Mesoporous Mater 2005, 81, 333-341.
[37] Huwe, H.; Fröba, M. J. Synchrotron Radiation 2004, 11, 363-365.
[38] Huwe, H.; Fröba, M. J. Synchrotron Radiation 2006, 13, 275-277.
[39] Ryoo, R.; Joo, S.H.; Jun, S. J. Phys. Chem. B 1999, 103, 37, 7743-7746.
[40] Kruk, M.; Jaroniec, M.; Ryoo, R.; Joo S.H. J Phys Chem B 2000, 104, 33, 7920-7925.
[41] Jun, S.; Joo, S.H.; Ryoo, R.; Kruk, M.; Jaroniec, M.; Liu, Z.; Ohsuna, T.; Terasaki, O. J. Am Chem Soc 2000, 122, 43, 10712-10713.
[42] Ryoo, R.; Joo, S.H.; Kruk, M.; Jaroniec, M. Adv Mater 2001, 13, 9, 677-681.
[43] Joo, S.H.; Choi, S.J.; Kwak, J.; Liu, Z.; Terasaki, O.; Ryoo, R. Nature 2001, 412, 6843, 169-1728.
[44] Shin, H.J.; Ryoo, R.; Kruk, M.; Jaroniec, M. Chem Commun 2001, 4, 349-350.
[45] Lee, J.S.; Joo, S.H.; Ryoo, R. J Am Chem Soc 2002, 124, 7, 1156-1157.
[46] Solovyov, L.A.; Shmakov, A.N.; Zaikovskii, V.I.; Joo, S.H.; Ryoo, R. Carbon 2002, 40, 13, 2477-2481.
[47] Darmstadt, H.; Roy, C.; Kaliaguine, S.; Choi, S.J.; Ryoo, R. Carbon 2002, 40, 14, 2673-2683.
[48] Fuertes, A.B. Microporous Mesoporous Mater 2004, 67, 273-281
[49] Darmstadt, H. ; Roy, C. ; Kaliaguine, S. ; Joo, S.H. ; Ryoo, R. Microporous Mesoporous Mater 2003, 60, 1-3, 139-149.
[50] Ryoo, R. ; Joo, S.H. Stud Surf Sci Catal 2004, 148, 241-260.
[51] Lee, J.; Yoon, S.; Hyeon, T.; Oh, S.M.; Kim, K.B. Chem Commun 1999, 2177-2178.
[52] Kang, M.; Kim, D.; Yi, S.H.; Han, J.U.; Yie, J.E.; Kim, J.M. Catal. Today 2004, 93-95, 695-699.
[53] Ressler, T. J. Synchrotron Radiation 1998, 5, 118-122.
[54] Newville, M.; Ravel, B.; Haskel, D.; Rehr, J.J.; Stern, E.A.; Yacoby Y. Phys B 1995, 208, 154-156.

3 Diskussion der Ergebnisse

In diesem Kapitel sollen die wichtigsten Ergebnisse der voran stehenden Veröffentlichungen wiedergegeben werden. Gleichzeitig dient es dazu, die Ergebnisse im Zusammenhang darzustellen. Alle hier getroffenen Aussagen finden sich in den voran stehenden Veröffentlichungen V2.1 bis V2.8 wieder, auf eine Zitation der entsprechende Stelle wird daher verzichtet.

Wie schon in der Einleitung kurz beschrieben, wurden die Gastspezies über ein nasschemisches Imprägnierungsverfahren in die Porenkanäle der Wirtspezies eingelagert. Die Imprägnierungsprozedur ist schematisch in Abbildung 3 dargestellt. Je nach Anzahl dieser Imprägnierungsprozesse werden unterschiedliche Gehalte an Metalloxiden in den mesoporösen Kohlenstoffen erhalten. So konnten z.B. Gehalte von bis zu 65 Gew.-% für Eisen(III)oxid erzielt werden. Mit Hilfe der Röntgenpulverdiffraktometrie (P-XRD), der Stickstoff-Physisorption, der Raman-Spektroskopie und der Transmissionselektronenmikroskopie (TEM) konnte die erfolgreiche Synthese der verschiedenen Metalloxide hauptsächlich in den Porensystemen der Wirte bei gleichzeitiger Erhaltung der Wirtstruktur nachgewiesen werden, wie nun stellvertretend für alle am Beispiel Fe_2O_3@CMK-1 verdeutlicht werden soll.

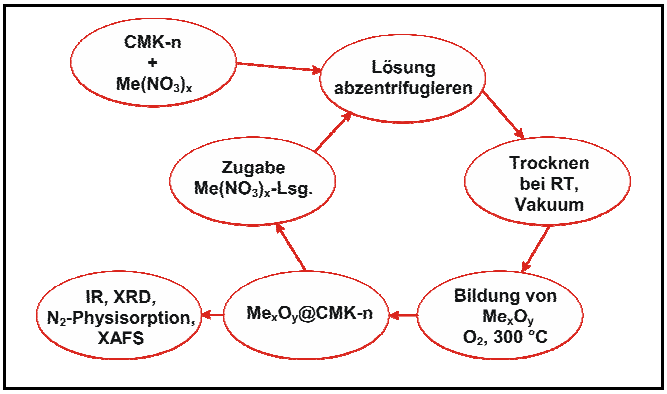

Abbildung 3: Schema des Imprägnierungsprozesses. Der Calcinierungsprozess (Bildung von Me_xO_y) wird hier als mit zum Imprägnierungsprozess zugehörend betrachtet.

Typische Röntgendiffraktogramme sind in Abbildung 4a gezeigt. Die Beugungsreflexe der Wirtstruktur nehmen mit jedem Imprägnierungszyklus (immer einschl. Calcinierungsprozess, s. Abb. 3) ab und die Maxima verschieben sich hin zu kleineren d-Werten (Tabelle 2). Gleichzeitig ist im höheren Winkelbereich (Abb. 4b), in dem die Hauptreflexe von volumenkristallinem Hämatit auftreten, kein Reflex zu erkennen. Nach dem vierten

Imprägnierungszyklus ist nur ein schwacher, breiter Reflex von hauptsächlich röntgenamorphen, kleinen Eisen(III)oxid Kristalliten sichtbar. Dies zeigt, dass sich kein kristallines Eisen(III)oxid außerhalb der Porenkanäle befindet.

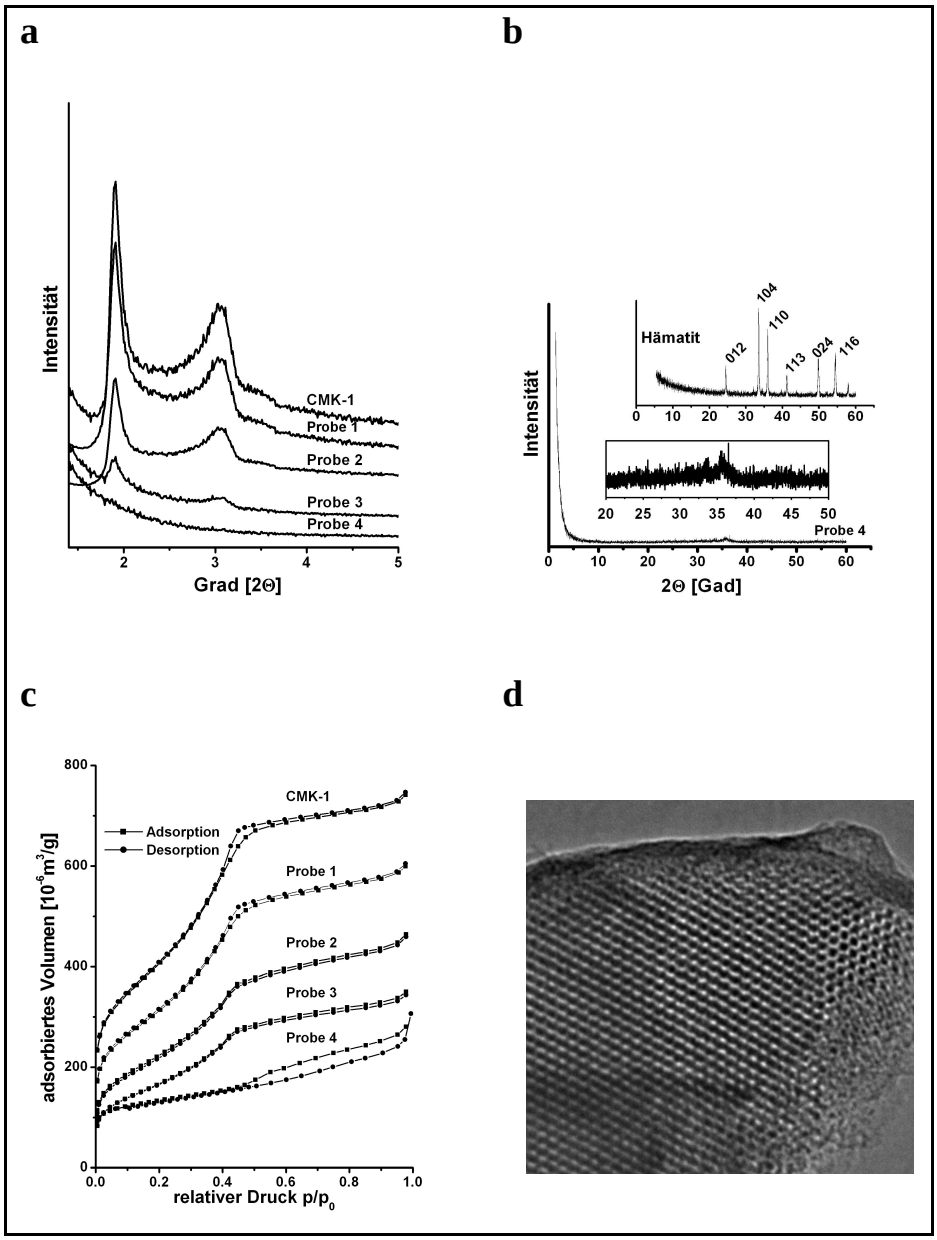

Abbildung 4: a) P-XRD im unteren Winkelbereich, b) P-XRD im Winkelbereich, in dem die stärksten Hämatitreflexe auftreten, c) N_2-Sorptionsisothermen von CMK-1 und der entsprechenden Wirt/Gast-Verbindung sowie d) TEM der Wirt/Gast-Verbindung nach dem vierten Imprägnierungszyklus (Probe 4).

Die Isothermen der N_2-Physisorption (Abb. 4c) können dem Typ IV nach IUPAC[48] zugeordnet werden; er ist typisch für mesoporenhaltige Materialien. Daneben zeigen sie einen gut sichtbaren Kapillarkondensationsschritt im Bereich p/p_0 = 0,3 – 0,45 für die Proben der

ersten drei Imprägnierungszyklen. Gleichzeitig ist mit jedem Imprägnierungszyklus eine Abnahme der adsorbierten Menge an Stickstoff zu beobachten. Die Porendurchmesser nehmen mit jedem Imprägnierungszyklus ab, die Porenradienverteilung wird dabei immer breiter (Tabelle 2). Dies ist ein Effekt, der auf ein inhomogenes Füllen der Poren zurückzuführen ist. Die Ergebnisse der N_2-Sorption deuten darauf hin, dass mit jedem Imprägnierungszyklus der Gehalt an Eisen(III)oxid in den Mesoporen zunimmt. Zusätzlich zeigt sich, dass das Porensystem des CMK-1 während der Imprägnierung nicht zerstört wird.

Tabelle 2: Daten der P-XRD und N_2-Physisorptionsmessungen für den CMK-1 und die Einlagerungsverbindungen Fe_2O_3@CMK-1 nach bis zu 4 Imprägnierungszyklen (Probe 1 bis 4).

	d_{110} [nm]	d_{211} [nm]	S_{BET} [m^3/g]	D_p [nm]	V_p [cm^3/g]
CMK-1	4,70	2,91	1403	3,11	0,74
Probe 1	4,65	2,89	1210	3,10	0,60
Probe 2	4,63	2,87	1005	3,06	0,46
Probe 3	4,55	-	634	3,02	0,35
Probe 4	-	-	220	< 1	0,30

d_{hkl}: d-Werte der P-XRD-Reflexe; S_{BET}: innere Oberfläche nach BET berechnet; D_p: Porendurchmesser nach BJH; V_P: Gesamtporen-volumen im relativen Druckbereich p/p_0 = 0,97 – 0,99.

Ein repräsentatives TEM-Bild, aufgenommen nach dem vierten Imprägnierungszyklus, zeigt deutlich, dass die Porenstruktur des CMK-1 erhalten geblieben ist und es sich keine Eisen(III)oxidteilchen auf der Oberfläche befinden.

Um zu überprüfen, ob die Umsetzung vom Eisennitrat zum Eisenoxid während des Imprägnierungsprozesses vollständig abgelaufen ist, wurden IR-Spektren aufgenommen. Mit ihrer Hilfe konnte die vollständige Zersetzung des Nitrations während der Imprägnierungsprozedur nachgewiesen werden. Die für Nitrationen charakteristische Bande bei 1380 cm^{-1} war nicht mehr zu detektieren.

Wie Untersuchungen gezeigt haben, bildet sich aus dem Eisennitrat während der Imprägnierungsprozedur Eisen(III)oxid mit einer hämatitähnlichen Struktur in den Poren der CMK-n aus. Volumenkristallines Hämatit selber kristallisiert im Korund-Typ. Die Sauerstoff-atome bilden dabei eine hexagonal dichteste Kugelpackung mit oktaedrischen Lücken, welche zu zwei Drittel mit Eisen(III)ionen gefüllt sind. Somit ergeben sich FeO_6-Oktaeder, die über die Seite, die Ecke und die Kante miteinander verknüpft sind.[35,49,50] Bedingt durch die Nanostrukturierung der Einlagerungsverbindung weichen die ermittelten Werte für die

Koordinationszahlen und Atomabstände von denen des Volumenkristalls ab. Dennoch ist, wie später gezeigt wird, eine hämatitähnliche Struktur deutlich nachzuweisen.

Um einen Einblick in die lokale Struktur des gebildeten Eisen(III)oxides sowie eine Bestätigung der Bildung derselben zu bekommen, wurden Röntgenabsorptionsspektren (XAS) an der Fe K-Kante aufgenommen. Von den aufgenommenen Spektren wurde der Bereich der EXAFS (extended X-ray absorption fine structure) für die Auswertung benutzt. Eine daraus extrahierte, modifizierte radiale Verteilungsfunktion ist in Abbildung 5 dargestellt. Deutlich ist zu sehen, dass die Einlagerungsverbindung im Gegensatz zum volumenkristallinen Hämatit keine Koordinationsschalen bei größeren Radien beziehungsweise Bindungslängen aufzeigt (3,5 Å zu 7,5 Å), ein Effekt, der durch die kleinen Partikelgrößen oder „static disorder effects“ der nanostrukturierten Einlagerungsverbindungen bedingt ist. Gleichzeitig ist die Intensität der Fe-Fe-Schalen gegenüber dem volumenkristallinen Hämatit stark reduziert, ebenfalls ein Effekt hervorgerufen durch die Nanostrukturierung des Eisen(III)oxides.

Wie schon Blake[34] gezeigt hat, können aus den einzelnen Schalen Informationen über den Aufbau der FeO_6-Oktaeder gewonnen werden. Im Bereich von 1,9 bis 3,7 Å treten die Fe-Fe-Schalen auf, die, bedingt durch die verschiedenen Verknüpfungsarten der FeO_6-Oktaeder, in vier Unterschalen aufgeteilt werden können.

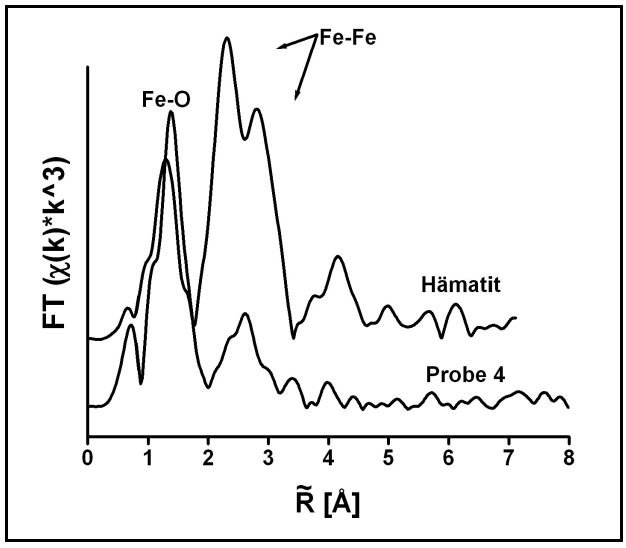

Abbildung 5: Modifizierte radiale Verteilungsfunktion von der EXAFS-Oszillation an der Eisen K-Kante der Wirt/Gast-Verbindung Fe_2O_3@CMK-1 nach dem vierten Imprägnierungszyklus und der von volumenkristallinem Hämatit.

Die Koordinationsschalen bis zu 3,28 Å werden durch flächen- und kantenverknüpfte, die oberhalb davon durch eckenverknüpfte Oktaeder gebildet. Mit Hilfe einer EXAFS-Analyse können nun die zu den auftretenden Schalen gehörenden Parameter wie Abstand und Koordinationszahl des volumenkristallinen Hämatits und der Wirt/Gast-Verbindungen ermittelt, mit Werten aus Einkristalldaten verglichen und somit Strukturveränderungen aufgezeigt werden. Die Analyse hat gezeigt, dass die Parameter für das volumenkristalline Hämatit in guter Übereinstimmung mit den Einkristalldaten liegen. Im Gegensatz dazu zeigt die Einlagerungsverbindung eine deutliche Abnahme bei den Koordinationszahlen, welche typisch für kleine Partikel und „static disorder effects“ ist. Im Gegensatz zum volumenkristallinen Hämatit tritt die erste Schale der Nanopartikel bei einem Abstand von 2,94 Å auf. Dieser Abstand liegt zwischen denen von Manceau[51] angegebenen für seiten- und eckenverknüpften Eisen(III)oxid-Oktaedern. In den Porensystemen der CMK-n wurden also ungeordnete Eisen(III)oxid-Nanopartikel synthetisiert, die im Vergleich zum volumenkristallinen Hämatit aus FeO_6-Oktaeder ohne Flächenverknüpfungen bestehen.

Um weiterreichende Informationen aus der EXAFS-Analyse zu erhalten, wurde die bisher übliche Auswertungs- und Fitprozedur dem nanostrukturierten Eisen(III)oxidsystem angepasst. Mit Hilfe der EXAFS-Analyse unter Einbeziehung von Mehrfachstreupfaden und einer neuen Prozedur bei der Verfeinerung der FEFF-Files konnten so neue Strukturinformationen gewonnen, deren Gewinnung bisher nicht möglich war. Dieser neue Weg ist schematisch in Abbildung 6 dargestellt.

Der umfassende Vergleich zwischen der herkömmlichen und der neuen Auswertungsprozedur unter Berücksichtigung z.B. der Mehrfachstreupfade, der Fe-O-Schalen und den Beiträgen von höheren Schalen ist ausführlich in der Veröffentlichung V2.6 beschrieben. Als ein Ergebnis wurde gezeigt, dass mit Hilfe der neuen Prozedur eine umfassende Strukturanalyse sowohl des volumenkristallinen Hämatits als auch der Einlagerungsverbindung über die ersten 4 Fe-Fe-Schalen möglich ist. Für das volumenkristalline Hämatit wurde eine sehr gute Übereinstimmung zwischen den gewonnenen Parametern für die Bindungslänge und Koordinationszahl mit denen der Einkristalldaten ermittelt. Einzige Ausnahme bildet die starke Abnahme der Koordinationszahl in der vierten Fe-Fe-Schale gegenüber den Einkristalldaten. Diese für höhere Schalen wohlbekannte Reduktion, zusammen mit den sich nicht signifikant ändernden Debye-Waller-Faktoren, ist wahrscheinlich auf kleinste Partikel im volumenkristallinen Hämatit oder eine strukturelle Unordnung zurückzuführen.

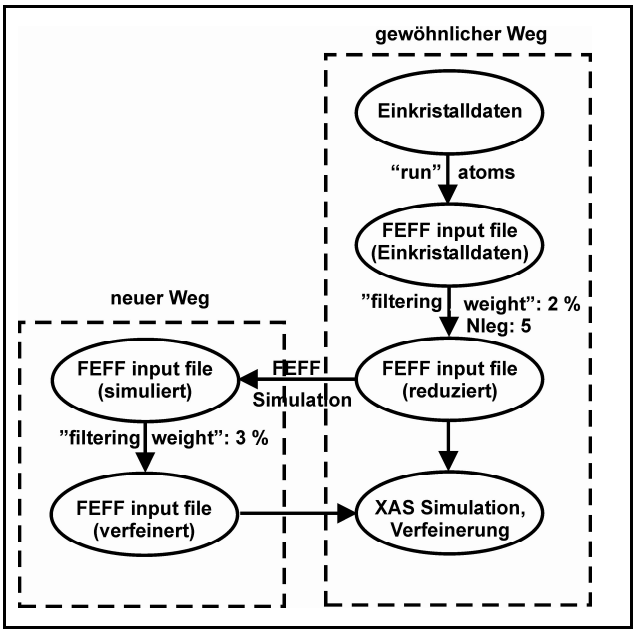

Abbildung 6: Gewöhnliche und neue, verfeinerte Prozedur für die FEFF-Files.

Die Koordinationszahlen der Einlagerungsverbindungen sind im Vergleich mit denen des Einkristalls signifikant kleiner. Dagegen wiesen die Debye-Waller-Faktoren nur kleine Änderungen auf. Die Kombination aus der Reduktion der Koordinationszahlen mit den nur minimalen Änderungen der Debye-Waller-Faktoren zeigt, dass sich im Porensystem sehr kleine Nanopartikel (< 3 nm) gebildet haben. Die erste Fe-Fe-Schale tritt bei einem Abstand auf, bei dem sich die Oktaeder nur über die Kante und nicht wie im Einkristall über die Fläche miteinander verknüpfen können. Auch die Bindungslängen für die zweite und vierte Koordinationsschale unterscheiden sich von denen der Einkristalldaten, sie gehören zu kanten- und eckenverknüpften Oktaedern. Anders als beim volumenkristallinen Hämatit treten keine flächenverknüpften Oktaeder ($r \approx 2{,}91$ Å) auf. Diese vollständige Strukturinformation bezüglich der nanostrukturierten Einlagerungsverbindung ist nur mit Hilfe der verfeinerten Auswerteprozedur möglich. Es wurde gezeigt, dass dieses Eisen(III)oxid aus kanten- und eckenverknüpften FeO_6-Oktaedern besteht. Ein Effekt, der auf die sehr kleinen Teilchen in den Poren zurückzuführen ist. Die im Hämatit auftretenden flächenverknüpften Oktaeder konnten nicht nachgewiesen werden.

Nach der Synthese und Charakterisierung der Einlagerungsverbindungen Fe_2O_3@CMK-1 und Fe_2O_3@CMK-3 wurden auch weitere 3d-Metalloxide von Mangan, Cobalt, Nickel, Kupfer und Zink in den mesoporösen Kohlenstoffen erfolgreich synthetisiert. Im Anschluss daran erfolgte die Reduktion innerhalb der Porensysteme mit einem Gemisch aus 5 % Wasserstoff

in Stickstoff. Neben den bereits oben beschriebenen Untersuchungsmethoden mittels P-XRD, TEM, IR- und Raman-Spektroskopie wurde an dieser Probenserie eine XANES- und EXAFS-Analyse durchgeführt.

Ein erster Blick auf die XANES-Spektren (Abb. 7, Cu_xO_y@CMK-3) zeigt, dass jeweils zwei Spektren (Einlagerungsverbindung und Volumenkristall) gleiche Kantenpositionen und gleiches Schwingungsverhalten aufweisen. Dies ist ein erster Hinweis auf die in den Poren vorliegende Phase.

Gleichzeitig ist eine für kleine Teilchen typische Verbreiterung der Kante zu erkennen.[23] Einige Spektren zeigen kleine Vorkantenpeaks (pre-edge peaks) die mit denen des Volumenkristalls übereinstimmen. Ein Vergleich der Lage der Absorptionskanten zwischen der jeweiligen unreduzierten und reduzierten Verbindung zeigt die erwartete Verschiebung hin zu kleineren Energien. Sie beträgt zum Beispiel für $Fe_2O_3 \rightarrow Fe$ ~ 8 eV, $NiO \rightarrow Ni$ ~ 0,8 eV und ~ 4 eV für $CuO \rightarrow Cu$, jeweils Oxid minus Metall. Diese Werte stimmen sehr gut mit den Literaturwerten der entsprechenden Volumenkristalle überein.[52]

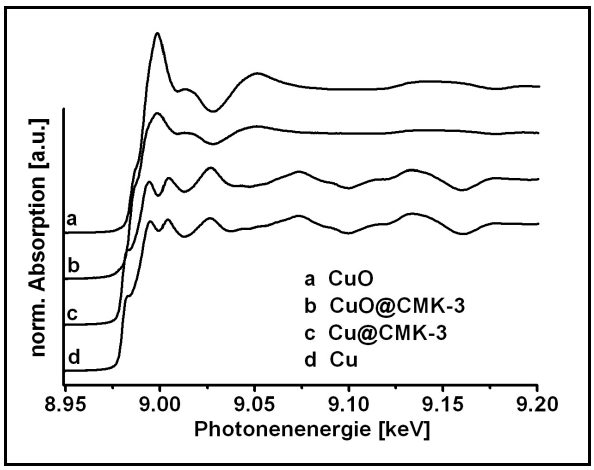

Abbildung 7: Normalisierte Cu-K-XANES-Spektren der Verbindung Cu_xO_y@CMK-3 und den entsprechenden Volumenkristallen Cu und CuO.

Zusätzlich zu den oben beschriebenen Untersuchungsmethoden wurde eine Linearkombination (LC) unterschiedlicher XANES-Spektren durchgeführt. Dabei handelt es sich vereinfacht gesagt um einen linearkombinatorischen Fit von Nahkantenspektren der Röntgenabsorptionsspektroskopie. Dafür werden zuerst verschiedene bekannte Verbindungen an der gleichen Absorptionskante aufgenommen. Mit dem anschließenden Auswertungs-

verfahren können dann deren Anteile an der unbekannten Einlagerungsverbindung bestimmt werden. Somit wurde zum einen die gebildete Phase bestimmt und zum anderen die Phasenreinheit der Einlagerungsverbindungen gezeigt: Es wurde MnO_2@CMK-3 zu MnO@CMK-3, Fe_2O_3@CMK-3 zu Fe@CMK-3, Co_3O_4@CMK-3 zu Co@CMK-3 NiO@CMK-3 zu Ni@CMK-3 und CuO@CMK-3 zu Cu@CMK-3 reduziert.

Mit Hilfe der EXAFS-Analyse wurden die Ergebnisse der LC XANES-Fits bestätigt und der räumliche Aufbau der gebildeten Einlagerungsverbindungen bestimmt. Die oben für das System Fe_2O_3@CMK-1 gemachten Aussagen können analog übernommen werden.
Die beiden durchgeführten XAS-Analysen zeigen deutlich, dass in dem Porensystem vom CMK-3 leicht ungeordnete Nanopartikel der 3d-Metalle und Metalloxide gebildet wurden. Im Fall von ZnO@CMK-3 wurde eine Strukturverbesserung in Bezug auf die Einkristalldaten durch den Reduktionsprozess und im Fall von MnO_2@CMK-3 eine Reduktion zu MnO@CMK-3 und nicht zu Mn@CMK-3 festgestellt. Eine Reduktion zu Zn@CMK-3 und Mn@CMK-3 ist durch die Bedingungen während des Reduktionsprozesses nicht möglich.

Wie schon in der Einleitung ausgeführt und begründet wurde, bildet das Eisenoxidsystem einen Schwerpunkt bei den durchgeführten Reduktionsuntersuchungen. Ziel war es, Informationen über das Reduktionsverhalten von nanostrukturierten Metalloxiden innerhalb der Porensysteme der Gaststrukturen zu gewinnen, um so möglichst phasenreines, nanostrukturiertes Magnetit, Wüstit und Eisen herzustellen zu können. Dazu wurden umfangreiche Reduktionsuntersuchungen unter Variation der Reduktionsparameter wie Heizrate und Reduktionsgasmenge durchgeführt. Ausgehend von diesen Ergebnissen wurden dann ausgewählte Proben einer zeitabhängigen Reduktion bei konstanter Temperatur unterzogen, um so eine größtmögliche Menge an nanostrukturiertem Magnetit, Wüstit und Eisen in den Poren der Wirtstruktur herstellen zu können.
Jede Einlagerungsverbindung wurde mittels der oben aufgeführten Methoden charakterisiert. Ein Schwerpunkt dabei bildeten wie bereits beschrieben die Strukturuntersuchungen der Gastspezies mit Hilfe der Röntgenabsorptionsspektroskopie (LC-XANES und EXAFS). Aus den Ergebnissen der Strukturuntersuchungen wurden verschiedene Reduktionsprofile erstellt, jeweils in Abhängigkeit von der Heizrate und der Menge an Reduktionsgas, und miteinander verglichen. Ein typisches Reduktionsprofil zeigt die Abbildung 8.
Das erste Maximum des Reduktionsprofils zeigt die Umwandlung von Hämatit zu Magnetit, das zweite die von Magnetit zu dem nicht-stöchiometrischen Wüstit und das dritte die

Reduktion zum metallischen Eisen. Gleichzeitig zeigt die Abbildung 8 die Entwicklung der einzelnen Eisenoxidphasen während des Reduktionsprozesses.

Um einen Eindruck über die Komplexität der Reduktion zu bekommen, sind in Abbildung 8 die Entwicklung der Magnetitphase aus der Reduktion der Probe Fe_2O_3@CMK-3 unter verschiedenen Reduktionsbedingungen dargestellt. Sie soll hier stellvertretend für die anderen Phasenentwicklungen diskutiert werden.

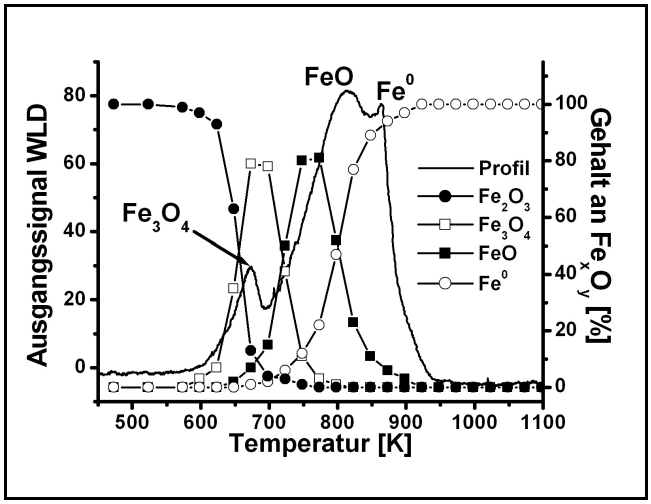

Abbildung 8: Reduktionsprofil für die Reduktion von Hämatit mit Entwicklung der einzelnen Phasen während des Reduktionsprozesses.

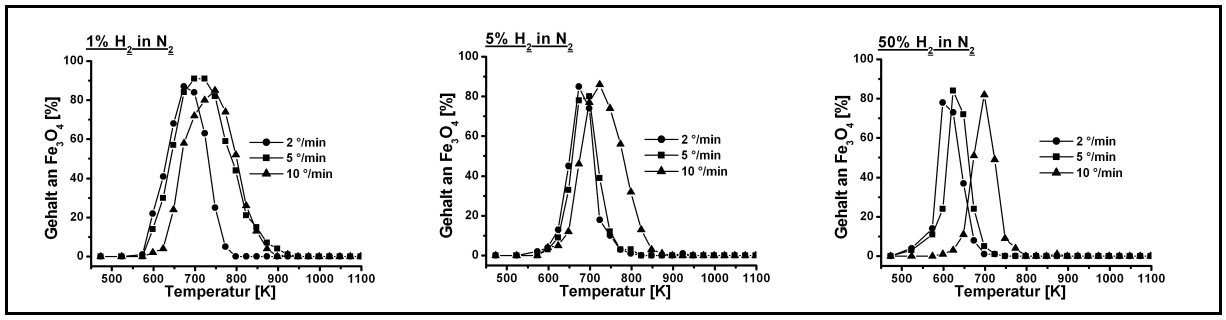

Abbildung 9: Entwicklung der Magnetitphase der Wirt/Gast-Verbindung Fe_2O_3@CMK-3 in Abhängigkeit von der Heizrate und der Wasserstoffkonzentration.

Es ist sehr deutlich zu sehen, dass der relative Anteil an Magnetit nicht von der Heizrate und der Wasserstoffkonzentration abhängt. Er liegt immer zwischen 80 und 90 %, der „höchste“ Anteil wird dabei mit der niedrigsten Wasserstoffkonzentration erreicht. Dieser Effekt kann auf eine langsamere Reduktion bei abnehmender Wasserstoffkonzentration zurückgeführt werden und bewirkt damit gleichzeitig eine geringere Reduktionsrate für die Reduktion zu $Fe_{1-x}O$@CMK-3.

Zu sehen ist auch, dass die Bildung von Fe_3O_4@CMK-3 mit abnehmender Wasserstoffkonzentration hin zu höheren Temperaturen verschoben wird und die Intervallbreite entsprechend zunimmt. Ein Effekt, der ebenfalls auf eine langsamere Reduktion bei abnehmender Wasserstoffkonzentration zurückzuführen ist.

Um die während der Reduktion der einzelnen Proben auftretenden Effekte zu verdeutlichen, wurden die Korrelationen zwischen der Heizrate, der Wasserstoffkonzentration, der maximalen Reduktionstemperatur und der Reduktionsintervallbreite (Halbwertsbreiten, FWHM) für die Magnetitphase aus den Messungen der Abbildung 9 extrahiert und zusammengefasst (Abb. 10).

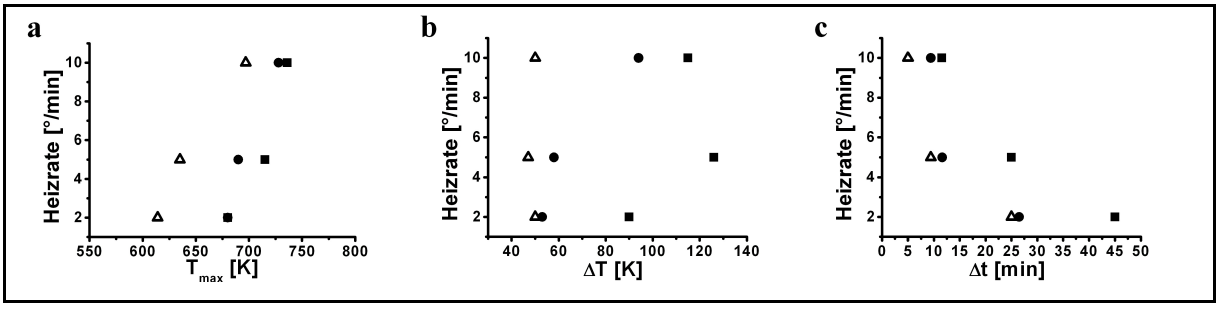

Abbildung 10: a) Temperaturen T_{max}, bei denen die maximalen Konzentrationen an Magnetit auftreten, b) die Halbwertsbreiten ΔT der Reduktionsintervalle und c) die Zeitspanne Δt der Reduktionsintervalle für verschiedene Wasserstoffkonzentrationen in Abhängigkeit von den Heizraten bei der Reduktion von Fe_2O_3@CMK-3.
Es bedeutet: (■)1 % H_2; (●) 5 % H_2;(Δ) 50 % H_2 in N_2.

In der Abbildung 10a ist ein deutlich linearer Zusammenhang zwischen der Temperatur, bei der die maximale Konzentration an Magnetit auftritt (T_{max}), und der Heizrate für die jeweiligen Wasserstoffkonzentrationen sichtbar. Die Temperaturen, bei denen die maximale Magnetitkonzentration erreicht wird, ist annähernd gleich für die Proben, die mit 1 % und 5 % H_2 in N_2 reduziert wurden. Sie startet bei 680 K für die Heizrate von 2 °/min und steigt mit zunehmender Heizrate auf 730 K. Für die Wasserstoffkonzentration von 50 % ist eine deutliche Verschiebung zu niedrigeren T_{max} zu erkennen. Der Einfluss der Wasserstoffkonzentration auf T_{max} ist signifikant. Die deutlich niedrigere maximale Temperatur für die hohe Wasserstoffkonzentration kann mit einer schnelleren Reduktion, bedingt durch die höhere Wasserstoffkonzentration, erklärt werden.
Der Einfluss der Wasserstoffkonzentration und der Heizrate auf die Breite des Reduktionsintervalls (ΔT) zeigt keinen so klaren Trend. Daher sollte die Interpretation der Abbildung 10b sehr vorsichtig erfolgen. Als erstes ist ein sehr deutlicher Einfluss der

Wasserstoffkonzentration auf die Breite des Reduktionsintervalls sichtbar. Bei der niedrigen Wasserstoffkonzentration von 1 % benötigt die Reduktion mehr Zeit als bei den höheren, was zu einer Verbreiterung von ΔT führt.
Eine deutliche lineare Korrelation zwischen der Heizrate und der Reduktionsintervallbreite für die Proben reduziert mit 1 % und 5 % H_2 ist nicht zu erkennen. Es sieht aber so aus, als ob ΔT mit zunehmender Heizrate breiter wird. Dabei sollte aber der Einfluss der Reaktionszeit zusätzlich zur Temperatur nicht vernachlässigt werden. Das Reduktionsintervall ΔT ist begrenzt durch die Starttemperatur T_s und die Endtemperatur T_E. Diese Temperaturen werden, bedingt durch die verschiedenen Heizraten, nach unterschiedlichen Zeiten erreicht. Durch den schnelleren Reduktionsprozess bei der Heizraten von 10 °/min nimmt ΔT zu, da das System noch Zeit für die Einstellung des Gleichgewichtes benötigt. Daher sind Überlegungen für diese Intervalle sehr schwierig. Bei der höchsten Wasserstoffkonzentration scheint es so, als ob mit zunehmender Heizrate das Reduktionsintervall kleiner wird. Dieser Effekt ist auf eine höhere Reaktionsgeschwindigkeit, bedingt durch die hohe Wasserstoffkonzentration, zurückzuführen, obwohl die kleinere Reduktionszeit eigentlich zu einer Verbreiterung von ΔT führen sollte. Bei dieser hohen Heizrate hat der Unterschied zwischen 5 % und 50 % H_2 einen merklichen Einfluss auf die Reduktionsintervallbreite. Bei 50 % H_2 sind die Reduktionsintervalle ΔT, unabhängig von der Heizrate, annähernd gleich bei etwa 50 K.
Ergänzend zeigt Abbildung 10c die oben angesprochene Abhängigkeit der Reduktion von der Zeit. Die Zeitspannen Δt der Reduktionsintervalle nehmen für die jeweiligen Wasserstoffkonzentrationen mit abnehmender Heizrate zu. Diese vermutlich exponentielle Abnahme untermauert die oben gemachten Aussagen.

Das Reduktionsverhalten der nanostrukturierten Eisenoxidteilchen ist, wie oben auszugsweise gezeigt, von der Menge an Wasserstoff und der Reduktionstemperatur abhängig. Ein Grund könnte sein, dass die Teilchen mit zunehmender Temperatur mobiler werden und sich so zu größeren Partikeln, natürlich immer noch beschränkt durch den Porendurchmesser, zusammenlagern können und somit ihr Reduktionsverhalten ändern. Das Oberflächen- zu Volumenverhältnis der Partikel nimmt mit zunehmender Partikelgröße ab und somit findet eine Verlagerung hin zu höheren Temperaturen und kürzeren Reduktionsintervallen statt. Dieser Effekt wurde auch am volumenkristallinen Hämatit nachgewiesen. Daneben hat auch die Wahrscheinlichkeit des Zusammentreffens von Eisenoxidteilchen mit den Wasserstoffteilchen einen Einfluss auf den Reduktionsverlauf. Die Wahrscheinlichkeit des

Aufeinandertreffens zweier Teilchen und damit die einer Reaktion nimmt mit steigender Wasserstoffkonzentrationen und Temperatur zu.

Das größte Problem bei den Versuchen, eine Erklärung für die beobachteten Verhaltensweisen während der Reduktion zu finden, liegt in der Komplexität des Systems selber. Die auftretenden Reduktionsreaktionen laufen als Konkurrenzreaktionen ab, bei denen der durch Reduktion freigesetzte Sauerstoff eine Rückreaktion (Oxidation) hervorruft. Diese Konkurrenzreaktionen stehen alle in einem thermischen Gleichgewicht miteinander, welches sich durch die steigende Reaktionstemperatur ständig neu einzustellen versucht. Untersuchungen zur ständigen Neueinstellung des thermischen Gleichgewichtes und dem Ablauf der Konkurrenzreaktionen, unmittelbar beeinflusst durch die Heizrate und die Wasserstoffkonzentration, könnten vermutlich die oben beobachteten und diskutierten Ergebnisse detaillierter erklären. Dazu wäre eine ausführliche kinetische Untersuchung der Reduktionen wünschenswert. Leider ist die Wissenschaft heutzutage noch nicht in der Lage, diese komplexen, nicht zeit- sondern temperaturabhängigen Reaktionen kinetisch zu interpretieren.

Neben den oben beschriebenen temperatur- und wasserstoffkonzentrationsabhängigen Reduktionen wurden auch Reduktionen bei konstanter Temperatur durchgeführt. Dazu wurde die Probe möglichst schnell auf die gewünschte Temperatur geheizt, bis zum Reduktionsende dort gehalten, dann schnell abgekühlt und hinterher charakterisiert.

Wie aus der Tabelle 3 zu entnehmen ist, wird bei der Reduktion unter bestimmten Bedingungen phasenreines Magnetit und Eisen als Reduktionsprodukt sowie ein hoher Anteil an Wüstit (max. 74 %) in den Porensystemen der Gastspezies erhalten.

Deutlich zu sehen ist, dass bei einer Temperatur von 573 K das Eisen(III)oxid im CMK-3 zu einer reinen Magnetitphase, das volumenkristalline Hämatit zu einem Gemisch aus Hämatit (40 %) und Magnetit (69%) reduziert wird. Dies ist eindeutig ein Effekt, der auf die Nanostrukturierung bzw. die dünnen Schichten der Eisen(III)oxide in den Porensystemen der Wirtspezies gegenüber dem volumenkristallinen Hämatit zurückzuführen ist.

Tabelle 3: Ergebnisse der LC-XANES Analyse für die Wirt/Gast-Verbindung (wgv) Fe_2O_3@CMK-3 sowie für das volumenkristalline Hämatit (vh) nach den jeweiligen Reduktionsprozessen bei konstanten Temperaturen mit 5 % H_2 in N_2.

Temperatur	Phase / Anteil	Fe_2O_3	Fe_3O_4	$Fe_{1-x}O$	Fe^0
573 K	wgv	-	99 %	-	-
	vh	40 %	60 %	-	-
623 K	wgv	4 %	76 %	20 %	-
	vh	-	99 %	-	-
723 K	wgv	-	10 %	74 %	16 %
	vh	-	28 %	64 %	7 %
873 K	wgv	-	-	-	100 %
	vh	-	-	-	99 %

"-" bedeutet, dass mit dieser Methode keine Phase detektiert wurde.

Die oben beschriebenen Reduktionsexperimente sind, wie schon in der Einleitung beschrieben, sehr zeit- und materialaufwendig. Für eine temperaturabhängige Reduktion wie der in Abbildung 8 gezeigten, wurden 35 Reduktionsansätze einschließlich späterer Charakterisierung durchgeführt. Für jeden der 35 Punkte musste die Reduktionsanlage wieder abgekühlt, neu bestückt und gestartet werden, ein insgesamt sehr zeitaufwendiges Unternehmen, gerade bei den niedrigen Heizraten. Daraus folgte die Überlegung, die Reduktion *in situ* zu verfolgen. Obwohl die *in situ* Röntgenabsorptionsspektroskopie gerade auf dem Gebiet der Katalyse schon lange angewendet wird, gab es keine geeignete Reaktionszelle für diese Art von Proben. Entweder konnte mit den existierenden Zellen nicht hoch genug geheizt werden, die Benutzung von Wasserstoff war nicht möglich oder sie hatte kein Fenster zur Detektion der Fluoreszenzstrahlung.

Letzteres war wegen der geringen Menge an Eisenteilchen unabdingbar. Aus dieser Not heraus wurde eine entsprechende Reduktionszelle (siehe Abbildung 11) entwickelt und erfolgreich getestet. Selbstverständlich ist der Einsatz dieser Zelle nicht auf die hier benötigten Parameter beschränkt.

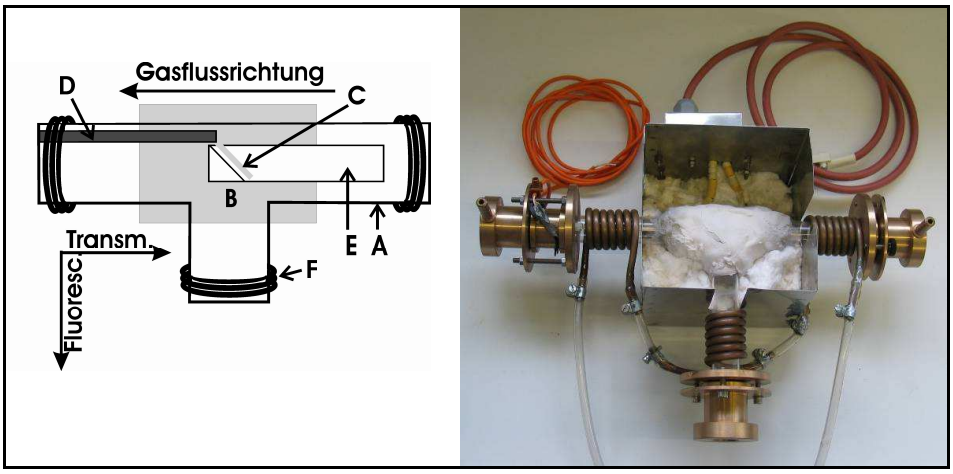

Abbildung 11: Links: Schematische Zeichnung der Zelle mit A: T-förmiges Quarzrohr, B: Heizbereich (grau schattiert), C: Probenposition, D: Temperaturfühler, E: Probenhalter, F: Wasserkühlung des Fluoreszenzarms. Rechts: Blick von oben auf die geöffnete Zelle und teilweise entfernter Isolierung.

Nach den ersten erfolgreichen Tests wurde die temperaturabhängige Reduktion des nanostrukturierten Eisen(III)oxides im Fe_2O_3@CMK-1 sowie die von volumenkristallinem Hämatit durchgeführt. Aus der Serie der erhaltenen Spektren (siehe Abbildung 12) wurden mittels einer Faktoranalyse nach Malinowaski[53] und Ressler[54] die Anteile der einzelnen Eisenoxidphasen bestimmt. Deutlich sind die Änderungen der weißen Linie und der EXAFS-Oszillationen während der Reduktion zu sehen. Auch hier ändert sich die Kantenlage um 8 eV bei der Umwandlung von Fe_2O_3@CMK-1 zu Fe@CMK-1.

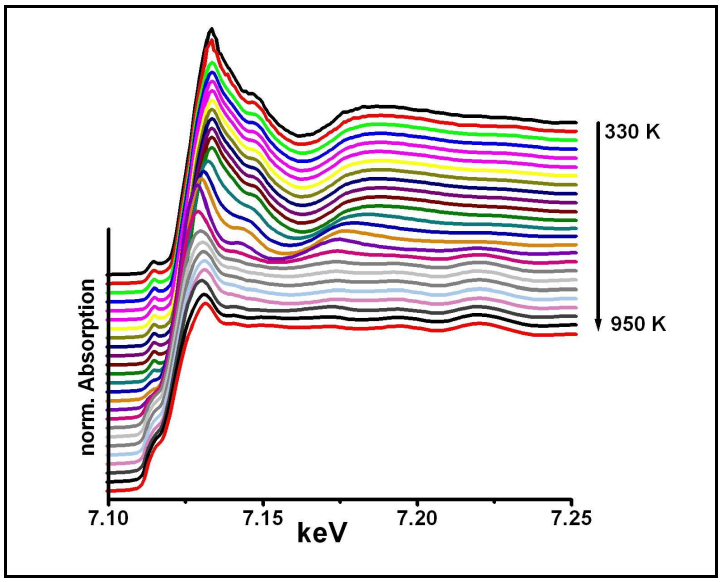

Abbildung 12: Temperaturabhängige in situ XAS-Messungen an der Fe K-Kante von Fe_2O_3@CMK-1 während der Reduktion mit 4 % H_2 in N_2.

Bei einem Vergleich der auftretenden Phasen (Abbildung 13) von der Einlagerungsverbindung und dem volumenkristallinen Hämatit ist deutlich zu sehen, dass das Reduktionsintervall der Einlagerungsverbindung schon bei niedrigeren Temperaturen beginnt und fast doppelt so breit ist. Der frühere Reduktionsbeginn ist vermutlich auf die geringe Teilchengröße (< 3 nm) und damit eine erhöhte thermochemische Aktivität der Eisen(III)-oxidteilchen im Fe_2O_3@CMK-1 zurückzuführen. Die Verbreiterung des Reduktionsintervalls kann wahrscheinlich mit einer durch die Poren erschwerten bzw. eingeschränkten Diffusion der Wasserstoffmoleküle erklärt werden.

Abschließend lässt sich zu diesen Untersuchungen sagen, dass die Reduktion von Fe_2O_3@CMK-1 nicht so schnell wie beim volumenkristallinen Hämatit bei gleichzeitig besserer Auflösung der einzelnen Phasen abläuft. Vergessen werden darf aber nicht, dass auch der Kohlenstoff der Wirtstruktur einen Einfluss auf das Reduktionsverhalten haben könnte.

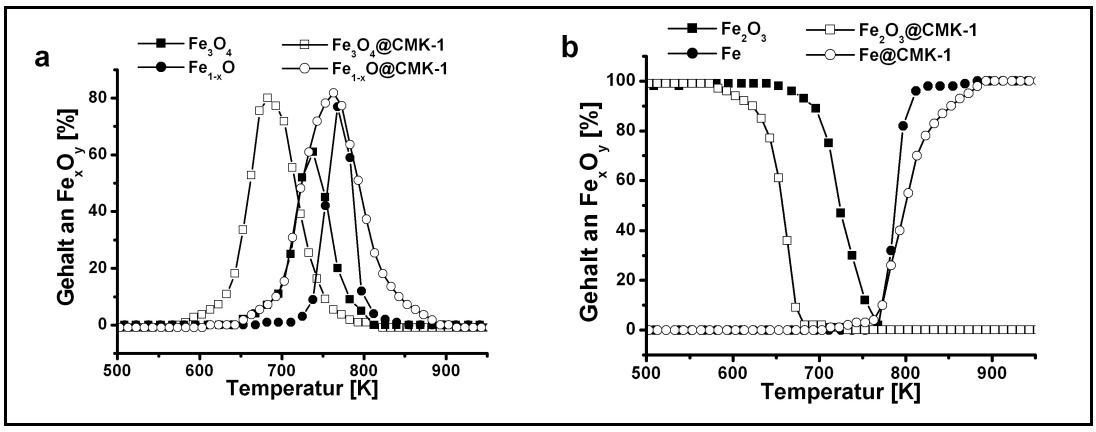

Abbildung 13: Vergleich zwischen den jeweiligen Eisenoxidphasen, die während der Reduktion von Fe_2O_3@CMK-1 und volumenkristallinem Hämatit auftreten.

Durch diese *in situ* Reduktion und Detektion ist es nun in Zukunft möglich, umfangreiche Redoxuntersuchungen zeit- und materialeffizient zu betreiben. Vernachlässigt werden darf dabei allerdings nicht der Zeitaufwand, welcher für eine vernünftige Auswertung der Spektren notwendig ist.

Parallel zu den hier beschriebenen Untersuchungen wurden Proben von Fe_xO_y@CMK-n ersten katalytischen Tests unterzogen. Da diese Tests nicht von mir, sondern von Mitarbeitern des Instituts für Organische Chemie und des Instituts für Katalyse der Bulgarischen Akademie der Wissenschaften in Sofia unter Leitung von Prof. Dr. Christo Minchev durchgeführt wurden, soll an dieser Stelle nur ein kurzer Abriss über die Ergebnisse erfolgen.

Untersucht wurde die katalytische Aktivität verschiedenen modifizierter Fe_xO_y@CMK-n auf die Methanolzersetzung zu Methan und Kohlenstoffdioxid als Hauptprodukte. Die Einlagerungsverbindungen wurden aus einer wässrigen (A) und einer ethanolischen (B) Eisennitratlösung unterschiedlicher Konzentration (5 und 0,5 M) hergestellt und dementsprechend als z.B. 0.5FeCMK-3A bezeichnet. Die temperaturabhängige Methanolzersetzung der verschiedenen katalytischen Spezies ist in Abbildung 14 dargestellt.

In Abhängigkeit von der Menge an nanostukturiertem Eisen(III)oxid ist ein signifikanter katalytischer Effekt für Temperaturen höher als 650 K für 0.5FeCMK-n bzw. 625 K für 5FeCMK-n sichtbar. Bei der Massenbilanzierung für die vollständige Methanolumsetzung sind keine Unterschiede zu erkennen.

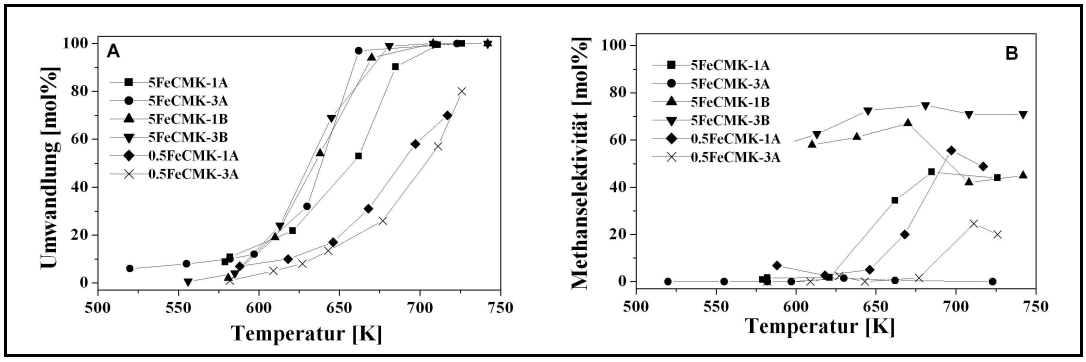

Abbildung 14: Methanolumsetzung (A) und Methanselektivität (B) in Abhängigkeit der Temperatur für verschieden modifizierte Einlagerungsverbindungen der Art Fe_2O_3@CMK-n.

Im Gegensatz dazu hat die Porenstruktur und die bei der Imprägnierung eingesetzte Lösung einen signifikanten, temperaturunabhängigen Einfluss auf die Produktverteilung. Insgesamt gesehen ist eine höhere katalytische Aktivität in Bezug auf die Methanbildung bei den aus den ethanolischen Lösungen synthetisierten Proben sichtbar. Gleichzeitig weisen die Proben der Serie CMK-1A eine höhere Methanselektivität als die der Serie CMK-3A auf. Diese Effekte wurden auch durch katalytische Experimente unter isothermischen Bedingungen bestätigt.

4 Zusammenfassung

Zum ersten Mal wurden nanostrukturierte Metalloxide der 3d-Übergangsmetalle in den Porensystemen von geordneten mesoporösen Kohlenstoffen synthetisiert. Über ein nasschemisches Imprägnierungsverfahren wurden so Wirt/Gast-Verbindungen vom Typ Me_xO_y@CMK-n mit n = 1 und Me = Fe, Cu, Co sowie mit n = 3 und Me = Mn, Fe, Co, Ni, Cu und Zn erhalten. Die *in situ* Synthese führt zur Bildung von fein verteilten, nanostrukturierten Metalloxidteilchen, die in ihrer Größe durch den Porendurchmesser der mesoporösen Kohlenstoffe beschränkt sind. Durch eine Reduktion innerhalb der Poren wurden aus den Metalloxiden von Eisen, Kobalt, Nickel und Kupfer die entsprechenden nanostrukturierten Metalle erhalten. Mangan(IV)oxid wurde zu Mangan(II)oxid reduziert und für Zinkoxid wurde eine Verbesserung der Struktur in Bezug auf die Einkristalldaten beobachtet.

Die Wirt/Gastverbindungen wurden mit dem sich ergänzenden, leistungsstarken Kanon an Untersuchungsmethoden wie der P-XRD, N_2-Physisorption, TEM, IR-Spektroskopie, Raman-Spektroskopie und XAS charakterisiert. Damit wurde (a) die Erhaltung der Wirtstruktur während der Imprägnierungsprozesse und der Reduktionen und (b) die Einlagerung der Gaststrukturen überwiegend in den Porenkanälen und nicht auf der Oberfläche der Wirtstruktur nachgewiesen. Mit Hilfe der Röntgenabsorptionsspektroskopie wurde ein umfangreiches Bild über die strukturelle Nahordnung der Gastverbindungen gewonnen: Durch die Auswertungen der XANES wurden die Strukturen, durch die Auswertung der EXAFS die Strukturparameter erhalten. Zusätzlich untermauerte die EXAFS-Analyse die Bildung von kleinen, leicht ungeordneten Nanopartikeln in der Größenordnung < 3 nm. Somit wurde die Bildung von leicht ungeordneten Metallen und Metalloxiden in den Porenkanälen der mesoporösen Kohlenstoffe CMK-1 und CMK-3 nachgewiesen.

Für die Auswerteprozedur wurde, bedingt durch die Nanostrukturierung der Wirt/Gast-Verbindungen, die herkömmliche Auswerteprozedur verfeinert und die damit erzielten Ergebnisse der der Standardprozedur gegenübergestellt. Somit wurde Zugang zu einem Auswerteverfahren geschaffen, mit dem auch Spektren von Teilchen kleiner 3 nm umfassender ausgewertet werden können. So war es zum Beispiel erstmalig möglich, für das Eisen(III)oxid im Fe_2O_3@CMK-n Aussagen über die ersten vier Fe-Fe-Schalen zu machen sowie das Fehlen von seitenverknüpften Oktaedern nachzuweisen.

Erstmalig wurde das Reduktionsverhalten von nanostrukturierten Eisen(III)oxiden strukturiert und umfassend untersucht. Die Reduktionen der Proben Fe_2O_3@CMK-n wie auch des volumenkristallinen Hämatits als Referenzsubstanz wurden dabei sowohl temperatur- als auch zeitabhängig durchgeführt. Die temperaturabhängigen Reduktionen zeigen die Abhängigkeiten der Bildung der einzelnen auftretenden Phasen u.a. von der Heizrate, der Menge an Reduktionsgas und der Menge an Eisen(III)oxid. Im Vergleich zum volumenkristallinen Hämatit beginnt die Reduktion bei den Wirt/Gast-Verbindungen schon bei geringeren Temperaturen, die einzelnen Phasen sind besser aufgelöst und das Reduktionsintervall ist verbreitert. Die bei dem komplexen Reduktionssystem Hämatit – Magnetit – Wüstit – Eisen stattfindenden Konkurrenzreaktionen erlauben nach dem heutigen Stand der Wissenschaft leider noch keine umfangreiche Interpretation des beschriebenen Reduktionsverhaltens. Es ist jedoch zu sehen, dass die Reduktionsschritte hauptsächlich durch den Anteil an Wasserstoff sowie der Reduktionstemperatur beeinflusst werden.
Mittels der zeitabhängigen Reduktionen wurde phasenreines Magnetit und Eisen sowie ein hoher Anteil an Wüstit in den Porensystemen der Wirtstruktur erzielt. Somit wurde eine erste umfangreiche Studie bezüglich des Reduktionsverhaltens der nanostrukturierten Eisenoxide in den Porensystemen der mesoporösen Kohlenstoffe CMK-1 und CMK-3 vorgestellt.

Die Reduktion der Gastsysteme mit anschließender Charakterisierung ist sehr zeit- und materialaufwendig. Eine elegante, schnelle Methode ist die Verfolgung der Reduktion *in situ* mittels *in situ* XAS. Speziell dafür wurde eine entsprechende Reaktionszelle entwickelt und implementiert.

Parallel zu den hier beschriebenen Untersuchungen wurden Wirt/Gast-Verbindungen vom Typ Fe_xO_y@CMK-n ersten katalytischen Tests unterzogen. Diese wurden in Kooperationen mit dem Institut für Organische Chemie und dem Institut für Katalyse der Bulgarischen Akademie der Wissenschaften in Sofia unter Leitung von Prof. Dr. Christo Minchev durchgeführt.

5 Literatur

[1] Ryoo, R.; Joo, S.H.; Jun, S. J. *Phys. Chem. B* **1999**, *103*, 37, 7743-7746.

[2] Lee, J.; Kim, J.; Hyeon, T. *Adv. Mater.* **2006**, *18*, 2073 und Literaturstellen darin.

[3] Ryoo, R.; Joo, S.H.; Jun, S.; Tsubakiyama, T.; Terasaki O. in: A. Galaraneau, F. di Renzo, F. Fajula, J. Vedrine (Eds.), Zeolithes and Mesoporous Materials at the Dawn of the 21st Century, *Studies in Surface Science and Catalysis, Vol. 135*, Elsevier, Amsterdam **2001** 1121

[4] Darmstadt, H.; Roy, C.; Kaliaguine, S.; Choi, S.J.; Ryoo, R. *Carbon* **2002**, *40*, 14, 2673-2683.

[5] Kruk, M.; Jaroniec, M.; Ryoo, R.; Joo, S.H. *J Phys Chem B* **2000**, *104(33)*, 7960.

[6] Jun, S.; Joo, S.H.; Ryoo, R.; Kruk, M.; Jaroniec, M.; Liu, Z.; Ohsuna, T.; Terasaki, O. *J. Am Chem Soc* **2000**, *122*, 43, 10712-10713.

[7] Ryoo, R.; Joo, S.H.; Kruk, M.; Jaroniec, M. *Adv Mater* **2001**, *13*, 9, 677-681 und Literaturstellen darin.

[8] Lee, J.; Yoon, S.; Hyeon, T.; Oh, S.M.; Kim, K.B. *Chem Commun* **1999**, 2177-2178.

[9] Joo, S.H.; Choi, S.J.; Kwak, J.; Liu, Z.; Terasaki, O.; Ryoo, R. *Nature* **2001**, *412*, 6843, 169-1728.

[10] Darmstadt, H. ; Roy, C. ; Kaliaguine, S. ; Joo, S.H. ; Ryoo, R. *Microporous Mesoporous Mater* **2003**, *60*, 1-3, 139-149.

[11] Ryoo, R. ; Joo, S.H. *Stud Surf Sci Catal* **2004**, *148*, 241-260.

[12] Mariwala, R.K. ; Acharya, M.; Foley, H.C. *J Microporous Mater* **1998**, *22(2)*, 281.

[13] Schüth, F. *Angewandte Chemie Int. Ed.* **2003**, *42*, 3604-3622.

[14] Weitkamp, J.; Hunger, M.; Rymsa, U. *Microporous Mesoporous Mater.* **2001**, *48(1-3)*, 255-270.

[15] Weitkamp, J.; Glaeser, R. Catalysis in Winnacker-Kuechler: *Chemische Technik* (5. Auflage) **2004**, 1, 645-718. Publisher: Wiley-VCH Verlag GmbH & Co. KGaA, Weinheim, Germany CODEN: 69GEIJ, general review written in german.

[16] Bajt, S.; Sutton, S.R.; Delaney, J.S. *Cosmochimica Acta* **1994**, *58*, 5209-5214.

[17] Becker, K.D.; Niemeier, D.; Wissmann, S.; Oversluizen, M.; Couves, J.W.; Chadwick, A.V. *Nucl. Instr. Meth.* **1995**, *B97*, 111-114.

[18] Cornell, R.M.; Schwertmann, U. *The Iron Oxides*, Wiley-VCH, Weinheim. **2003**.

[19] Darken, L.S.; Gurry, R.W. *J. Am. Chem. Soc.* **1946**, *68*, 798-819.

[20] de Masi, R.; Reinicke, D.; Muller, F.; Steiner, P.; Hufner, *S. Surf. Sci.* **2002**, *516*, L515-L521.

[21] Dünwald, H.; Wagner, C. *Z. Anorg. Allg. Chem.* **1931**, *199*, 321-819.

[22] Fjellvang, H.; Hauback, B.C.; Vogt, T.; Stolen, S. *Am. Mineral.* **2003**, *87*, 347-349.

[23] Fröba, M.; Köhn, R.; Bouffaud, G.; Richard, O.; van Tendeloo, G. *Chem. Mater.* **1999**, *11*, 2858-2865.

[24] Köhn, R.; Fröba, M. *Z. Anorg. Allg. Chem.* **2003**, *629*, 1673-1682.

[25] Köhn, R.; Paneva, D.; Dimitrov, M.; Tsoncheva, T.; Mitov, I.; Minchev, C.; Fröba, M. *Micropor. Mesopor. Mater.* **2003**, *63*, 125-137.

[26] Rao, Y.K.; Moinpour, M. *Metal Trans. B: Process Metallurgy* **1983**, *14B*; 711-723.

[27] Minchev, C.; Huwe, H.; Tsoncheva, T.; Paneva, D.; Dimitrov, M.; Mitov, I.; Fröba, *Micropor. Micropor. Mesopor. Mater.* **2005**, *8*, 333-341.

[28] Tsoncheva, T.; Paneva, D.; Mitov, I.; Huwe, H.; Fröba, M.; Dimitrov, M.; Minchev, C. *React. Kinet. Catal. Lett.* **2004**, *83*, 299-305.

[29] Basinska, A.; Jozwiak W.K.; Goralski J.; Domka F. *Appl. Catal., A: General* **2000**, *190*(1,2), 107-115.

[30] Chen, L.; Lu, G.L. *J. Mater. Sci.* **1999**, *34*, 17, 4193-4197.

[31] Takenaka, S.; Son, V.T.D.; Otsuka, K. *Energy & Fuels* **2004**, *18*, 3, 820-829.

[32] Waychumas, G.A.; Kim, C.S.; Banfield, J.F. *J. Nanoparticles Res.* **2005**, *7*, 409-433.

[33] Jolivet, J.P.; Chameac, C.; Tronc, E. *Chem. Comm.* **2004**, 481-488.

[34] Blake, R.L.; Hessevick, R.E.; Zoltai, T.; Finger, L.W. *Am Mineral* **1966**, *51*, 123-129.

[35] Pauling, L.; Hendricks, S.B. *J. Am. Chem. Soc.* **1925,** *47*, 781-790.

[36] Selvam, P.; Dapurkar, S.E.; Badamali, S.K.; Murugasam, M.; Kuwano, H. *Ad. Func. Mater.* **2002**, *12(2)*, 143-148.

[37] Redl, F.X.; Black, C.T.; Papaefthymiou, G.C.; Sandstrom, R.L.; Yin, M.; Zeng, H.; Murray, C.B.; O`Brien, S.P. *J. Am. Chem. Soc.* **2004**, *126*, 44, 14583-14599.

[38] Weng, Y.C.; Rusakova, I.A.; Baikalov, A.; Chen, J.W.; Wu, N.L. *J. Mater. Res.* **2005**, *20*, 1, 75-80.

[39] Bradshow, A.V. *Trans Inst Min Metall* **1970**, *79C*, 281-294.

[40] St. John, D.H.; Mathews, S.P.; Hayes, P.C. *Met Trans.* **1984**, *15B*, 701-708.

[41] Rau, M.; Rieck, D.; Evans, J.W. *Met Trans.* **1987**, *18B*, 257-278.

[42] Hayes, P.C.; Grieveson, P. *Trans Chim B* **1981**, *12B*, 319-326.

[43] El-Tabirou, M.; Dupre, B.; Gleitzer, C. *Met Trans.* **1988**, *19B*, 311-317.

[44] Brieler, F.J.; Grundmann, P.; Fröba, M.; Chen, L.; Klar, P.J.; Heimbrodt, W.; Krug von Nidda, H.-A.; Kurz, T.; Loidl, A. *J. Am. Chem. Soc.* **2004**, *126*, 797-807.

[45] Brieler, F.J.; Grundmann, P.; Fröba, M.; Chen, L.; Klar, P.J.; Heimbrodt, W.; Krug von Nidda, H.-A.; Kurz, Th.; Loidl, A. *Chem. Mater.* **2005**, *17*, 4, 795-803.

[46] Köhn, R.; Fröba, M. *Catalysis Today* **2001**, *68*, 227-236.

[47] Morey, M.S.; Stucky, G.D., Schwarz, S.; Fröba, M. *J Phys Chem B* **1999**, 103, 2037-2041.

[48] Sing, K.S.W.; Everett, D.H.; Haul, R.A.W.; Mouscou, L.; Pierotti, R.A.; Rouquerol, J.; Siemieniewska, T. *Pure Appl. Chem.* **1985**, *57*, 603-619.

[49] Greegor, R.B.; Lytle, F.W. *J Catal* **1980**, *63*, 476-486.

[50] Lee, P.A.; Pendry, J.B. *Phys Rev B* **1975**, *11*, 2795-2811.

[51] Manceau, A.; Drits, V.A. *Clay Mineral* **1993**, *28*, 165-184.

[52] Grunes, L.A. *Phys Rev B* **1983**, *27/4*, 2111-2131.

[53] Malinowaski, E.R.; Howery, D.G. *Factor Analysis in Chemistry* **1980**, New York:Wiley.

[54] Ressler, T.; Wong, J.; Roos, J.; Smith, I.L. *Environ. Sci. Technol.* **2000**, *34*, 950.

6. Liste weiterer Veröffentlichungen

6.1 Konferenzbegleitende Veröffentlichungen

- Pore design in view of adsorption, reductive and catalytic properties of Fe or Cu oxide modified large mesoporous silicas
  T. Tsoncheva, J. Rosenholm, H. Huwe, D. Paneva, M. Dimitrov, I. Mitov, F. Kleitz, M. Linden, M. Fröba and C. Minchev
  Stud. Surf. Sci. Catal., **2005**, *158*, 773-780.

- Effect of Support Pore Size on the Structural and Catalytic Properties of Iron and Cobalt Oxides modified SBA-1, SBA-15, MCM-41 and MCM-48 Silica Materials
  C. Minchev, H. Huwe, T. Tsoncheva, M. Dimitrov, D. Paneva, I. Mitov, M. Fröba
  Proc. 14th Internat. Zeolite Conf., **2004**, p. 841,
  ISBN: 0-958-46636-X

- Synthesis and Characterization of CuO and Fe_2O_3 nanoparticles within mesoporous MCM 41/-48 silica
  C. Minchev, R. Köhn, T. Tsoncheva, M. Dimitrov, I. Mitov, D. Paneva, H. Huwe and M. Fröba,
  Stud. Surf. Sci. Catal. **2002**, 142, 1245.

6.2 Berichte

- Synthesis and characterization of Mn(II) and Mn(IV) oxide nanoparticles inside mesoporous carbon CMK-3
  H. Huwe and M. Fröba
  HASYLAB-Jahresbericht 2005 (Teil 1), HASYLAB/DESY, Hamburg **2005**, S. 527-528.

- A New *In Situ* Cell for XAFS Investigations
  H. Huwe and M. Fröba
  HASYLAB-Jahresbericht 2004 (Teil 1), HASYLAB/DESY, Hamburg **2004**, S. 1115-1116.

- Influence of the synthesis conditions on the anatase-rutile phase transition of TiO_2
  S. Eiden-Assmann, J. Widoniak, H. Huwe and M. Fröba
  HASYLAB-Jahresbericht 2004 (Teil 1), HASYLAB/DESY, Hamburg **2004**, S. 329-330.

- Synthesis and characterization of iron(III) oxide within mesoporous carbon CMK-3
  H. Huwe and M. Fröba
  HASYLAB-Jahresbericht 2004 (Teil 1), HASYLAB/DESY, Hamburg **2004**, S. 479-480.

- XAFS investigations of nanostructured GaAs inside the pore system of mesoporous MCM-41 matrices
  S. Kroker, H. Huwe and M. Fröba
  HASYLAB-Jahresbericht 2003 (Teil 1), HASYLAB/DESY, Hamburg **2004**, S. 541-542.

- XAFS investigations on the reduction products of iron(III) oxide nanoparticles within mesoporous carbon
  H. Huwe and M. Fröba
  HASYLAB-Jahresbericht 2003 (Teil 1), HASYLAB/DESY, Hamburg **2004**, S. 289-290.

- XAFS investigations of iron(III) oxides inside the pore system of mesoporous carbon
  H. Huwe and M. Fröba
  HASYLAB-Jahresbericht 2002 (Teil 1), HASYLAB/DESY, Hamburg **2003**, S. 457-458.

- Using EXAFS for the structural chracterization of iron oxides inside the pore system of mesoporous silica and carbon
  H. Huwe and M. Fröba
  HASYLAB-Jahresbericht 2001 (Teil 1), HASYLAB/DESY,Hamburg **2002**, S. 807-808.

7 Danksagung

Als erstes möchte ich mich bei Prof. Dr. Michael Fröba unter anderem für die freundliche Aufnahme in seine Arbeitsgruppe, die Überlassung der interessanten Aufgabenstellung, der Möglichkeit zur freien Forschung und den hervorragenden Arbeitsbedingungen bedanken.

Frau Marie-Luise Wolff danke ich für die praktische Unterstützung meiner Arbeit im Labor, ihr Engagement sowie die sehr gute und produktive Zusammenarbeit. Für ihren im November 2006 angetretenen, wohlverdienten Ruhestand wünsche ich ihr alles Gute.

Bei Prof. Dr. Christo Minchev vom Institut für Organische Chemie der Bulgarischen Akademie der Wissenschaften in Sofia, Bulgarien, möchte ich mich für die sehr ertragreiche Kooperation und, was für mich viel mehr zählt, für die daraus entstandene Freundschaft bedanken.

Weiterhin möchte ich mich bei denen Bedanken, die mir während der Anfertigung dieser Arbeit mit Rat und Tat zur Seite gestanden oder/und mit mir kooperiert haben. Das sind in alphabetischer Reihenfolge:

Brieler, Dr. Felix, ehemaliger Mitarbeiter AG Prof. Dr. Fröba
Brüggman, Ulf, HASYLAB@DESY, Hamburg
Funari, Dr. Sergio, HASYLAB@DESY, Hamburg
Gath, Carina, AG Prof. Dr. Fröba
Grundmann, Petra, AG Prof. Dr. Fröba
Güngerich, Martin, Philips-Universität Marburg
Herrendorf, Dr. Wolfgang, AG Prof. Dr. Fröba
Hoffmann, Dr. Frank, AG Prof. Dr. Fröba
Jäger, Dana, AG Prof. Dr. Fröba
Jakubowski, Michaela, AG Prof. Dr. Fröba
Klar, Prof. Dr. Peter, Philips-Universität Marburg, JLU Gießen
Klementiev, Dr. Konstantin, HASYLAB@DESY, Hamburg
Koch, Günter, AG Prof. Dr. Fröba
Köhn, Dr. Ralf, ehemaliger Mitarbeiter AG Prof. Dr. Fröba
Kroker, Sven, AG Prof. Dr. Fröba
Morell, Jürgen, AG Prof. Dr. Fröba
Rebbin, Dr. Vivian, AG Prof. Dr. Fröba
Ressler, Dr. Thorsten, Fritz-Haber-Institut, Berlin
Roggenbuck, Jan, AG Prof. Dr. Fröba
Sack, Ralf und Mitarbeiter, Werkstatt der Anorg. und Analyt. Chemie der JLU Gießen
Serafin, Dr. Michael, AG Prof. Dr. Fröba
Stumpf, Tamara, AG Prof. Dr. Fröba
Thommes, Dr. Matthias, Firma Quantachrome Instruments, Florida, USA
Tsoncheva, Dr. Tanja, BAS, Sofia, Bulgarien
Welter, Dr. Edmund, HASYLAB@DESY, Hamburg
Wienold, Dr. Julia, HASYLAB@DESY, Hamburg
Wörner, Hubert, AG Prof. Dr. Fröba
Wolf, Jürgen, Inst. f. Anorg. und Analyt. Chemie der JLU Gießen

Ferner möchte ich mich bei der JLU Gießen, dem Fonds der Chemischen Industrie und der DFG für die finanzielle Unterstützung bedanken. Dem HASYLAB@DESY danke ich für die Finanzierung und Bereitstellung der Messzeiten.